LBL-22419

**Lawrence Berkeley Laboratory**
UNIVERSITY OF CALIFORNIA

Materials & Molecular
Research Division

# NEAR THRESHOLD STUDIES OF PHOTOELECTRON SATELLITES

P.A. Heimann
(Ph.D. Thesis)

November 1986

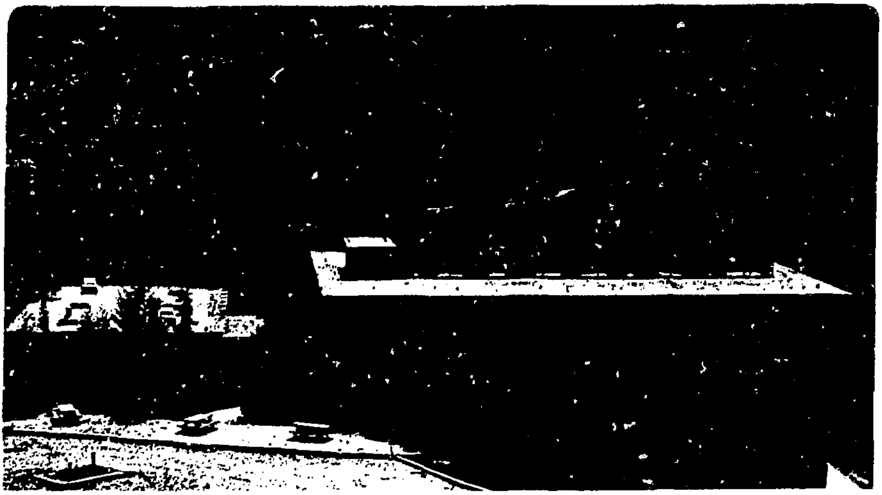

Prepared for the U.S. Department of Energy under Contract DE-AC03-76SF00098

LBL--22419

DE87 004594

# Near Threshold Studies of Photoelectron Satellites

Philip Alfred Heimann

Ph.D. Thesis

*Lawrence Berkeley Laboratory*
University of California
Berkeley, California 94720

November 1986

This work was supported by the Director, Office of Energy Research, Office of Basic Energy Sciences, Chemical Sciences Division of The U.S. Department of Energy under Contract Number DE-AC03-76SF00098.

# Table of Contents

# NEAR THRESHOLD STUDIES OF PHOTOELECTRON SATELLITES

Philip Alfred Heimann

Materials and Molecular Research Division
Lawrence Berkeley Laboratory
and
Department of Chemistry
University of California
Berkeley, California 94720

## Abstract

Photoelectron spectroscopy and synchrotron radiation have been used to study correlation effects in the rare gases: He, Ne, Ar, Kr, and Xe. Two kinds of time-of-flight electron analyzers were employed to examine photoionization very close to threshold and at higher kinetic energies. Partial cross sections and angular distributions have been measured for a number of photoelectron satellites. The shake-off probability has been determined at some inner-shell resonances.

The valence satellites of neon were studied from about 5 to 45 eV kinetic energy. The partial cross sections and angular distribution asymmetry parameters of the satellites are compared with those of the 2s and 2p main lines. The partial cross section and asymmetry parameter results are used to confirm the previous assignments of the satellite final states in neon and to consider, in general, the energy-dependent behavior of satellites.

The valence satellites of helium and neon were examined with threshold electron analysis. This measurement was the first direct observation of photoelectron satellites at threshold. Strong correlation effects were observed in the asymmetry parameters of the helium satellites and in the presence of many final states in the Ne threshold photoelectron spectrum.

Multiple-electron ejection was investigated at the inner-shell resonances: Ar 2p → ns, nd, Kr 3d → np, and Xe 4d → np. Multiple-electron ejection was observed to be a strong decay channel. At the resonances studied, a valence electron and the Rydberg electron are usually ejected in these transitions.

Threshold electron analysis was applied to the argon valence satellites. For argon at threshold, essentially all of the possible satellite final states, $^{2S+1}L$, were observed.

# I. INTRODUCTION

Photoelectron spectroscopy is an effective probe of electronic structure.[1] The experiments described in this thesis use photoelectron spectroscopy to examine electron correlation in atoms. Photoelectron spectra taken at a soft x-ray photon energy $h\nu$ contain discrete peaks at kinetic energies $\varepsilon_j$,

$$\varepsilon_j = h\nu - I_j, \tag{1}$$

where $I_j$ is the electron binding energy. In the independent-electron approximation, also known as Koopmans' theorem,[2] an electron is ionized from a given orbital while the other electrons remain in their initial state orbitals. In this limit, which can explain the intense main lines, the binding energy is associated with the orbital energy in the neutral atom.

The intensities of photoelectrons are proportional to the cross section $\sigma_j(\varepsilon_j)$, which in the dipole approximation is given by,[3]

$$\sigma_j(\varepsilon_j) = \frac{4\pi^2\alpha a_0^2}{3} (\varepsilon_j + I_j) \sum_k |\langle\psi_j^{(N-1)} \phi_k(\varepsilon_j)| \sum_\mu^N r_\mu \, |\psi_i^{(N)}\rangle|^2. \tag{2}$$

Here, $\alpha$ is the fine structure constant, $a_0$ is Bohr's radius, $\psi_j^{(N-1)}$ is the ion wavefunction, $\phi_k(\varepsilon_j)$ is the wavefunction of the continuum electron, and $\psi_i^{(N)}$ is the neutral atom wavefunction. The cross section depends on the dipole matrix elements, which in the independent-electron approximation simplify to integrals over the initial and final state orbitals, $\phi_j$ and $\phi_k(\varepsilon_j)$.

The angular distribution of photoelectrons in the dipole approximation and with linearly polarized light is described by Yang's theorem,[4]

$$\frac{d\sigma}{d\Omega} = \frac{\sigma}{4\pi}[1 + \beta P_2(\cos\theta)]. \qquad (3)$$

Here, $\beta$ is the angular-distribution asymmetry parameter, $P_2$ is the second Legendre polynomial, and $\theta$ is the angle between the light polarization vector and the photoelectron emission direction. The asymmetry parameter, which assumes values between -1 and 2, is sensitive to the phase of the outgoing photoelectron waves.

Photoelectron spectra have weak satellite peaks, which correspond to excited final states of the ion. These satellites cannot be explained within the independent-electron approximation. Electron correlation must be considered, and indeed the satellites yield insight into electron correlation.

The mechanisms used in discussing satellites are related to the methods for calculating satellite intensities. "Shake-up" refers to a calculation which uses single Slater determinants to describe the initial and final states.[5] In terms of a physical effect, shake-up involves the relaxation of the passive orbitals as the hole is formed. The satellite intensity depends on a product of overlap integrals between the passive orbitals in the initial atom and final ion. Shake-up should be most important for inner-shell ionization, in which the effective nuclear charge for the valence electrons changes by nearly one unit.

At a higher level of sophistication, a configuration interaction expansion is used to describe either or both the initial state (ISCI) or the final ionic state (FISCI).[6] Configuration interaction may include correlation in the initial atom and final ion as well as relaxation. In the case of FISCI, a satellite gains intensity from the admixture of the primary hole configuration in the satellite final state. For final states of different symmetry than the main line, ISCI can contribute, but FISCI cannot.

Both the shake-up and configuration interaction models, as described above, are only truly appropriate to the limit of high photoelectron kinetic energy. Shake-up, for example, invokes the sudden approximation, which requires photoabsorption and ejection of an electron to occur quickly. In the sudden limit, the (satellite) / (main line) intensity ratio is constant, independent of the energy. At the present time, the minimum kinetic energy for the sudden limit has not been determined.

The energy dependence of satellite cross sections has been introduced into the theoretical models in only a preliminary way. For shake-up, the varying length of time to create the hole has been considered.[7] For all satellite transitions, the resulting intensity is lower at threshold and increases to a constant value at higher kinetic energy. The changing dipole matrix elements can also influence satellite intensities even expressed as a ratio with the main line, since the satellite and main line will be at different kinetic energies.[8] Outside the sudden limit, additional mechanisms, sometimes referred to as continuum-state configuration interaction (CSCI), contribute to satellites. At some resonances for doubly-excited states, satellite cross sections are known to vary rapidly with photon energy.[9,10] At the satellite thresholds, being furthest from the sudden limit, CSCI effects should have their greatest influence.

Chapter III describes the cross sections and asymmetry parameters of the Ne valence satellites at low kinetic energies. For neon in this energy range, the most important satellite final states, $2p^4np\ ^2P^o$, can be reached by shake-up associated with 2p ionization. Predictions for satellite asymmetry parameters are not available except when symmetry requires the asymmetry parameter of the satellite and main line to be the same.

Chapters IV and VI present the first direct measurements of photoelectron satellites at threshold. The He, Ne, and Ar valence satellites were studied. Helium, a two-electron atom, is a special system for which much more detailed calculations have been performed.[11] In argon, a strong configuration interaction mixes the final ionic states $3s3p^6\ ^2S$ and $3s^23p^4nd\ ^2S$.[6,8] In general for the rare gases other than helium, FISCI is considered to be more important than ISCI because of the closed shell initial state.[6]

Another feature in photoelectron spectra which results from correlation is the continuous distribution of shake-off electrons. In shake-off, two ejected electrons share a total kinetic energy, usually with one electron being much faster than the other.[12] Chapter V is concerned with the shake-off occuring in the decay of inner-shell resonances of Ar, Kr, and Xe.

The following chapter describes the threshold electron analyzer and various other experimental methods.

REFERENCES

1. K. Siegbahn, C. Nordling, G. Johansson, J. Hedman, P.F. Heden, K. Hamrin, U. Gelius, T. Bergmark, L.O. Werme, R. Manne, and Y. Baer, ESCA Applied to Free Molecules (North-Holland, Amsterdam, 1969).
2. T. Koopmans, Physica 1, 104 (1933).
3. S.T. Manson, in Advances in Electronics and Electron Physics 41, 73 (1976).
4. C.N. Yang, Phys. Rev. 74, 764 (1948).
5. T. Aberg, Phys. Rev. 156, 35 (1967).
6. K.G. Dyall and F.P. Larkins, J. Phys. B 15, 203 (1982); K.G. Dyall and F.P. Larkins, J. Phys. B 15, 219 (1982).
7. T.D. Thomas, Phys. Rev. Lett. 52, 417 (1984); T.D. Thomas, J. Electron Spectrosc. Relat. Phenom. 40, 259 (1986).
8. H. Smid and J.E. Hansen, Phys. Rev. Lett. 52, 2138 (1984).
9. P.R. Woodruff and J.A.R. Samson, Phys. Rev. Lett. 45, 110 (1980).
10. D.W. Lindle, T.A. Ferrett, U. Becker, P.H. Kobrin, C.M. Truesdale, H.G. Kerkhoff, and D.A. Shirley, Phys. Rev. A 31, 714 (1985).
11. C. Greene, Phys. Rev. Lett. 44, 869 (1980).
12. T.N. Chang and R.T. Poe, Phys. Rev. A 12, 1432 (1975).

## II. EXPERIMENTAL

In this thesis gas phase photoemission experiments using synchrotron radiation are described. The experiments took place during ten runs at the Stanford Synchrotron Radiation Laboratory (SSRL) and one run at the Hamburg Synchrotronstrahlungslabor (HASYLAB). The radiation provided by these storage rings is an intense continuum from a few eV to a few tens of keV.[1] For our work, other important characteristics of synchrotron radiation are its high polarization and its time structure shown in Fig. 1. For a single bunch in the storage ring at SSRL, short pulses are emitted at a frequency of 1.28 MHz.

Two monochromators were used: the "new grasshopper" on beam line III-1 at SSRL[2,3] and the toroidal grating monochromator (TGM) at HASYLAB.[4] The "grasshopper" is a 1m radius Rowland circle monochromator with adjustable slit openings and two interchangeable gratings, with ruling densities of 600 l/mm and 1200 l/mm. The relative photon flux from the monochromator after passing through a 1500 Å thick Si window is shown by the solid line in Fig. 2. Pate[3] reported an absolute intensity of ~ $3 \times 10^9$ 1/s at 150 eV photon energy and with 15mA current in the storage ring. The energy resolution $\Delta(h\nu)$, at constant $\Delta\lambda$, increases with photon energy as $(h\nu)^2$. The dashed line in Fig. 2 represents the photon intensity at a constant energy resolution, which is more relevant to our experiments. The Si window is observed to absorb strongly at 100 eV, at the 2p subshell threshold.

The HASYLAB TGM provides higher intensity, in part because it accepts a larger horizontal angle from the storage ring: 9 mrad as compared with 2 mrad for the "grasshopper." Similar to the "grasshopper" the slits are adjustable and two effective gratings are provided, with 750 l/mm and 1500 l/mm ruling densities. The resolution of the TGM is somewhat better than the "grasshopper" at open slit settings, but improves only slowly as the slits are closed because of the imperfect focus at the exit slit. The polarization of the TGM must be carefully calibrated.

The time-of-flight apparatus has been described in detail elsewhere.[6] The same vacuum chamber, pumps, and most of the electronics were used for both the Double-Angle Time-of-Flight (DATOF) and threshold measurements. A thin Si window (Luxel) isolates the $10^{-10}$ torr vacuum of the monochromator from the $10^{-4}$ torr chamber vacuum. The main chamber is pumped by a 500 l/s Airco turbo pump and a 1000 l/s cryopump from CTI-cryogenics. A second 500 l/s Airco turbo pump provides differential pumping for the analyzers. For the DATOF experiments, the gas inlet uses a microchannel array. The gas source is nearly effusive. The pressure behind the gas inlet is held constant by a Granville-Phillips leak value and a capacitance manometer (MKS Instruments, Inc.). The photon intensity is monitored by a sodium salicylate scintillator and photmultiplier tube.

In the DATOF experiment, two electron analyzers are positioned at angles 0° and 55° with respect to the photon polarization direction. The photoelectron kinetic energy is inferred from the time delay between the synchrotron light pulse and the arrival of the electron at one of the two detectors. A field-free flight distance of 10.5 cm is followed by a pair of grids and another length of 18 cm, over which electrons may be either accelerated or retarded. Retarding results in higher resolution, while acceleration allows electrons with lower kinetic energy to be studied. The time-of-flight technique has good sensitivity because electrons of all energies are collected at once. The analyzer resolution results mainly from the size of the interaction region and is $\Delta E/E = 0.02$ (0°) and 0.03-4 (55°). The transmission of the time-of-flight analyzers is nearly constant down to a kinetic energy of ~ 20 eV, where it begins to decrease.

The experiments described in chapters IV-VI were performed with a threshold electron analyzer using time-of-flight, which is shown in Fig. 3. A schematic diagram is found in Fig. 1 of chapter IV. The motivation for constructing this analyzer was to measure the intensities of satellite transitions at and near threshold. At that time, only a single satellite He n=2 had been observed at zero kinetic energy.[7] Threshold analyzers, which have both high resolution and high sensitivity, are particularly suited to the study of satellite spectra, which contain a number of weak lines. The threshold analyzer described below is most similar to that of Baer et al.[8] While having quite high resolution at 0 eV, the resolution of their analyzer degrades rapidly with increasing energy, to $\Delta E \sim 1$ eV at 2 eV. By lengthening the flight distance from 15 mm to 215 mm, we hoped to have good resolution over the kinetic energy range from 0 to 10 eV.

The remainder of this chapter will follow, in an approximately chronological way, work that began in the fall of 1983 and ended in the summer of 1985. In order to choose flight distances and aperture sizes, various properties of a threshold analyzer were calculated analytically, and ray tracing was performed. Then the rest of the analyzer was designed, including the gas jet and magnetic shielding. Drawing and assembly were followed by nearly one year of testing and modification, made more difficult by insufficient beam time. In order to store an electron energy spectrum while the photon energy is scanned, a FORTRAN program called TEA was written. Finally, a second version of the threshold analyzer was constructed for the experiments in chapter IV performed in collaboration with the U. Becker group at HASYLAB.

Referring to the photograph in Fig. 3, the synchrotron radiation (moving into the figure) and gas intersect beneath the top, reflecting grid. Photoelectrons travel through three regions as shown in Fig. 1 of chapter IV: the extraction region ($d_e \sim 5$ mm, i.e. from the center to the entrance grid), the acceleration region ($d_a = 18$ mm), and the drift region ($d_d = 192$ mm). The flight time of the electron depends on these distances and on the extraction ($E_e = 2.2$ V/cm) and accelerating ($E_a = 3.8$ V/cm) fields in the following way:

$$t(U_0,d_e) = t_e + t_a + t_d, \qquad (1)$$

where $U_0$ is the initial electron kinetic energy and $d_e$ is considered to vary depending on where the electron starts in the interaction region. The rather large interaction region is mainly defined by the width of the synchrotron radiation beam from the "grasshopper" monochromator ~ 2x2 $\text{mm}^2$ and by the diameter of the entrance aperture 6.6 mm.

$$t_e = \frac{\sqrt{2m}}{qE_e}\left(\sqrt{U_0 + d_e q E_e} \pm \sqrt{U_0}\right), \qquad (2)$$

where m and q are the electron's mass and charge, and the ± considers electrons initially moving away from or toward the detector. For kinetic energies less than the reflector voltage, two peaks are observed separated by the time for an electron to move from the interaction region toward the reflector and then to return to its starting point. Similarly,

$$t_a = \frac{\sqrt{2m}}{qE_a}\left(\sqrt{U_0 + d_eqE_e + d_aqE_a} - \sqrt{U_0 + d_eqE_e}\right). \qquad (3)$$

$$t_d = m^{1/2}d_d[2(U_0 + d_eqE_e + d_aqE_a)]^{-1/2}. \qquad (4)$$

These equations are identical to those for a time-of-flight mass spectrometer with extraction and acceleration regions.

For high time (energy) resolution, the space-focussing condition must be satisfied at the center of the interaction region,[9]

$$\frac{dt}{dd_e} = 0. \qquad (5)$$

An electron from the far side of the interaction region is accelerated more, while an electron from the near side travels a shorter distance. With the correct distances and voltages, both electrons reach the detector with the same flight time. For our analyzer parameters, the space-focussing condition is satisfied for electron kinetic energies between 0 and 10 eV. When considering a source of width 4 mm, the time differences are at most 0.5 ns.

To choose all the distances and voltages, additional criteria must be considered. The total flight distance was limited by the dimensions of the existing vacuum chamber, originally built for the double-angle time-of-flight measurements. In addition, the duty cycle of SPEAR in the 4x1 mode ($\Delta t$ = 195 ns) suggested a flight time of 150 ns for 0 eV electrons.

The transmission function of a threshold analyzer is a consequence of the weak extraction field. For very low kinetic energies, here 0 - 0.03 meV, all electrons are collected by the detector, whose active area is determined by the anode radius $r_a$ of 14.2 mm. With increasing kinetic energy, the transmission function decreases steeply. The transmission may be calculated from the flight time (Eqns. (1)-(5)) and from the constant transverse velocity with which an electron will just hit the edge of the anode. The acceptance half-angle δ and transmission T are given to a good approximation by:

$$\delta = \sin^{-1}\left(\frac{r_a\sqrt{m}}{t\sqrt{2U_0}}\right) \qquad (6)$$

$$T = \frac{1}{2}\,(1 - \cos\delta). \qquad (7)$$

The solid line in Fig. 4 shows the calculated analyzer transmission function convoluted with a gaussian 0.2 eV wide representing the monochromator bandpass. At threshold, the transmission has a value well below 100 % because of the monochromator resolution. The moderate resolution of the soft x-ray monochromators not only broadens the threshold peaks, but actually decreases their intensity at a constant photon flux. At low kinetic energies, the transmission of angle-resolved electron analyzers is significantly lower. For example, our other time-of-flight spectrometers[6] collect δ of 3°, which correponds to a transmission of 0.07 %, below the abscissa in Fig. 4. This comparison should be qualified by noting that the threshold measurement benefits less from the multichannel nature of time-of-flight since only the low kinetic energy part of the spectrum is useful. A disadvantage of the strongly varying transmission function is the resulting uncertainty in the calibration for intensity measurements. To overcome this difficulty, photon energy scans may be considered where all the peaks are at the same kinetic energy and analyzer transmission.

The observed variation of photoelectron intensities with emission direction is influenced by the analyzer acceptance angle $\delta$. For small $\delta$, the angular distribution of photoelectrons and Auger electrons is described by Yang's theorem:[10]

$$\frac{d\sigma}{d\Omega} = \frac{\sigma}{4\pi}\,[1 + \beta P_2(\cos\theta)], \qquad (8)$$

where $\beta$ is the angular distribution asymmety parameter, $P_2$ the second Legendre polynomial, and $\theta$ the angle between the analyzer axis and the photon electric field vector. Here, the dipole approximation, a randomly oriented sample, and 100 % linearly polarized light have been assumed. For large angular acceptance, one must integrate Eqn. (8) over $d\Omega$. First, the coordinates are rotated by $\theta$ about $\hat{x}$ in order to place $\hat{z}$ parallel to the analyzer axis. In the new coordinate system $(r, \delta', \phi)$,

$$P_2(\cos\theta) \rightarrow \frac{1}{2}[3(\cos\delta'\cos\theta - \sin\delta'\sin\phi\sin\theta)^2 - 1]. \qquad (9)$$

Then integrating over the acceptance cone of the analyzer,

$$\frac{1}{\sigma}\int d\sigma = \frac{1}{4}[2 - 2\cos\delta + \beta\cos\delta\sin^2\delta P_2(\cos\theta)] \qquad (10)$$

As an advantageous consequence of Eqn. 10, $\theta$ of 55° is always a magic angle irrespective of $\delta$. Therefore, the threshold analyzer in Fig. 3, whose orientation is fixed at the magic angle, will measure intensities independent of $\beta$. Angular distribution effects cannot be neglected at angles quite close to the magic angle. For example at 53°, different $\beta$ values can lead to intensity variations of up to 13 %. For the measurement of $\beta$ with a rotatable threshold analyzer, the sensitivity to $\beta$ decreases only slowly with $\delta$.

Ray tracing was performed with the program EBQ written by A.C. Paul primarily for relativistic ion beams. In Fig. 5, equipotential surfaces and electron trajectories are plotted for an idealized geometry. For 4 cm diameter accelerating elements separated by 1 and 2 cm, the effects of fringing fields is quite small. The electrons follow parabolic paths in the extraction and acceleration regions and, of course, linear paths in the drift region. There are flight-time differences, which result from the different emission angles, of which $\delta'$ from 0° to 50° are shown in Fig. 5 for $U_0 = 0.1$ eV. The time dispersion among 0.1 eV electrons that reach the detector is 0.7 ns. Because of the narrowing acceptance angle $\delta$, this time width decreases with increasing energy. Starting the electron rays from different positions in the interaction region leads to small time differences in agreement with the one-dimensional calculation.

The effects of a grid on electron flight paths were examined by considering a small portion of 100 lines/in. mesh of 0.001 in. wires. The volume, a cylinder of 0.05 in. radius and length, was limited by the maximum number of points allowed by EBQ. Before the grid, electrons are accelerated, while on the far side lies a drift region. First of all, 10 % of the electrons are lost from physically hitting a wire. The other electrons are deflected, especially if they pass close to a wire. However, the calculated deflections are small, ~ 1°, which results in an additional transmission loss of ~ 8 % and in negligible time differences of ~ 0.1 ns. On the other hand the artificial boundaries of the small volume enhance the uniformity of the electric field. In the threshold analyzer electrons pass through three grids, all Cu 20 lines/in. The observed photoelectron peaks are asymmetrically broadened on the low kinetic energy side, which would be reduced by replacing the grids by open apertures. A disadvantage of apertures is that electrons starting from the sides of the interaction region are accepted in a very asymmetric way. For electrons starting with 0.1 eV kinetic energy from an initial position 2 mm above the analyzer axis, initial emission angles from -17° to -8° with respect to the analyzer axis are collected.

Various components of the threshold analyzer will now be described. The openings of the grid-apertures and of the two collimators in the drift region were chosen by considering a finite source volume and the minimum kinetic energy to fill the detector. A 32 meV electron starting 2 mm off-axis and moving initially in the perpendicular direction will just miss the edge of all the apertures. The resulting aperture diameters are large, 6.6 mm for the first and smallest grid-aperture. This aperture size should be compared with the aperture of our other time-of-flight analyzers, with a diameter of 2.4 mm.[4] Since a larger interaction region is viewed by the threshold analyzer, the sensitivity should be enhanced. On the other hand, the differential pumping, provided by a 500 l/s Airco turbo pump mounted below the analyzer, is somewhat compromised by the large aperture openings. In addition, there is a small gap at the wall of the magnetic shielding cylinder. The grid-apertures are constructed from thin Al sheet (0.016" thick) to avoid focusing effects.

The detector is in many respects identical to that of our other time-of-flight analyzers.[6] It consists of a pair of Varian 40 mm microchannel plates and an anode. The conical anode has a resistance that increases from 16 Ω in front to 50 Ω in back and is followed by a transformer, which decouples the signal from high voltage to gound potential. The pulses' leading edge have fall times of ~ 1 ns. The pulse heights are on the order of 50 mV. The channel plate stack was modified in order to make it easier to disassemble and put together. The contact rings were etched from 0.005" Cu sheet. A slotted Lexan ring keys on the anode shield, while having an inner diammeter which aligns the microchannel plates and contact rings. Finally, the anode and channel plate stack can be remove from the analyzer.

Magnetic shielding is provided by an annealed mu metal cylinder with 4" O.D. and 0.060" wall thickness. An estimate of the effect of a magnetic field may be obtained by considering the motion of an electron with constant energy. This electron will follow a circular path in a plane ⊥ to B with a radius given by,

$$r = \frac{mv}{Bq} \tag{11}$$

For example, a 7 eV electron moving in a 10 mG magnetic field is deflected by 2 mm over a 20 cm flight path. After putting a cuff over the 2" diameter hole opposite the gas-inlet needle, the residual magnetic field was less than 20 mG. Although three pairs of Helmholtz coils were constructed, a significant effect was not observed in the electron spectra. The Helmholtz coils were used only once.

In order to preserve the uniformity of the electric field in the interaction region, a thin needle is used as the gas source. A stainless steel tube (0.065" O.D.) is employed. At the end, a brass plug with a 0.006" diameter orifice simply increases the backing pressure. The peaking of this gas source was determined by measuring the electron count rate while moving the gas inlet $\perp$ to the analyzer axis. The peaking is only moderate: $\theta_{1/2}$, defined by $I(\theta_{1/2})/I(0°) = 0.5$, is 40°. However, this performance is somewhat better than that of the microchannel array gas inlet,[6] for which $\theta_{1/2}$ was measured to be 50°.

The timing electronics are the same as used for the other time-of flight experiments.[6] An additional low voltage power supply, using operational amplifiers, provides the voltages for the accelerating elements. The timing pulses from the anode are amplified (x9) and discriminated before being sent to a time-to-amplitude convertor (TAC) as a start. A reference timing signal from an inductive coil in the storage ring provides a stop. The pulse height spectrum is accumulated in a Canberra Series 40 multi-channel analyzer (MCA) and is then read into a Digital Equipment Corp. (DEC) LSI-11/23 computer. Peripherals of the computer include a Hewlett Packard 7220C xy plotter and a DEC RL02 hard disk drive with 10 Megabyte removable disks.

A program called TEA was written to perform the data acquisition. At each photon energy point, the following data must be read and stored: a spectrum of electron counts vs. flight time and the photon and pressure scalars. The photon scalar is derived from a sodium salicylate scintillator and photomultiplier tube. The pressure scalar monitors the pressure behind the gas needle. During a scan, which typically lasts one hour, the experimenter must be able to follow the scan's progress.

The TEA program has the capability for drawing graphs on the HP plotter, for converting energies to time channels, and for performing simple integrations. In addition, a scan may be interrupted.

The facility for running dual tasks is achieved by poling. After a delay equal to the point collection time, a completion routine sets a logical variable READY to be true. At various times while, for example, TEA might be plotting, the program checks the value of READY. If READY is true, the secondary process is interrupted until the primary task of storing the completed spectrum and beginning the next one has been carried out. The running of two tasks at the same time may be achieved more naturally by using the RT 11 foreground/background monitor.

The "grasshopper" monochromator is controlled by the program SPECTR, which is provided and supported by SSRL. In the READEXTERNAL mode, SPECTR waits passively for the characters 'E,' followed by a real number which is the next requested photon energy. After the monochromator motion has been completed, SPECTR sends the character 'F.' As a result of the dead time needed by SPECTR in the READEXTERNAL mode, the collection time per point must be at least 10 s.

At each scan point, a series of seven, primary steps are performed. First, a time spectrum (limited to a maximum of 501 channels) is transferred from the MCA to computer memory. Then, the photon and pressure scalars are read. To save disk space and time, the real data array is first converted into integer numbers and then written into a file as an unformatted block (or two blocks). The TEA program now sends SPECTR the request for the next photon energy. After receiving the 'F' character in return, the scalars and MCA are cleared. The MCA is then placed on collect, which through a gating signal also starts the scalars. Finally, the completion routine is set to run after the collection time has elapsed. The execution of these steps takes less than 2 s, in general.

Initial testing of the threshold analyzer occurred over a four day period at the end of the April 1984 dedicated run. This length of time was enough to characterize in part three problems and to identify one solution. First, the synchrotron beam would not pass cleanly through the analyzer. A diffuse component of the beam, probably caused by scattering from the Si window, hit the metal surfaces of the analyzer causing a large background. By positioning a 0.125" diammeter aperture in front of the analyzer, this unwanted signal was minimized. When gas sample was introduced, however, a new, intense background signal arose, that was not flat. This new background signal was interpreted as being caused by high energy electrons hitting the surfaces of the analyzer. Finally, the analyzer transmission was observed to decrease at kinetic energies below 5 eV. We realized later that the transmission losses were at least in part caused by the analyzer power supply common floating with respect to the ground of the chamber and gas needle.

The April run was followed by seven months without beam time. Additional testing took place in Berkeley with a Varian LEED/Auger electron gun modified for timing. Pulses of ~ 15 V from a Tektronix PG508 pulse generator were sent to one of the deflectors of the electron gun. At electron beam energies of 100-200 eV, the electron gun delivered pulses of 2-3 ns width. Because the electron energy loss may have any value, background cannot be effectively studied with the electron gun.

A number of modifications of the analyzer were made. The uniformity of the electric fields in the extraction and acceleration regions was improved. A cuff was added to the magnetic shield. In order to make alignment easier as well as to improve the background, two fixed apertures were mounted on the chamber bottom flange. In Berkeley, a careful allignment was done with a laser so that the synchrotron radiation centered on the front and back apertures will pass through the center of the analyzer. The solid disk reflector was replaced with a grid. The metal surfaces of the analyzer, which were originally gold plated, were painted with colloidal graphite.

The present performance of the threshold analyzer can be seen in Fig. 4 as well as in the various spectra shown in chapters IV-VI. The background has been reduced to a sufficient extent that transitions with $\sigma < 1$ kb have been observed. The filled circles in Fig. 4 show the analyzer transmission inferred from the measured intensity ratios of the He n=2 satellite at low kinetic energy and the He 1s. For the He 1s peak the calculated transmission at high kinetic energy was assumed. The observed and calculated transmission agree well. That the measured transmission appears somewhat higher suggests that the effective source volume at low kinetic energies is larger than at high kinetic energies.

The highest resolution was achieved in the Ar threshold scan in chapter VI, where the 3s peak has a 0.085 eV width, of which the analyzer contributes an estimated 0.055 eV. This resolution at 0 eV kinetic energy is inferior to the upper bounds of 0.020 eV reported by

Baer et al.[8] or 0.028 eV quoted by Stockbauer.[11] Improvements in our resolution could probably be realized by integrating the electron counts over a smaller time window or by using lower extraction and acceleration voltages. However, in the experiments described in this thesis, the monochromator bandwidth was comparable to that of the analyzer. Therefore, the gain from improved analyzer resolution would be small and could not offset the loss in transmission.

The goal of satisfactory resolution over the kinetic energy range from 0 to 10 eV has also been achieved. The open circles in Fig. 4 represent the full width at half maximum (FWHM) of the He n=2 satellite peak. Near threshold, the observed FWHM in the time spectra is caused by the form of the transmission function. From 0.2 eV to 2 eV kinetic energy, the main contribution to the FWHM is the monochromator resolution, which is estimated to be 0.2 eV. Above 2 eV, the resolution of the threshold analyzer contributes significantly. The worsening of the analyzer resolution follows the compression of the time scale as the kinetic energy increases. A time resolution of 1 ns corresponds to an energy width of 0.2 eV at 5 eV kinetic energy, but of 0.4 eV at 10 eV kinetic energy. Improved resolution at the higher kinetic energies requires a longer flight distance.

For the He and Ne threshold experiment described in chapter IV, a second version of the threshold analyzer was constructed to be compatible with the Becker group's chamber. Since their chamber is rotatable, angular distributions near threshold could be measured. There are a number of small differences between the two threshold analyzers. The second version has a longer flight distance of 285 mm.

From outside the chamber, the gas needle may be moved in one dimension. The magnetic shielding is provided by two concentric cylinders of 0.025" thick mu metal. Finally, the TEA program could not be used with the TGM program. Instead, three scalars were read: two counting electrons arriving in different kinetic energy windows and a third monitoring the photon intensity.

## REFERENCES

1. H. Winick, in Synchrotron Radiation Research, H. Winick and S. Doniach, eds. (Plenum, New York, 1980).
2. F.C. Brown, R.Z. Bachrach, and N. Lien, Nucl. Instrum. Meth. **152**, 73 (1978).
3. B. Pate, Ph.D. Thesis, Stanford University (1984).
4. R. Bruhn, E. Schmidt, H. Schröder, B. Sonntag, A. Thevenon, G. Passereau, and J. Flamand, Nucl. Instrum. Meth. **208**, 771 (1983).
5. D.W. Lindle, T.A. Ferrett, P.A. Heimann, and D.A. Shirley, Phys. Rev. A **34**, 1131 (1986).
6. M.G. White, R.A. Rosenberg, G. Gabor, E.D. Poliakoff, G. Thornton, S.H. Southworth, and D.A. Shirley, Rev. Sci. Instrum. **50**, 1268 (1979); M.G. White, Ph.D. Thesis, University of California, Berkeley (1979), Lawrence Berkeley Laboratory report No. LBL-9527.
7. P.R. Woodruff and J.A.R. Samson, Phys. Rev. Lett. **45**, 110 (1980).
8. T. Baer, P.M. Guyon, I. Nenner, A. Tabche-Fouhaille, R. Botter, L.F.A. Ferreira, and T.R. Govers, J. Chem. Phys. **70**, 1585 (1979).
9. W.C. Wiley and I.H. McLaren, Rev. Sci. Instrum. **26**, 1150 (1955).
10. C.N. Yang, Phys. Rev. **74**, 764 (1948).
11. R. Stockbauer, Int. J. Mass Spectrom. Ion Phys. **25**, 89 (1977).

## FIGURE CAPTIONS

Fig. 1 A diagram showing the electron storage ring, monochromator and photoelectron spectrometer. In the time-of-flight method,time differences are measured between the synchrotron radiation pulse and the arrival of the electron at a detector.

Fig. 2 The relative photon intensity (solid curve) from the "grasshopper" monochromator (1200 l/mm grating) which is transmitted through a 1500 Å thick Si window. For the dashed curve the intensity has been divided by $(h\nu)^2$ to give the intensity for a unit energy interval. The sodium salicylate scintillator, which monitors the photon flux, has an efficiency which increases by 80 % between 100 and 270 eV photon energy, in an approximately linear way.[5]

Fig. 3 A photograph of the threshold electron analyzer. At the top is the extraction region with the acceleration and drift region below. The conical anode can be seen through the support beams.

Fig. 4 The threshold analyzer performance as determined by the measurement of $He^+$ 1s and n=2 photoelectrons. The experimental transmission (filled circles) is compared with a calculated curve. The observed resolution of the analyzer is shown with open circles.

Fig. 5 A plot from the program EBQ showing electron paths and equipotential surfaces. The cylindrically symmetric configuration has a reflector at 0 V separated by 2 cm from the first grid at 4V which is spaced by 1 cm from the drift region at 14 V. The initial kinetic energy is 0.1 eV.

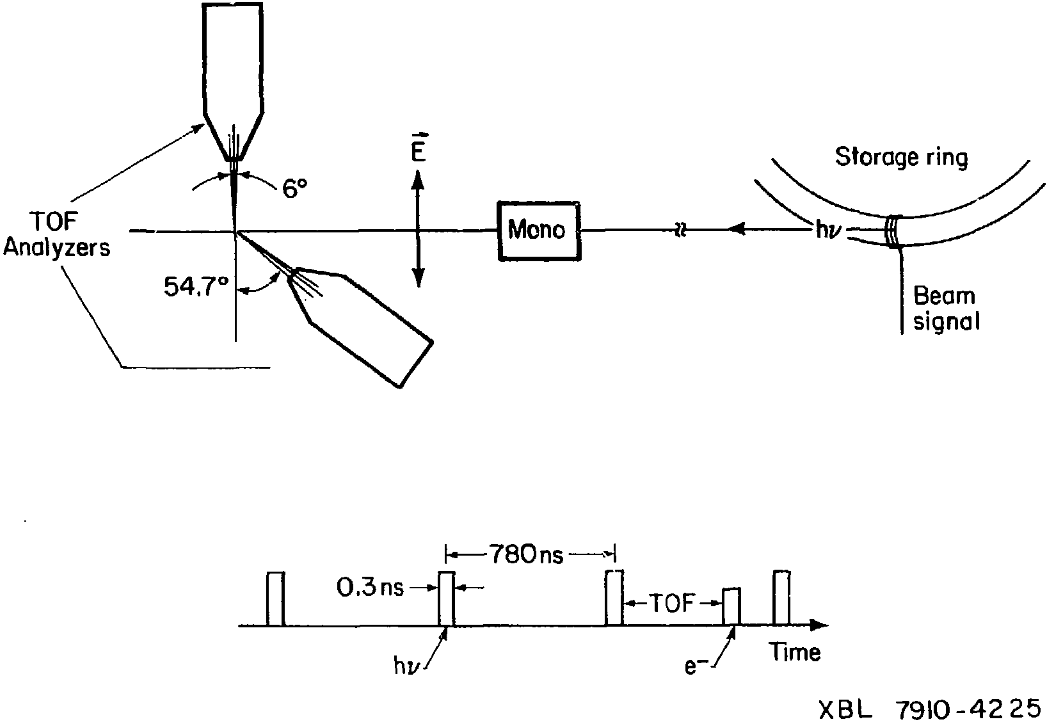
TOF
Analyzers
6°
54.7°
E⃗
Mono
Storage ring
hν
Beam
signal
780ns
0.3ns
TOF
hν
e⁻
Time
XBL 7910-4225

Figure 1

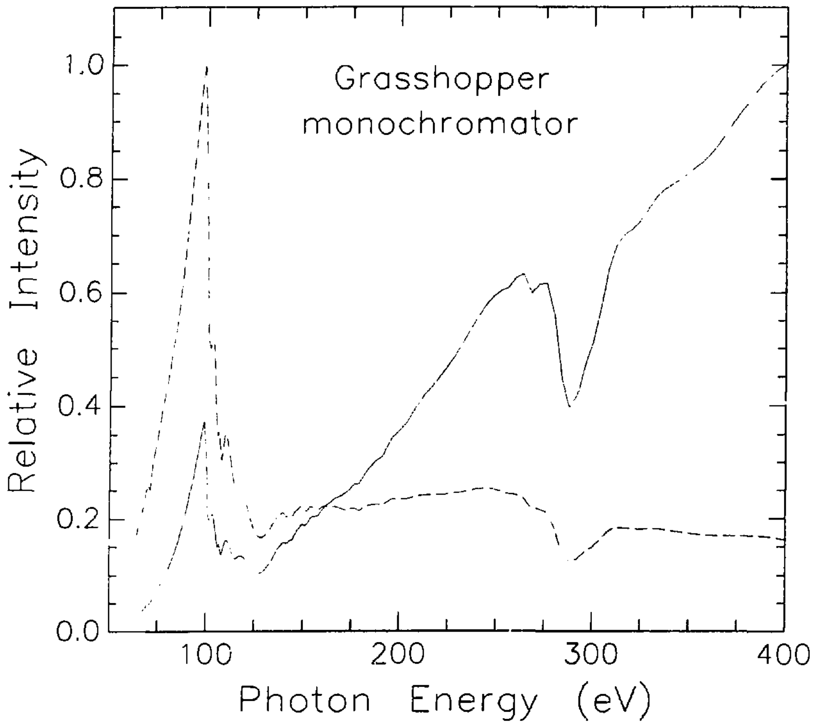

XBL 8611-4316

Figure 2

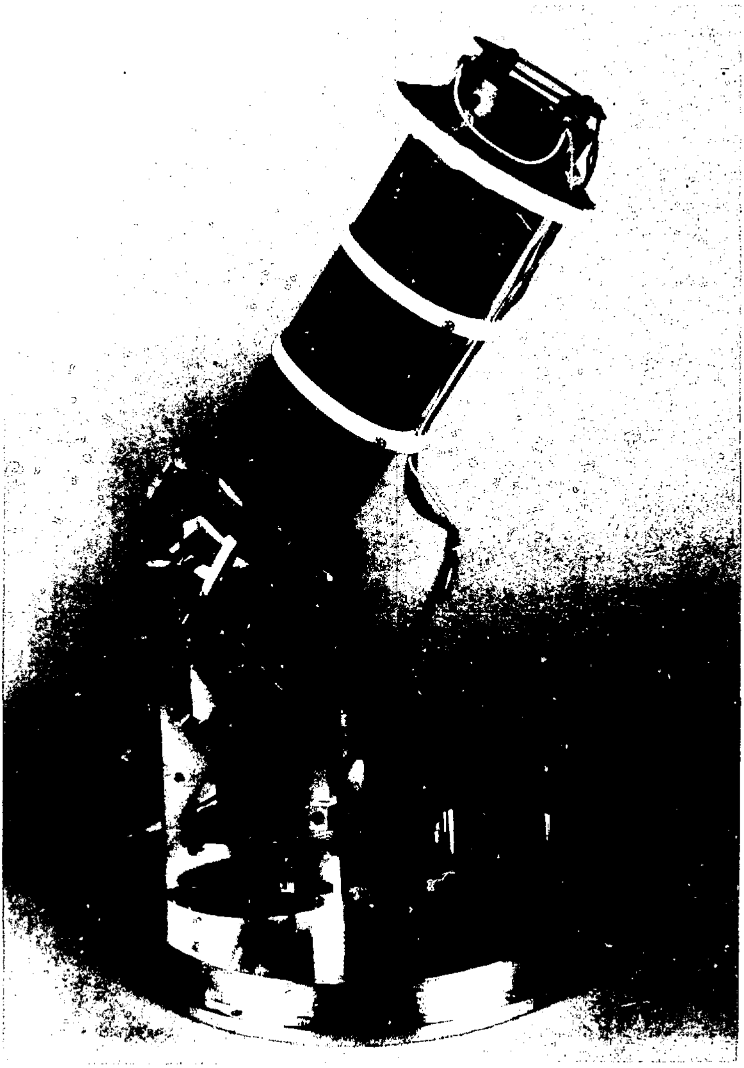

CBB 857-5407

Figure 3

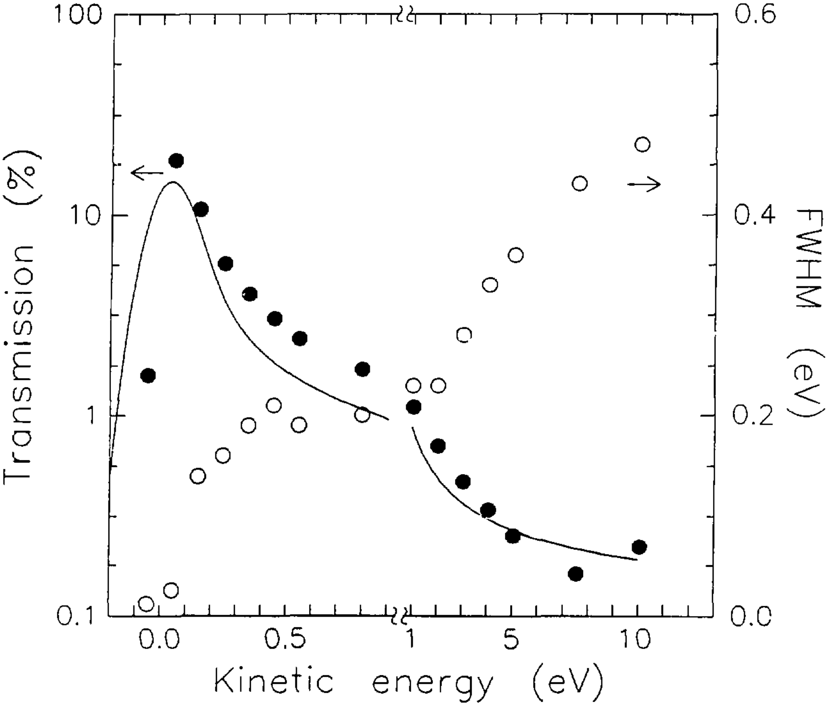

XBL 8611-4317

Figure 4

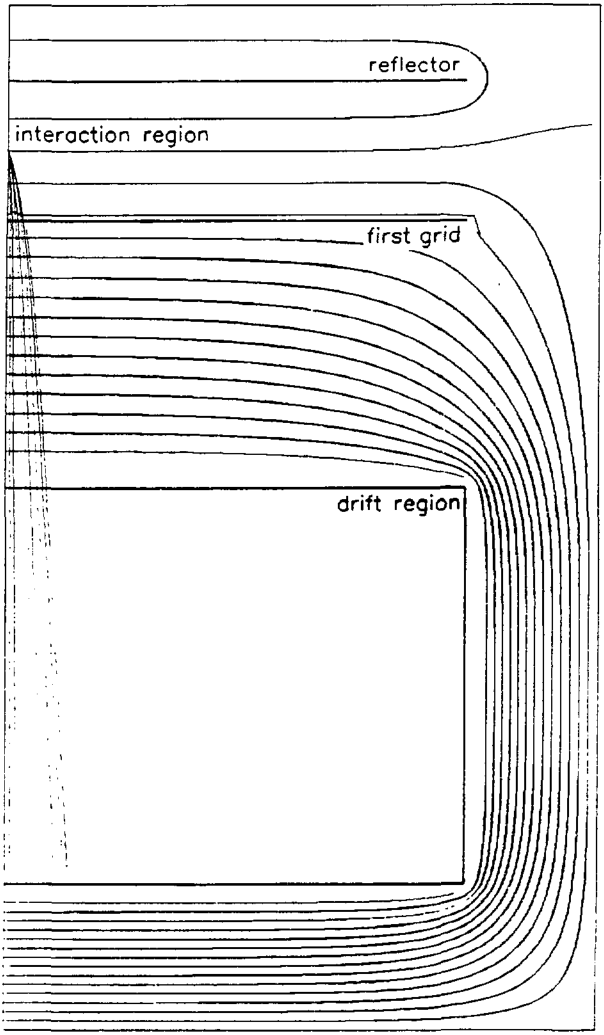

XBL 8611-4315

Figure 5

# III. THE VALENCE PHOTOELECTRON SATELLITES OF NEON*

## ABSTRACT

Synchrotron radiation was directed at neon gas, creating $Ne^+$ ions in "satellite" states characterized by the configurations $1s^22s^22p^4nl$, in addition to the main line final states: $2s^{-1}$ and $2p^{-1}$. Satellite features appearing in the photoelectron spectrum were studied in the near-threshold region with photon energies from 55.2 to 99.7 eV. For three of the satellite peaks, the angular distribution asymmetry parameter, $\beta_i$, varies with kinetic energy in much the same way as the asymmetry parameter of the 2p line. None of the satellites have a $\beta_i$ like that of the 2s line. All the satellite partial cross sections, $\sigma_i$, have kinetic energy dependences similar to the partial cross section of the 2p main line. However, the $\sigma_i$ curves are not identical, and some deviation from the 2p intensity behavior is observed. These $\beta_i$ and $\sigma_i$ results are used to confirm the previous assignments of the satellite final states in neon and to consider, in general, the energy-dependent behavior of satellites near threshold.

## A. INTRODUCTION

In simple systems such as atomic neon, the photoelectron spectrum is dominated by intense peaks associated with the removal of a single electron from the nominal ground-state configuration of the parent atom; e.g.,

$$\mathrm{Ne}(1s^2 2s^2 2p^6;\ {}^1S) \rightarrow \mathrm{Ne}^+(1s^2 2s^2 2p^5;\ {}^2P_{1/2,3/2}) + e^- .$$

These "main" peaks are analogous to the "diagram" lines in x-ray spectra.

Also present, usually with much lower intensity, are "satellite" peaks, which fall at higher binding energies than the main peaks. For heuristic reasons these satellites have been called "shake-up" peaks, because their dominant configurations could be accessed in a hypothetical two-electron excitation process; e.g.,

$$\mathrm{Ne}(1s^2 2s^2 2p^6) + h\nu \rightarrow e^- + \mathrm{Ne}^+(1s^2 2s^2 2p^4 n\ell) .$$

Here one 2p electron would undergo photoejection, and another would simultaneously be "shaken up" into the n  orbital by the changing Coulomb field. In this approximation the satellite intensity can be estimated as being proportional to the square of the overlap matrix element between the passive electrons in the initial and final states; i.e., excluding the initial and final orbitals of the photoelectron.[1]

A more general theoretical approach takes electron correlation into account and employs multi-configuration wave functions in both the initial and final states.[2] The satellite peaks are then associated with "correlation states," which are accessed by the same process that gives rise to the main peak. This approach restores the qualitative equivalence of the ionic "main" and "satellite" states and liberates the latter from their dependence on being created through the somewhat artificial "shake-up" process. Using a single configuration initial state and a multi-configuration final state, Dyall and Larkins[2,3] have calculated the binding energies and high energy intensities of the neon valence satellites.

These theoretical approaches have been adequate for providing an understanding of the existing satellite data measured with fixed-energy laboratory-based photon sources. The majority of correlation-satellite studies have been addressed to the energies of satellite peaks and to their intensities in the high energy (sudden) limit. A notable exception is an early paper on neon by Wuilleumier and Krause,[4] in which these authors used laboratory sources at several fixed energies to do pioneering studies of the kinetic energy ($\epsilon$) dependence of satellite cross sections $\sigma_i$ and angular distribution asymmetry parameters $\beta_i$. Wuilleumier and Krause noted that studies of $\sigma_i(\epsilon)$ and $\beta_i(\epsilon)$ should yield insights into the symmetry of the correlation satellite states and the mechanism by which they are populated. They also considered the useful concept of the relative excitation energy, $\epsilon/E_0$, where $E_0$ is the energy separating the correlation state from the main-line state. The ratio $\epsilon/E_0$ can be regarded qualitatively as an adiabaticity parameter.[1]

With the availability of synchrotron radiation, there now exists the capability of controlling $\epsilon$ continuously. Of special interest is the possibility of making measurements of $\sigma_i(\epsilon)$ from the adiabatic regime, just above threshold, to the high $\epsilon$ sudden limit. Additional information can be gained by measuring $\beta_i(\epsilon)$ through the range of $\epsilon$ in which $\beta$ of the main line exhibits its characteristic variation: in the neon case, near threshold, where $\beta_{2p}$ varies greatly. In this paper we report a synchrotron-radiation study of the neon 2s, 2p satellites in which $\sigma_i(\epsilon)$ and $\beta_i(\epsilon)$ were measured through the range between $\epsilon \approx$ 3-6 eV and $\epsilon \sim$ 40 eV (between $\epsilon/E_0 \approx 0.1$-$0.2$ and $\epsilon/E_0 \sim 1.2$). Parallel experiments have examined the outer shell satellites of other atoms: He[5], Ar[6], and Xe.[7]

The experiment and data analysis are described in Section II. The spectral peak assignments are discussed in Section III. Section IV is devoted to the angular distribution results, and Section V to the partial cross sections. Finally, Section VI contains the conclusions.

## B. EXPERIMENTAL

This experiment was performed at the Stanford Synchrotron Radiation Laboratory (SSRL) using a grazing incidence "grasshopper" monochromator with a 1200 line/mm grating. A 1000Å thick Si window isolated the monochromator vacuum from the experimental chamber. During the experiment the background pressure of the chamber was about $5\times10^{-4}$ torr. We estimate that the pressure in the interaction region was approximately a factor of 10 higher.

Photoelectrons were analyzed by the time delay between the synchrotron light pulse and the arrival of the electrons at one of two detectors. This method has been described elsewhere.[8,9]

The simultaneous measurement at two angles, $\theta = 0^\circ$ and $54.7^\circ$, yields the reported quantities $\beta_i(\varepsilon)$ and $\sigma_i(\varepsilon)$ from Yang's theorem:[10]

$$\frac{d\sigma_i(\varepsilon,\theta)}{d\Omega} = \frac{\sigma_i(\varepsilon)}{4\pi} [1 + \beta_i(\varepsilon)P_2(\cos\theta)] . \qquad (1)$$

Here the subscript i denotes a particular satellite peak, and $\theta$ is the angle between the photon electric vector and the photoelectron propagation direction. The dipole approximation, a randomly oriented sample, and linear polarized light have been assumed. A high degree of polarization P has been estimated for the "grasshopper" monochromator,[9] and the resulting uncertainty in $\beta_i$ should be relatively small, less than 0.1 for $P \approx 90$ percent. The intensities measured provide branching ratios of the satellite peaks with respect to the 2s line, $\sigma_i/\sigma_{2s}$. All the intensity ratios presented here compare two transitions at the same photon energy. To obtain $\sigma_i$ the satellite to 2s ratio was multiplied by $\sigma_{2s}$ from Wuilleumier and Krause.[11]

For calibration, the transmission of the 54.7° analyzer and the relative efficiencies of the two analyzers were evaluated from the measured intensity of the 2s peak in combination with the literature cross section,[11] and the known value of $\beta_{2s} = 2$. The transmission function was corrected for changes in the light intensity, the percentage of higher-order light components, and the gas pressure.

To determine the peak areas and binding energies, the time-of-flight spectra (which were linear in time) were converted to a linear energy scale. Using a least-squares program, the satellite peaks were then fitted to Gaussian functions. Figure 1 displays the fit of a converted spectrum. The unresolved satellites 6 and 7 were fitted to 2 Gaussians separated by a fixed 0.55 eV, the approximate difference in binding energies. An exponential tail was combined with the Gaussian for the 2s peak, which was asymmetrically broad on the low kinetic energy side. For the background the sum of two functions was used: the first being constant in energy, and the second constant in time, varying as $\epsilon^{-3/2}$. The binding energies were determined from the separation between the satellites and the 2s main line, which has a binding energy of 48.48 eV.[12,13]

The error bars provided for the $\sigma_i(\epsilon)$ and $\beta_i(\epsilon)$ data in this work represent either the standard deviations of the fits or the agreement between different spectra taken at the same photon energy. For the most important systematic error, that resulting from the calibration procedure, we estimate the uncertainty in $\beta$ to be 0.1 and the uncertainty in the branching ratio to be 5 percent. At the lowest kinetic energies, 5 eV or less, the calibration error increases to about 0.15 in $\beta$ and to 10-20 percent in the branching ratio.

## C. THE ENERGY SPECTRUM

The spectrum shown in Figure 1 was accumulated in 3000 sec with an accelerating voltage of 13 volts. The numbers labeling the satellite peaks follow the notation of Wuilleumier and Krause[4] and will be used throughout this discussion. Our total experimental resolution can be seen, for example, in the observed width of the satellite peak 7, which is 0.41 eV FWHM. Convoluted in this width is the monochromator bandwidth, estimated to be 0.33 eV.

For the satellites appearing in this spectrum, Table 1 lists our binding energies along with the final ionic states as assigned by Dyall and Larkins[3] and with the energies from emission spectroscopy.[12] Wuilleumier and Krause identified several other peaks with very low intensity. With an improved signal-to-background ratio, we do not observe peaks 5, 8 (attributed by them to 2p electrons having undergone two inelastic collisions), 9, and 12. Dyall and Larkins could not find assignments for these features, either.

At photon energies above 66 eV, satellites 1 and 2 are observed. Because of their low intensity, only a brief description of their behavior will be given here. Satellite 1 has a $\beta_i$ of 0.3(3) and a branching ratio with respect to the 2s main line of 2.3(3) percent, averaged over energy. For satellite 2, $\beta_i$ increases from about 0 at 10 eV kinetic energy to about 1 at 35 eV. Similarly, the branching ratio of satellite 2 rises from approximately 1.5 to approximately 3 percent over the same energy range.

For two of the peaks appearing in Fig. 1, their shape implies some partly hidden structure. First, satellite 6 appears as a shoulder on the low kinetic energy side of satellite 7. In the 54.7° spectrum at 64.1 eV, satellite 6 is more prominent. Secondly, satellite 3 is always unnaturally broad. Figure 2 displays the satellite peak widths from five similar spectra. The larger width of satellite 3 probably results from the summing of significant contributions from more than one of the final states listed in Table I. Comparison of the binding energy of satellite 3 with the energies of these final states suggests that one or more of the $(^1D)3d$ states should be an important component in this peak.

At this point some qualitative observations can be made about the satellite spectrum as a whole. First, all but the weakest lines can be assigned to configurations containing an excited orbital n with n=3. Therefore, processes leaving the $Ne^+$ ion with higher values of n seem to be less important. Secondly, final states of the form np $^2P^o$ are more important than those of the type ns $^2S$ or nd $^2S$. In other words, satellites of the 2p main line are more important than those of the 2s line. This result, which will be confirmed in the following section by the $\beta_i$ curves, is expected because the 2p channel is much more intense than the 2s in this energy range. In fact, the branching ratio $\sigma_{2p}/\sigma_{2s}$ varies from 28 at 55 eV to 10 at 100 eV.[11] Having made separate calculations for the $^2S$ and $^2P^o$ manifolds, Dyall and Larkins assumed that the 2s and 2p satellites would be scaled by the main line branching ratio of the 2s and 2p cross sections. This argument implies that at high photon energy, i.e. 1 keV or more, satellites of the 2s peak should dominate over the 2p satellites. In Ar, Kr, and Xe a dissimilar situation exists because of the unusually strong interaction between the $nsnp^6$ and $ns^2np^4nd$ configurations.[3]

## D. ANGULAR DISTRIBUTIONS

A complete assignment from the energy spectrum alone would require a degree of resolution unobtainable by the present or by earlier studies, and beyond the accuracy of theory. As seen in Table I, there are too many final states, too closely spaced. However, the angular distribution asymmetry parameters can provide additional information. Manson and Starace[14] applied the angular momentum transfer formalism to the term dependence of angular distributions. Assuming LS coupling, they showed that for certain transitions all final states with the same $^{2S+1}L$ must have identical $\beta_i$ parameters. Applying these rules to Ne, the $^2S$ main line and satellite final states must have a $\beta$ value of 2 independent of energy. Similarly, $\beta_i$ is -1 for the $^2P$ states. These geometrical arguments do not restrict the $\beta_i$ variation of the $^2P^o$ or $^2D$ states. However, the same algebraic expression in terms of scattering amplitudes applies to $\beta_i$ of the 2p main line as well as the other $^2P^o$ transitions. While the scattering amplitudes need not be the same, the $^2P^o$ satellites should have $\beta_i$ curves similar to that of the 2p main line.

Table II presents the numerical values of $\beta_i$, and Fig. 3 shows the $\beta_i$ results as functions of kinetic energy for the five satellite peaks. Included in these plots are the $\beta_i$ values obtained by Adam.[15] While confirming the observed trends for the three higher binding energy satellites, Adam's $\beta_i$ results are systematically higher than ours.

For three satellite peaks--4, 6+7, and 10--the observed $\beta_i$ variation with energy is very much like $\beta_{2p}$,[15] though for satellite 10, $\beta_i$ seems to fall somewhat below the $\beta_{2p}$ curve. In the case of satellites 4 and 10, the state assignments in Table I for these $^2P^o$ peaks are strongly supported by the $\beta_i(\varepsilon)$ result. Conversely, this result suggests that even without an obligatory rule from angular momentum and parity considerations, $\beta_i$ for a shake-up satellite will resemble that of its main line. We believe this approximate identity should hold for all satellites having the same term symbol as a main line. In Ar and Xe, Adam et al.[6] and Fahlman et al.[7] have observed that the $(^1D)md\ ^2S$ satellites have $\beta_i$ like $\beta_{ns}$.

For the peak 6+7, consideration of binding energies alone gives an ambiguous identification. The $\beta_i$ results suggest that one of the unresolved final states, $(^1D)3p\ ^2P^o$, is dominant. In the photon energy range of this experiment, the contribution from $(^1S)3s\ ^2S$ should be small because ionization of a 2p electron is much more probable than of a 2s electron. Wuilleumier and Krause[4] measured the angular distribution of peak 7 at photon energies of 132.3 and 151.4 eV. Obtaining a $\beta_i$ value the same as $\beta_{2p}$ within error, they estimated the maximum admixture of $(^1S)3s\ ^2S$ to be 25 percent. Using a similar assumption, namely:

$$\beta_7(\varepsilon) = C_{3s}\ \beta_{2s}(\varepsilon)+C_{3p}\ \beta_{2p}(\varepsilon), \qquad (2)$$

and using $\beta_{2s}=2$ and the literature values for $\beta_{2p}(\varepsilon)$,[11,15] we estimate the contribution of $(^1S)3s\ ^2S$, $C_{3s}$ to be 10 ± 10 percent of satellite 7 in the low $\varepsilon$ range.

The energy dependence of $\beta_i$ for satellites 3 and 11 are quite different from either $\beta_{2s}(\varepsilon)$ or $\beta_{2p}(\varepsilon)$. Satellite 11 is associated with a single final state of symmetry $^2D$, so that the satellite-producing mechanism is not final ionic-state configuration interaction (FISCI). A similar situation exists for helium in the photoelectron channel leading to $He^+(2p)$, for which $\beta_i$ is quite different from that of the He 1s main line.[5]

For satellite 3 several final states are involved. As discussed earlier, the binding energy and broad width of this peak imply both a major contribution from the $(^1D)3d$ final states and the possible presence of additional components. Because $\beta$ for this line is roughly constant, lying midway between $\beta(^2S) = 2$ and $\beta(^2P) = -1$, its intensity may be attributed to an approximately equal admixture of $(^1D)3d\ ^2P$ and $^2S$ final states. The slightly rising slope observed may then be due to a small admixture of $^2P^o$ states. A conclusive decomposition of satellite 3 would require a known $\beta_i$ for the $(^1D)3d\ ^2D$ final state.

## E. PARTIAL CROSS SECTIONS

The primary data, intensity branching ratios between the satellite and the 2s line are shown in Table II. In Fig. 4 each measured ratio has been multiplied by the appropriate literature value of $\sigma_{2s}$,[11] yielding the satellite cross section, $\sigma_i$. To introduce the $\varepsilon$ dependence in the shake model, Smid and Hansen[17] have included the variation of the main-line dipole matrix elements, e.g. $\langle\varepsilon d\ r\ 2p\rangle$. This reasoning suggests that the satellite $\sigma_i$ should resemble $\sigma_{2p}$ at the same kinetic energy, where the continuum wavefunctions $\varepsilon d$ will be most alike.

Several observations can be made from Fig. 4. All the satellites have $\sigma_i(\varepsilon)$ varying similarly to $\sigma_{2p}(\varepsilon)$, but except perhaps for satellite 3, the agreement is not exact. For example, $\sigma_i(\varepsilon)$ for the satellite peak 6+7 exhibits a deviation that demonstrates a breakdown of the shake theory in the low-$\varepsilon$ region. Ironically, $\sigma_i(\varepsilon)$ of satellite 3 shows very close agreement with $\sigma_{2p}(\varepsilon)$. This similarity must be regarded as fortuitous because the $\beta_i(\varepsilon)$ data for this satellite (Fig. 3) disagree strongly with $\beta_{2p}(\varepsilon)$. In addition, Fig. 4 shows that the various satellite $\sigma_i(\varepsilon)$ curves differ, even for those three satellite peaks (4, 6+7, and 10) in which the $\beta_i(\varepsilon)$ data track $\beta_{2p}(\varepsilon)$. We conclude that near-threshold satellite intensities have complicated origins and cannot be simply predicted from main-line curves. Finally, the satellites $\sigma_i(\varepsilon)$ do not display a tendency to approach zero at threshold. This final observation, along with the result that the $\sigma_i(\varepsilon)$ curves are different, stand in conflict with the models of Stohr et al.[18] and Thomas,[19] developed for core-level satellites.[20]

It is of interest to compare our near-threshold satellite intensities with previous work. In Table III our intensities at $\epsilon = 10$ eV and 40 eV are given as branching ratios relative to the 2p main line. Also listed are the measurements at 130 to 150 eV photon energy given by Wuilleumier and Krause,[4] and predicted values from the shake-theory calculation of Dyall and Larkins.[3] The literature values for both $\sigma_{2s}$ and $\sigma_{2p}$ were used to convert our data to the (satellite)/(2p) branching ratio. The precise values of Wuilleumier and Krause are in doubt because of an uncertainty in the normalization given by their Table V.[21] Nevertheless, their results indicate that the sudden-limit intensities of the individual satellites have not been reached at the highest photon energies of our experiment.

The qualitative agreement between the calculated and experimental intensities confirms that Dyall and Larkins' model includes the most important effects. Thus for the neon valence satellites, it appears that the relaxation which accompanies the formation of the hole and correlation in the final ionic state are important mechanisms. In this somewhat artificial division, we consider the change from the atomic to the ionic one electron orbitals separately from the multi-configurational description of the ionic state. These mechanisms may explain the populations of $^2P^o$ and $^2S$ final states, measured to be about 64 and 11 percent of all the satellite intensity, respectively. On the other hand, either initial state (ISCI) or continuum state configuration interaction (CSCI) must be invoked to explain the presence of the $^2D$ and $^2P$ satellites, about 25 percent of the satellite spectrum. By comparison, the intensity variation of satellite 11, $(^1D)3s\ ^2D$, is quite different from that of the He$^+$ 2p satellite in the helium photoelectron spectrum, which is produced mainly by the CSCI process. The He 2p to 1s branching ratio decreases monotonically with increasing energy.[5] Thus the main contribution to satellite 11 may well be initial state configuration interaction. For the 5p satellites in the xenon spectrum, Hansen and Perssen[22] have suggested that initial state correlation plays the main role.

Satellite intensity data over a wider energy range is desirable, but the available data are very limited. For the single case of satellites 6+7 it is possible to extend the data range to $\varepsilon \sim 1.5$ keV, by combining our results with intensities given by Wuilleumier and Krause.[4] The combined data are shown in Fig. 5, plotted against a logarithmic kinetic energy scale. Unfortunately, these data must be interpreted with caution, because the high intensities observed at the three highest kinetic energies may not represent an enhancement of a single satellite process. At these energies, the 2s channel has become stronger than the 2p, and as a consequence the $(^1S)3s\ ^2S$ satellite may dominate over the $(^1D)3p\ ^2P^o$.

Also plotted in Fig. 5 is a curve representing a theoretical treatment of the satellite intensity variation from the adiabatic to sudden limits.[19] This model of Thomas is based on a specific "shake-up" mechanism during the creation of the hole state. The relative intensity ratio $\mu$ is given by

$$\mu = \mu \exp(-mr^2E_0/2\ {}^2E_{ex}), \qquad (3)$$

where m is the electron mass, $E_0$ refers to the energy separation between the satellite and main-line final states, and $E_{ex}$ is the excitation energy of the satellite electron above the <u>main line</u> threshold, i.e., $E_{ex} = E_0+\epsilon$. The adjustable parameters, $\mu$ and r, are the sudden-limit intensity ratio and an effective radius, respectively. For the curve shown in Fig. 5, both parameters were varied to achieve the best reasonable fit with the data ($\mu = 3.7$ percent and $r = 0.78$Å); the highest energy points were excluded from the fit for the reason mentioned above.

With suitable adjustment, the model can be made to fit the data in Fig. 5. However, there are at least two reasons for caution in appraising this agreement. First, the model must be regarded with skepticism at low values of $\epsilon$, because it does not explicitly require energy conservation [$\mu(\epsilon<0) > 0$]. Second, the low-energy behavior of satellites 6+7 cannot be regarded as typical. For comparison, the nearly constant intensity ratio for satellite 10 is included in Fig. 5. Satellite intensity ratios which decrease as kinetic energy increases have been observed in He[5] and Ar.[6] Eqn. (3) cannot provide a universal curve for this complex variety of energy-dependent satellite intensities.

## F. CONCLUSION

We have described the measurement of the binding energies, asymmetry parameters, and partial cross sections for the neon valence satellites. Observing the satellite spectrum at low photon energies, certain types of final state configurations are found to be more important than others. Of the final states with unambiguous parentage, $^2S$ and $^2P^o$, the $^2P^o$ states receive greater intensity, which suggests that the satellites mainly "borrow" intensity from the 2p main line. In addition, the excited orbital is usually in the n=3 shell. For the $^2P^o$ satellites, $\beta_i(\epsilon)$ follows $\beta_{2p}(\epsilon)$ closely. Therefore, as a general rule, a satellite having the same $^{2S+1}L$ as the main line also should have a $\beta_i(\epsilon)$ which tracks the $\beta(\epsilon)$ of the main line. Other satellites may have quite different $\beta_i(\epsilon)$ dependence, as seen from the $\beta(\epsilon)$ results. All $\sigma_i$ approximately imitate $\sigma_{2p}$ as a function of kinetic energy. The observed deviations of $\sigma_i(\epsilon)$ from $\sigma_{2p}(\epsilon)$ remain puzzling. These differences do suggest that the sudden limit has not been reached by $\epsilon \sim 40$ eV ($\epsilon/E_0 \sim 1.2$). Comparison of the experiments with the calculation of Dyall and Larkins[3] confirms the importance of relaxation and FISCI. However, to explain the presence of $^2D$ and $^2P$ satellites, some other mechanism must contribute, such as initial state correlation. The neon valence satellites represent a problem which has been partly solved. Two very useful contributions would be: (1) a measurement of $\beta_i$ at high energy, e.g. $h\nu = 1$ keV, in order to determine the role of the 2s satellites, (2) a calculation of $\sigma_i$ which includes ISCI.

## REFERENCES

*Paper published with co-authors C.M. Truesdale, H.G. Kerkhoff, D.W. Lindle, T.A. Ferrett, C.C. Bahr, W.D. Brewer, U. Becker, and D.A. Shirley, Phys. Rev. A 31, 2260 (1985).

1. T. Åberg, Phys. Rev. 156, 35 (1967).
2. K.G. Dyall and F.P. Larkins, J. Phys. B 15, 203 (1982) and references therein.
3. K.G. Dyall and F.P. Larkins, J. Phys. B 15, 219 (1982).
4. F. Wuilleumier and M.O. Krause, Phys. Rev. A 10, 242 (1974).
5. D.W. Lindle, T.A. Ferrett, U. Becker, P.H. Kobrin, C.M. Truesdale, H.G. Kerkhoff and D.A. Shirley, to be published; F. Wuilleumier, J. de Physique C2, 347 (1982) and references therein.
6. M.Y. Adam, P. Morin and G. Wendin, to be published.
7. A. Fahlman, M.O. Krause and T.A. Carlson, J. Phys. B 17, L217 (1984); A. Fahlman, M.O. Krause, T.A. Carlson and A. Svensson, Phys. Rev. A 30, 812 (1984).
8. M.G. White, R.A. Rosenberg, G. Gabor, E.D. Poliakoff, G. Thornton, S.H. Southworth and D.A. Shirley, Rev. Sci. Instr. 50, 1268 (1979).
9. S.H. Southworth, C.M. Truesdale, P.H. Kobrin, D.W. Lindle, W.D. Brewer and D.A. Shirley, J. Chem. Phys. 76, 143 (1982); S. Southworth, U. Becker, C.M. Truesdale, P.H. Kobrin, D.W. Lindle, S. Owaki, and D.A. Shirley, Phys. Rev. A 28, 261 (1983).
10. C.N. Yang, Phys. Rev. 74, 764 (1948).
11. F. Wuilleumier and M.O. Krause, J. Electron Spectrosc. Relat.

Phenom. 15, 15 (1979).

12. W. Perssen, Phys. Scr. 3, 133 (1971).

13. C.E. Moore, Atomic Energy Levels, NBS Circular 467 (U.S. GPO, Washington, D.C., 1949), Vol. 1.

14. S.T. Manson and A.F. Starace, Rev. Mod. Phys. 54, 389 (1982).

15. M.Y. Adam, private communication.

16. G.V. Marr and J.B. West, Atom. Data 18, 497 (1976).

17. H. Smid and J.E. Hansen, Phys. Rev. Lett. 52, 2138 (1984).

18. J. Stohr, R. Jaeger and J.J. Rehr, Phys. Rev. Lett. 51, 821 (1983).

19. T.D. Thomas, Phys. Rev. Lett. 52, 417 (1984).

20. While the function provided by Thomas does not go to zero at the satellite threshold, he suggests that the intensity should vanish because of the shrinking of phase space.

21. In Table V of Ref. 4, the columns labelled Peak 7(i) and Total provide normalizations which differ by 30 percent. Manfred Krause has suggested that the Peak 7(i) scaling should be correct.

22. J.E. Hansen and W. Perssen, Phys. Rev. A 30, 1565 (1984).

Table I. The neon valence satellite binding energies from the present work together with the assignments of Dyall and Larkins[3] and with the energies of Perssen[12] from emission spectroscopy. All the satellite final states include a $1s^2 2s^2 2p^4$ core.

| Peak | Binding Energy (eV) | Assignment | Optical Energy (eV) |
|---|---|---|---|
| 1 | 62.27(10) | $(^1D)5p\ ^2P^o$ | |
| | | $(^1D)4d\ ^2S$ | |
| 2 | 61.02(10) | $(^1D)4p\ ^2P^o$ | 60.96 |
| 3 | 59.56(7) | $(^3P)5p\ ^2P^o$ | 59.83 |
| | | $(^1D)3d\ ^2D$ | 59.54 |
| | | $(^1D)3d\ ^2S$ | 59.51 |
| | | $(^1D)3d\ ^2P$ | 59.46 |
| | | $(^1S)3p\ ^2P^o$ | 59.40 |
| 4 | 58.06(6) | $(^3P)4p\ ^2P^o$ | 58.01 |
| 6 | 56.41(5) | $(^3P)3d\ ^2P$ | 56.48 |
| | | $(^3P)3d\ ^2D$ | 56.33 |
| 7 | 55.85(4) | $(^1S)3s\ ^2S$ | 55.87 |
| | | $(^1D)3p\ ^2P^o$ | 55.80 |

Table I. Continued.

| Peak | Binding Energy (eV) | Assignment | Optical Energy (eV) |
|---|---|---|---|
| 10 | 53.10(4) | $(^3P)3p\ ^2P^o$ | 53.06 |
| 11 | 52.13(3) | $(^1D)3s\ ^2D$ | 52.12 |
| 2s | | | 48.48 |
| 2p | | | 21.57 |

Table II. The asymmetry parameter values and branching ratios with respect to the 2s main line. The error in the last digit is noted in parentheses.

| Peak | K.E. (eV) | Asymmetry Parameter (β) | Branching Ratio (%) | Peak | K.E. (eV) | Asymmetry Parameter (β) | Branching Ratio (%) |
|---|---|---|---|---|---|---|---|
| 3 | 3.3 | - | 11.9 (33) | 4 | 3.6 | -0.42 (10) | 4.5 ( 8) |
| | 4.4 | 0.41 (23) | 11.0 (16) | | 4.7 | -0.06 (21) | 3.2 ( 5) |
| | 7.1 | 0.55 ( 5) | 12.6 ( 8) | | 5.9 | 0.19 (15) | 3.4 ( 7) |
| | 10.7 | 0.56 (11) | 12.4 ( 3) | | 8.6 | 0.43 (22) | 3.4 ( 1) |
| | 12.8 | 0.52 ( 6) | 13.0 ( 4) | | 12.2 | 0.74 (42) | 3.1 ( 4) |
| | 15.8 | 0.55 (12) | 12.0 (18) | | 14.3 | 0.81 (15) | 3.3 ( 2) |
| | 20.9 | 0.52 ( 5) | 12.0 ( 3) | | 17.3 | 0.95 (24) | 3.2 ( 4) |
| | 25.9 | 0.44 (12) | 11.3 (12) | | 22.4 | 1.14 (39) | 3.4 ( 5) |
| | 31.0 | 0.86 ( 7) | 9.3 ( 6) | | 27.4 | 1.06 (37) | 2.9 ( 8) |
| | 36.1 | 0.57 (24) | 9.5 (15) | | 32.5 | 1.47 (27) | 2.6 ( 6) |
| | 40.1 | 0.76 (15) | 8.3 ( 7) | | 37.6 | 1.43 (44) | 3.1 ( 7) |
| | | | | | 41.6 | 0.91 (26) | 3.4 ( 4) |
| 6 | 4.7 | -0.04 ( 4) | 19.1 ( 6) | 10 | 3.2 | - | 12.7 (33) |
| + | 5.9 | 0.14 ( 7) | 20.5 (13) | | 4.0 | - | 11.0 ( 6) |
| 7 | 6.9 | 0.17 (11) | 20.2 ( 9) | | 6.0 | -0.20 ( 2) | 12.5 ( 5) |
| | 8.0 | 0.31 (10) | 22.2 (11) | | 7.2 | -0.01 (14) | 9.6 ( 3) |
| | 10.7 | 0.35 ( 7) | 22.9 ( 8) | | 8.8 | 0.13 (34) | 9.6 ( 9) |
| | 14.3 | 0.71 (14) | 22.6 (18) | | 9.7 | 0.17 ( 3) | 10.1 ( 3) |
| | 16.4 | 0.70 ( 4) | 23.9 ( 5) | | 10.9 | 0.17 ( 8) | 10.0 ( 4) |
| | 19.5 | 0.87 (20) | 23.7 (12) | | 13.6 | 0.35 (13) | 9.2 ( 5) |
| | 24.5 | 1.04 (11) | 24.7 ( 4) | | 17.2 | 0.68 (20) | 7.8 ( 2) |
| | 29.6 | 1.10 ( 9) | 24.2 ( 7) | | 19.3 | 0.68 ( 6) | 7.7 ( 2) |
| | 34.6 | 1.11 ( 8) | 24.4 ( 9) | | 22.3 | 0.70 ( 7) | 7.4 ( 5) |
| | 39.7 | 1.26 ( 7) | 23.7 ( 5) | | 27.4 | 0.81 (12) | 7.0 ( 5) |
| | 43.8 | 1.27 (10) | 23.3 ( 9) | | 32.5 | 0.76 (25) | 6.2 ( 6) |
| | | | | | 37.5 | 0.97 (29) | 5.5 ( 6) |
| | | | | | 42.6 | 1.23 (16) | 5.1 ( 3) |

Table II. Continued.

| Peak | K.E. (eV) | Asymmetry Parameter (β) | Ratio (%) |
|---|---|---|---|
| 11 | 3.3 | - | 13.1 (23) |
| | 4.1 | 1.24 (18) | 7.6 ( 7) |
| | 5.0 | 1.68 (25) | 7.0 (12) |
| | 7.0 | 0.51 ( 4) | 8.6 ( 3) |
| | 8.2 | 0.18 (15) | 7.1 (15) |
| | 9.7 | -0.01 (10) | 6.4 ( 3) |
| | 10.7 | -0.12 ( 5) | 6.8 ( 6) |
| | 11.9 | -0.22 ( 7) | 6.6 ( 2) |
| | 14.6 | -0.20 ( 6) | 6.2 ( 4) |
| | 18.2 | -0.27 ( 7) | 6.9 ( 6) |
| | 20.3 | - | 7.2 ( 2) |
| | 23.3 | -0.34 (13) | 6.6 ( 6) |
| | 28.4 | 0.16 (25) | 6.8 ( 5) |
| | 33.4 | 0.27 (13) | 6.1 ( 5) |
| | 38.5 | - | 5.2 (12) |

Table III. Relative satellite intensities as a ratio with the 2p line. The results of this work are compared with the higher energy measurement of Wuilleumier and Krause[4] and with the sudden limit calculation of Dyall and Larkins.[3]

| Satellite Peak No. | 10 eV Kinetic Energy | 40 eV Kinetic Energy | Experiment at 130-150 eV Photon Energy[a] | Calculation[b] |
|---|---|---|---|---|
| 3 | 0.81 | 0.85 | 0.54 | 0.41-0.61 |
| 4 | 0.20 | 0.33 | 0.49 | 0.36 |
| 6+7 | 1.34 | 2.33 | 2.55 | 1.13-1.24 |
| 10 | 0.52 | 0.51 | 0.68 | 0.28 |
| 11 | 0.32 | 0.48 | 0.35 | - |
| Sum | 3.19 | 4.50 | 4.61 | 2.18-2.49 |

[a] Wuilleumier and Krause's reported intensities for satellites 5, 8, 9, and 12 have been added to their neighbor satellite peak.

[b] The calculated contributions from $^2S$ states have been multiplied by the ratio $\sigma_{2s}/\sigma_{2p}$ at 55-150 eV photon energy.[10]

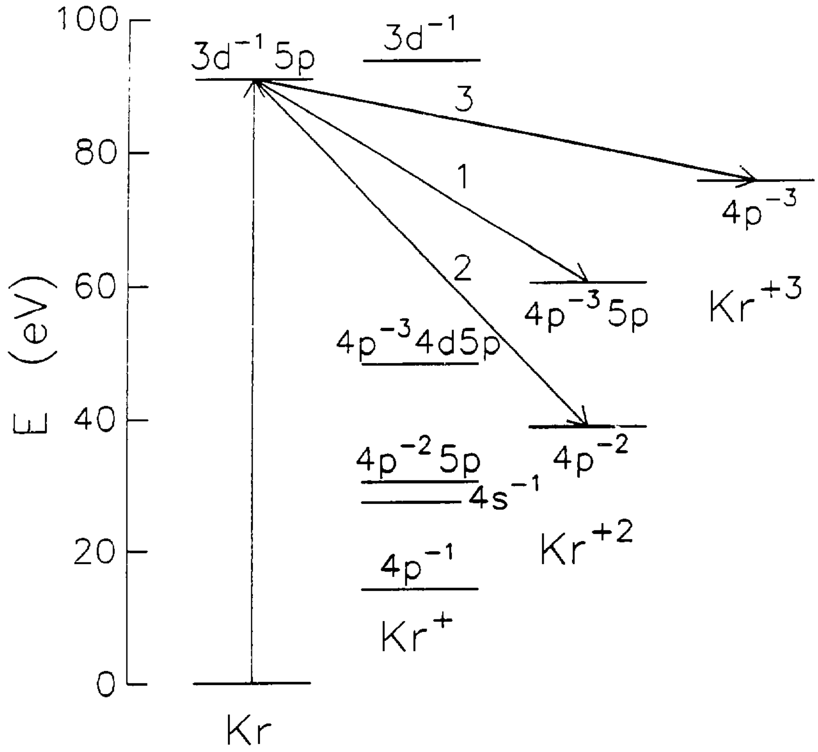

XBL 8611-4318

Figure 4

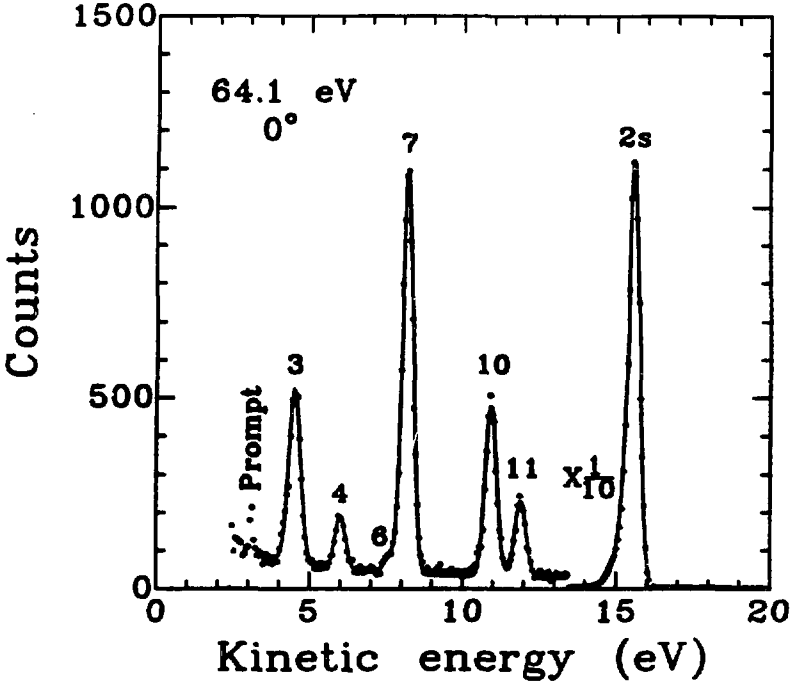

XBL 845-1986A

Figure 1

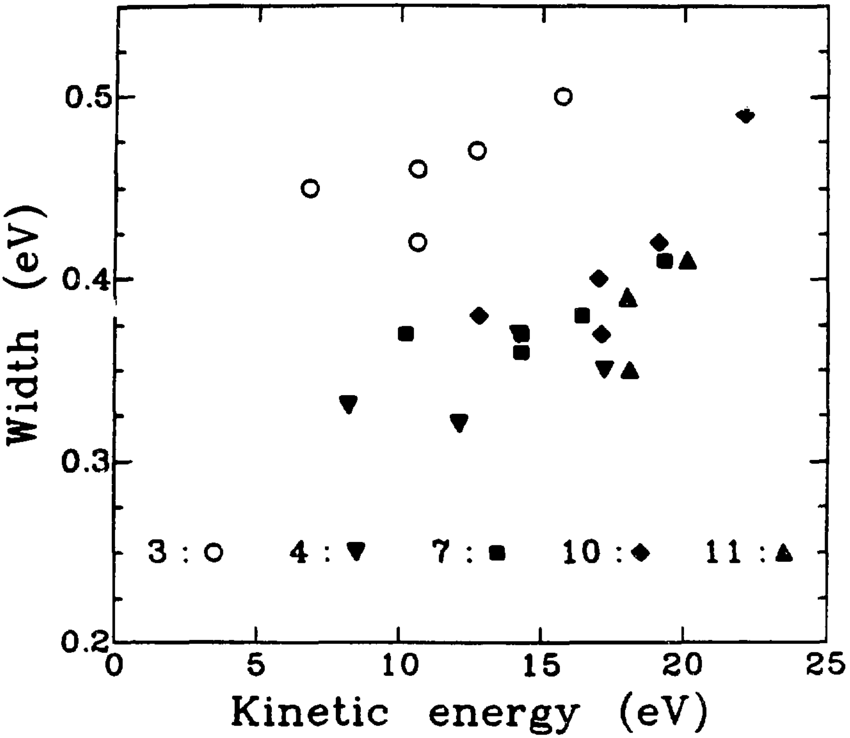

XBL 8410-4569

Figure 2

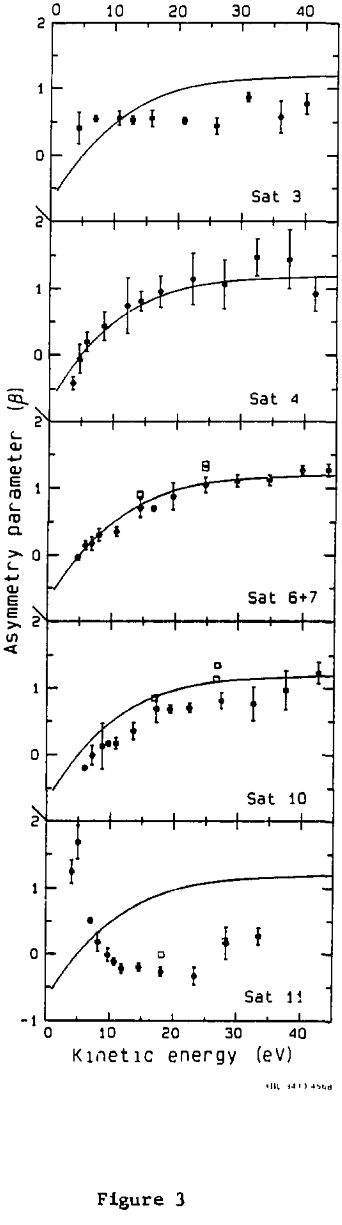
0
10
20
30
40
2
1
0
Sat 3
Sat 4
Sat 6+7
Sat 10
Sat 11
-1
Asymmetry parameter (β)
Kinetic energy (eV)
XBL 8410-4568

Figure 3

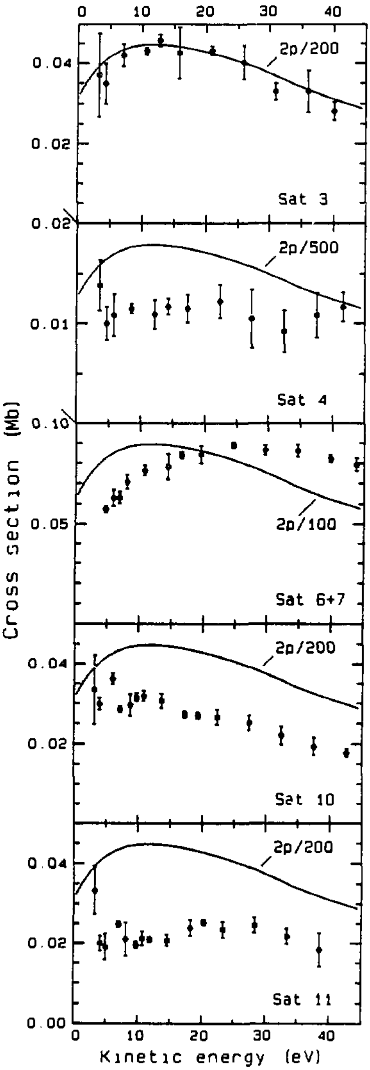
0
10
20
30
40
0.04
0.02
2p/200
Sat 3
0.02
2p/500
0.01
Sat 4
0.10
0.05
2p/100
Sat 6+7
0.04
0.02
2p/200
Sat 10
0.04
0.02
0.00
2p/200
Sat 11
Cross section (Mb)
Kinetic energy (eV)

Figure 4

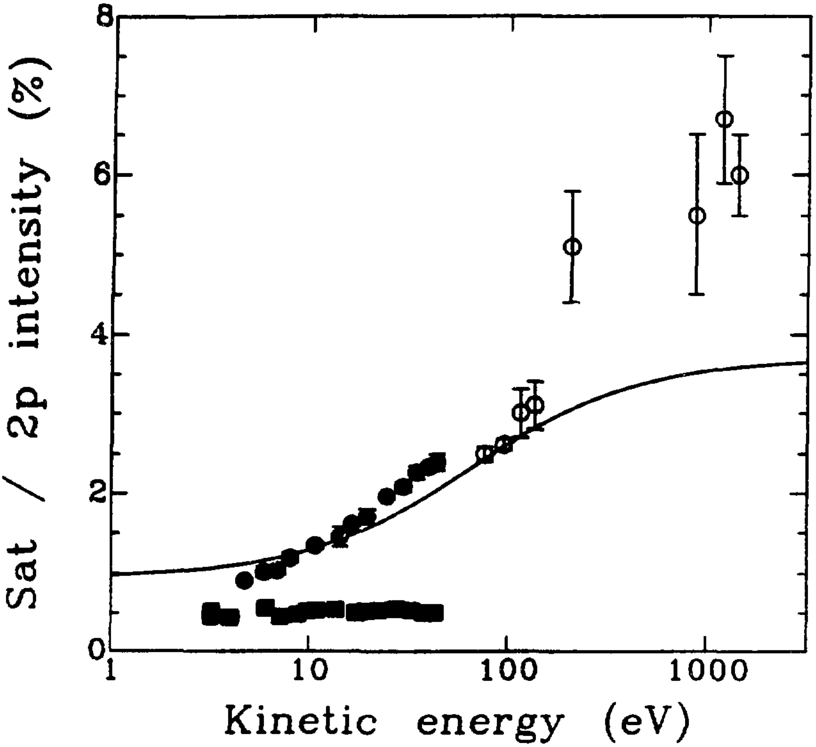

XBL 8410-4570

Figure 5

# IV. HELIUM AND NEON PHOTOELECTRON SATELLITES AT THRESHOLD*

## ABSTRACT

Photoionization of helium and neon to excited satellite states, $He^+$ nl and $Ne^+$ $1s^2 2s^2 2p^4 nl$, was studied with synchrotron radiation and threshold electron analysis. Photoelectron satellites have been directly measured at threshold for the first time. The relative satellite cross sections were determined over the kinetic energy range from 0 to 1 eV. The angular distributions were also evaluated close to threshold. Strong correlation effects were observed in two cases. For He near threshold, the angular-distribution asymmetry parameter $\beta$ is near zero for the $n=2$ satellite and is increasingly negative for the higher n satellites, in agreement with the theoretical prediction of Greene. In the threshold photoelectron spectrum of Ne, many final states are present, some with quartet spin multiplicity and others with high L values.

## A. INTRODUCTION

In photoelectron spectra strong "main-line" peaks are accompanied by weak satellite peaks. The satellite transitions lead to final ionic states that cannot be created simply by removing a single electron from the nominal ground-state configuration; e.g.,

$$\mathrm{He}\ (1s^2(^1S)) \rightarrow \mathrm{He}^+\ (2s,2p) + e^-,$$

$$\text{or Ne}\ (1s^2 2s^2 2p^6(^1S)) \rightarrow \mathrm{Ne}^+\ (1s^2 2s^2 2p^4(^1D)3p(^2P^o)) + e^-.$$

Two theoretical models which are used to describe satellite intensities are shake-up and configuration interaction (CI). According to the shake-up theory,[1] the more or less abrupt change in the atomic potential that accompanies the photoelectron's departure provides a perturbation which may "shake" one of the passive electrons into an excited orbital. In this heuristic picture, the probability of reaching an excited (satellite) final state in the ion depends on the time $\Delta t$ for the hole to be created; i.e., on the kinetic energy of the photoelectron. Two limits are hypothesized. At the satellite threshold, in the adiabatic limit, the passive electrons' orbitals can relax into their final state form during photoemission, accelerating the photoelectron. In this limit the satellite transition should have its minimal value. In the high photon energy, sudden limit, the satellite transition's intensity approaches a constant fraction of the main-line intensity. Thomas[2] has developed a model for the transition from the adiabatic to the sudden limit. In this model the sudden limit is already closely approached at a relatively low value of the satellite photoelectron's kinetic energy.

The configuration-interaction model employs a multiconfiguration description of the initial and final states to calculate the satellite cross sections $\sigma$. Because of their closed-shell initial states, CI calculations have been carried out for the valence satellites of the rare gases.[3] In the high photon-energy limit, the relative satellite intensities may be calculated from the CI mixing coefficients. For the "final-ionic state CI channel" in Ne 2p photoemission, for example, much of the intensity is derived from the admixture of the main configuration, $Ne^{+} |2p^{5}\ {}^{2}P^{o}\rangle$, in the final-state wavefunction. By using a basis of relaxed orbitals to describe the final-ionic state, the CI calculations include the shake-up contributions. To first approximation, the photon-energy dependence of the (satellite) / (main line) intensity ratio is determined by the energy variation of the dipole matrix element between the 2p and continuum orbitals.[4] At a given photon energy, $h\nu$, the satellite and main-line photoelectrons will have different kinetic energies. For the $np^{4}nd\ {}^{2}S$ satellites in Ar, Kr and Xe, Smid and Hansen[4] have predicted that the relative intensities will remain nearly constant with energy, decreasing slowly with increasing $h\nu$. However, these calculations are not expected to be accurate at low kinetic energies.

The predictions of the different theories for satellities far from the sudden limit are most rigorously tested by measuring satellites at threshold and low kinetic energies. In particular, one experiment has examined a satellite intensity through a wide range of kinetic energies down to threshold. Woodruff and Samson[5,6] used synchrotron radiation to ionize He and the fluorescent decay from the excited $He^{+}(n=2)$ levels to measure the n=2 satellite intensity down to threshold. In the low kinetic energy region, they observed that the satellite cross section varied slowly with energy except on autoionizing doubly-excited states, where dramatic asymmetric and window profiles were observed. Since the satellite intensity was not observed to decrease at low energies, their experiment suggests that the time dependent shake-up theory[2] is not an adequate description for He near threshold as might be expected for a two electron system. By having a strong electric field present or absent, Woodruff and Samson[6] were also able to deconvolute the n=2 fluorescence into the 2s and 2p contributions. Their results, as well as those from photoelectron angular distribution measurements,[7-9] show the 2s having a nearly constant (satellite) / (main line) intensity ratio, while the (2p) / (1s) branching ratio decreases with increasing kinetic energy over the measured 60 eV range. The energy-dependent behavior of $\sigma_{2s}$ and $\sigma_{2p}$ has been reproduced by close-coupling calculations.[10]

The fluorescent technique, however, is limited to the lowest-binding-energy satellite. A more general method is electron spectroscopy. Satellites in the Ar KLL Auger spectrum have been studied by Armen et al.[11] In qualitative agreement with the predictions of the time dependent shake-up theory, the core-level Auger satellite is weaker near threshold, increasing to a constant value at higher photon energies. Experiments on the valence photoelectron satellites of Ne,[12,13] Ar[14] and Xe[15] have revealed a variety of intensity vs. energy dependences: increasing, nearly constant and decreasing. Quite different $\sigma(h\nu)$ behavior has been seen for satellites whose main final-state configurations have the same excited orbital.[12,13] Shake-up and initial- and final-ionic-state CI alone are unable to explain the observed variety of $\sigma(h\nu)$ behavior. Mechanisms not included in these theories are autoionization from doubly-excited states, studied in He[5-8] and Ne,[13] and continuum-state CI, which has been observed in the He 2p energy dependence.[6-9] Autoionization into satellite channels and continuum-state CI have together been referred to as interchannel coupling.

These additional processes should be strongest at threshold. Unfortunately, electron spectrometers typically have increasing difficulties with background and transmission as the electron energy decreases below a few eV. However, one class - threshold electron analyzers - are specifically designed to study photoionization processes at threshold by using a small electric field for extracting slow electrons.[16-18] For 0 eV electrons this technique provides high sensitivity and high resolution. A threshold electron analyzer has been constructed which uses time-of-flight analysis, similar to the approach used by Baer et al.[16] Because of its longer flight distance, the resolution of our analyzer degrades more slowly with increasing kinetic energy, facilitating the measurement of satellite intensities at small kinetic energies. Combining the threshold electron analyzer with a rotatable chamber allows satellite angular distributions to be determined near threshold, as well. In this paper we report studies of correlation satellites in the photoelectron spectra of $He^+$ and $Ne^+$, determined near threshold by this spectometer. Experimental procedures are described in Section B. In Section C we report and discuss the cross sections and asymmetry parameters of the $He^+$ satellites. Neon satellite cross sections and asymmetry parameters are presented and discussed in Section D. Finally, Section E contains the conclusions.

## B. EXPERIMENTAL

Figure 1a shows the threshold electron analyzer, which is cylindrically symmetrical. In the interaction region, the synchrotron radiation beam crosses through an effusive gas jet. Electrons ejected from the gaseous atoms pass through three regions: the extraction region (10 mm long), the acceleration region (18 mm), and the drift region (262 mm). With the voltages plotted in Fig. 1b, zero-kinetic energy electrons have a flight time of 150 ns. Figure 2 shows a photoelectron spectrum of He with the photon energy 1 eV above the n=2 satellite threshold. Two peaks result from the n=2 satellite transition because of photoelectrons initially moving toward (shorter time) and away from (longer time) the detector.

The small electric field across the interaction region bends the trajectories of low kinetic energy electrons toward the detector. For very slow electrons, in our case 0 to 30 meV, all emission directions are accepted. The transmission function shown in figure 2 was calculated by considering a point source and the initial ejection angle for an electron to hit the edge of the detector. The transmission decreases steeply to an acceptance half-angle ($\delta$) of 10° at 1 eV. However, the 1 eV angular acceptance is still much larger than that of an angle resolved photoelectron analyzer. For example, the time-of-flight electron spectrometers of White et al.[19] have a collection half-angle $\delta$ of 3°.

A threshold time-of-flight analyzer, like a time-of-flight mass spectrometer, achieves high resolution by satisfying the space focussing condition.[20] As shown in Fig. 1b, an electron from the side of the interaction region further from the detector is accelerated more than one from the near side. With the proper choice of distances and voltages, both electrons arrive at the detector in the same flight time. One-dimensional calculations which consider a 5 mm wide interaction region show that the resulting time width can be < 1 ns for electrons with kinetic energies from 0 to 10 eV. Ray tracing for 0.1 and 1 eV electrons predicts that the time width from the different initial emission directions should also be < 1 ns. These calculations are confirmed by the observed full width at half maximum of 1.3 ns for the 1 eV peak in figure 2. The monochromator bandpass contributes significantly to this width.

We now describe some other aspects of the design. A moveable hypodermic needle serves as the gas inlet while preserving the uniformity of the electric field. The analyzer apertures are wide in order to accept electrons from a large interaction region. The first and smallest aperture has a diameter of 6 mm. The apertures are covered with Cu grids, 20 lines/inch. For the shielding of magnetic fields, there are 2 cylinders of mu metal around the analyzer and 1 cylinder at the vacuum chamber wall. The drift region and detector are differentially pumped by a 50 l/s turbo pump. The electron detector, consisting of a pair of microchannel plates and a conical anode, is identical to that of White et al.[19] To minimize unwanted secondary electrons, all surfaces seen by photoelectrons in flight are coated with graphite. In order to further reduce the background, an aperture is positioned upstream of the analyzer to prevent scattered light from hitting any analyzer surfaces.

The time-of-flight signal processing is done in the usual way[19] using a time-to-amplitude converter (TAC), which receives the electron pulse as "start" and the light pulse as "stop." Scans are done by varying the photon energy and having a multi-input scalar collect: (i) the counts falling into one or two time (kinetic energy) windows and (ii) the output from the photon flux monitor, a sodium salicylate scintillator. For normalization the electron counts are divided by the photon flux. Within a scan the electrons are all at a given kinetic energy. Therefore, in a scan the normalized intensities are proportional to the differential cross section $d\sigma/d\Omega\ (h\nu,\theta)$, with no analyzer transmission correction needed. The sample pressure was held constant by a variable leak valve. The ambient pressure of the chamber was about $3\times10^{-5}$ mbar during both the He and Ne experiments.

The experiments were performed at the 5.6m toroidal grating monochromator (TGM) at the Hamburger Synchrotronstrahlungslabor (HASYLAB). Some preliminary scans were carried out using a grazing incidence "Grasshopper" monochromator at the Stanford Synchrotron Radiation Laboratory (SSRL). For He a 1500 l/mm grating with no filter was used. For Ne a 750 l/mm grating was employed with a 1500 Å Al filter to reduce the contribution of higher order light. Residual higher order light produces a continuous background because the higher order components are above the threshold for double ionization. In addition, the measured light intensity must be corrected in order to represent the first order component alone. The typical resolution of the TGM monochromator was 0.1 eV for the 0 eV scans and 0.2 eV for the higher kinetic energy scans.

Fig. 3 shows a 0 eV scan with the He satellites n=2 through 8 clearly seen with smoothly decreasing intensity. At 65.4 eV photon energy, the combined analyzer and monochromator resolution is 0.15 eV, of which the monochromator contributes an estimated 0.08 eV. The n=8 satellite has a cross section of only 0.8 kb, which demonstrates the high sensitivity of the threshold technique. The higher satellites are seen as an unresolved step which ends at the $He^{+2}$ threshold. The 0 eV signal rises above the $He^{+2}$ threshold as the double ionization probability increases.

The peaks in a constant kinetic energy scan are not symmetric. For a 0 eV scan the low $h\nu$ side contains only the monochromator width, while the high $h\nu$ side is affected by both the monochromator and analyzer resolutions. As a result, the peaks were fitted using an asymmetric gaussian function, for which the left and right sides can have different widths.

The satellite cross sections were calculated from intensity ratios relative to the n=2 satellite for He and to the 2s main line for Ne. The He n=2 satellite cross section has been measured by Woodruff and Samson[5] to be 0.10(1) Mb from 0 to 1 eV kinetic energy. For Ne, $\sigma_{2s}$ has only been determined down to 2.5 eV.[21] This lowest kinetic energy value $\sigma_{2s}$ = 0.21(4) Mb (assumed to include satellite 13) was extrapolated linearly to $\sigma_{2s} = 0.17$ Mb at 0 eV. The reported errors for the cross sections represent the uncertainties of the fits, increased if two scans do not agree within errors. These error estimates are as large as, or larger than, the statistical uncertainty.

The analyzer was mounted in a chamber which could be rotated about the photon beam.[22] In order to determine the angular distribution asymmetry parameter $\beta$, we carried out 0.5 and 1 eV scans at three angles, $\theta = 0°$, 48° or 55°, 90°. Here, $\theta$ is the angle between the photon polarization direction and the electron emission direction. In the dipole approximation with a randomly oriented sample, the angular distribution of photoelectrons follows the equation given by Yang,[23]

$$\frac{d\sigma(\theta,h\nu)}{d\Omega} = \frac{\sigma}{4\pi}\,[1+\beta(h\nu)P_2(\cos\theta)], \qquad (1)$$

where $P_2$ is the second Legendre polynomial. In analyzing the angular distribution results, two sizable corrections must be considered. First, the incomplete linear polarization of the light must be included. Secondly, the large acceptance angle ($\delta$) of the analyzer must be considered. The resulting equation for the photoelectron angular distribution is:

$$\frac{1}{\sigma}\int d\sigma =$$

$$\frac{1}{4}\,[2-2\cos\delta + \frac{1}{4}\,(1-P_1)\beta\cos\delta\sin^2\delta + P_1\,\beta\cos\delta\sin^2\delta\,P_2(\cos\theta-\lambda)]. \qquad (2)$$

The first two terms represent the angle-independent part, which becomes monotonically larger as $\delta$ increases. The last two terms come from the angle-dependent portion of Eq. (1).

The polarization calibration was performed by taking photoelectron spectra of Ne at several angles and by using the known β-values of the 2s and 2p lines. The measured values for the He experiment (60 - 80 eV photon energy) were $P_1 = 0.89(2)$, $\lambda = -7(2)°$ and for the Ne experiment (50 - 60 eV) $P_1 = 0.73(3)$, $\lambda = -10(1)°$, where $P_1$ is the first Stokes parameter $(I_{||} - I_{\perp}) / (I_{||} + I_{\perp})$ and λ the angle between the major axis of the polarization ellipse and the horizontal plane of the DORIS storage ring. Measuring the intensity ratio of He (n=2) at low kinetic energy and He 1s at high kinetic energy while assuming the calculated δ at high energy gives the following results: δ=15° at 0.5 eV and δ=11° at 1 eV. These δ values, which represent average acceptance angles over the source volume, are quite similar to those calculated for a point source at 0.5 and 1.0 eV. The analyzer sensitivity was very angle-dependent in part because of the crescent-shaped photon beam spot, 5 mm broad. As a result, the sensitivity to θ had to be calibrated against a transition of known β.

## C. HELIUM

The cross sections and asymmetry parameters will be discussed separately below.

### 1. HELIUM CROSS SECTIONS (σ)

Table I shows the observed He satellite binding energies together with the calculated energies of a singly charged H-like ion. Each satellite contains an unresolved summation of the possible values of the orbital angular momentum l. Table I displays in its last column the observed $\sigma$ values at 0 eV. At threshold the satellite $\sigma$ values decrease approximately as the mean separation of energy levels adjacent to $E_n$, $\Delta E(n) = 8I_H n / (n^2 - 1)^2$, with $I_H$ being the ionization potential of H. Fano and Cooper[25] state that for a given Rydberg series, the excited orbitals are nearly identical at small r except for a normalization factor, for which they use the energy spacing. Qualitatively, the variation of the satellite $\sigma$ values with n reflects the expansion of the Rydberg orbitals.

The satellite $\sigma$ values from 0 to 1 eV above threshold are shown in Fig. 4. The $\sigma$ values in both the table and the figure have been corrected for the contribution of higher-order light, which decreases nearly linearly from 31 % at 65 eV to 12 % at 80 eV photon energy. There are no calculated $\sigma$ values available for comparison. A recent photoelectron measurement at higher kinetic energies[26] shows $\sigma_{n=3}$ and $\sigma_{n=4}$ having lower values than at threshold, with the intensities decreasing faster than the 1s main line. The satellites as a whole show relatively constant behavior over the kinetic energy range from 0 to 1 eV. Continuum state CI has been shown both theoretically[10] and experimentally[6-9] to strengthen the 2p satellite as the kinetic energy decreases. It should affect the higher n satellites in a similar manner. However, the intensity variations caused by continuum state CI, as observed for He 2p, occur over wide ranges of kinetic energy. The resulting intensity change from 0 to 1 eV should be quite small. The changes in intensity which are observed probably result from autoionization from doubly excited states. A number of autoionizing resonances $K_n$ have been reported:[6] $2_4$ at 73.66 eV, $0_4$ (74.15 eV),

$3_5$ (75.54 eV), $3_6$ (76.10 eV), and $3_7$ (76.30 eV), all of which could contribute to variations in Fig. 4. A more detailed study is required to determine the effect of individual resonances on each satellite.

## B. HELIUM ASYMMETRY PARAMETERS (β)

Figure 5 shows the asymmetry parameters of the He satellites n=2-6 measured at kinetic energies near 0.5 and 1.0 eV. The relative analyzer efficiency E(θ) was calibrated by using known β-values for one transition. For 0° E was alternatively inferred from $\beta_{1s} = 2$ and from $\beta_{n=2} = -0.10(12)$.[7] E(55°) was set arbitrarily to 1, while $\beta_{n=2}$ was again used to evaluate E(90°). The error bars for β include both statistical errors and systematic errors from the efficiency calibration, estimated to be 0.1. The $\beta_{n=2}$ values reported result from the $\beta_{1s}$ calibration and agree with the earlier measurements.[7-9] Lindle et al.[26] determined β for the satellites n = 3,4 and 5 at some higher kinetic energies. Their lowest kinetic energy β values, at 3-4 eV, agree with the present results, while at higher energies $\beta_{n=3}$ and $\beta_{n=4}$ are observed to increase.

Greene[27] has calculated the near-threshold asymmetry parameters for He. His theoretical approach starts from Herrick's[28] |KT> basis, developed for doubly excited states. In this basis the dipole operator $r_1 \cos\theta_{12}/r_2^2$ is approximately diagonal. Here $r_1$ is the radial distance of the bound electron, $r_2$ the radial distance of the photoelectron and $\theta_{12}$ the angle between $\hat{r}_1$ and $\hat{r}_2$. Larger values of K and T correspond to more correlated angular motion of the two electrons, which tends to keep them on opposite sides of the nucleus. For both near-threshold satellites and doubly-excited states, the dipole operator has dominant importance for the angular wavefunctions. In both these cases angular correlations are influential. For He with a $^1P^o$ final state, the T = 1 channel is the lowest energy channel at high $r_2$. For He with T = 1, the preferential photoelectron direction is parallel or anti-parallel to $\underline{L} = \underline{j}_\gamma$, and $\beta \sim -1$, where $\underline{L}$ is the total orbital angular momentum and $\underline{j}_\gamma$ is the angular momentum of the photon. The results calculated by Greene are displayed in Fig. 5 as open squares, connected by a solid line for clarity. Both the experiment and theory show β decreasing with increasing n. The generally good agreement between experiment and theory implies that the factors affecting β are reasonably well understood and are included in Greene's theory. This is the major result of the comparison. The decreasing trend in β also confirms the expectation that the K, T classification becomes more exact as n increases. The agreement between the experiment and the calculation of Greene also improves with increasing n. Finally, Greene only claimed accuracy for his calculation for photoelectron energies between 0 and a fraction of an eV. However, the small change in β from 0.6 to 1.1 eV, as well as the agreement with the measured β values at 3-4 eV,[26] suggests that the theory and the angular correlations which it describes may in fact apply to a wider kinetic energy range than expected.

An alternative basis set for the He final state is $|nl_1l_2;L\pi\rangle$, where n and $l_1$ refer to the bound electron and $l_2$ to the photoelectron. In this description each satellite n has a set of $l_1$ unresolved components, with $\beta_n$ determined by,

$$\beta_n = \sum_{l_1} \sigma_{l_1}\beta_{l_1} \Big/ \sum_{l_1} \sigma_{l_1} . \qquad (3)$$

The extraction field was much too weak to produce significant $l_1$ mixing. For the n=2 He satellite where $l_1$ may be s or p, Jacobs and Burke[10] and Chang[29] have calculated $\beta_{2p}$ which decreases with decreasing kinetic energy until $\beta_{2p} = -0.85$ at 1.3 eV (from Jacobs and Burke). All $\beta_{ns}$ must be 2. From $\beta_{2s}$ and $\beta_{2p}$ along with our experimental $\beta_{n=2}$, one infers $\sigma_{2p} / \sigma_{2s} = 2.7(5)$ at 0.6 eV and 2.3(4) at 1.1 eV. Like $\beta_{n=2}$, these ratios agree with earlier measurements.[6,8] For the higher n satellites larger $l_1$ and $l_2$ can contribute. Since only $\beta_{ns}$ is known _a priori_, and only $\beta_{2p}$ is available from calculations, the different $l_1$ components are undetermined for n > 2. However, the observed negative β values imply that the ns states cannot be dominant constituents in the n > 2 satellites. Fig. 6a shows Greene's[30] threshold predictions for the fractional contribution of the different $l_1$ values in a given n satellite peak. As n increases the distribution over $l_1$ shifts toward higher $l_1$. We shall return to Fig. 6b at the end of Section IV.

## D. NEON

### 1. NEON CROSS SECTIONS (σ)

Figure 7 shows the 0 eV scan of the $Ne^+$ (2s) and $Ne^+$ $(1s^2 2s^2 2p^4 nl)$ satellites. At 48.5 eV, the combined analyzer and monochromator resolution is 0.14 eV, of which the monochromator contributes an estimated 0.11 eV. Table II contains assignments of the observed peaks using the optical energies of Persson.[32] The table also includes peaks observed at higher photon energy than shown in Fig. 7. This rather long list is not meant to be complete, but instead includes the states which are necessary to obtain a good fit. Additional states could contribute, for example, $(^1S)3s\ ^2S$ at 55.87 eV and $(^1D)3d\ ^2S$ (59.51 eV). Above 59 eV, as the energy approaches the double ionization thresholds, the assignments become more uncertain because the density of final states increases greatly. Both the d and f Rydberg orbitals have small quantum defects because of large centrifugal barriers. The energy spacing between nd and nf states is therfore quite small. As a result, the satellite peaks assigned to 4d and 5d states in Table II probably contain nf contributions.

The spectral scan in Fig. 7 contains many more peaks and its assignment many more final states than have been previously observed in Ne spectra.[12,13,31] Term symbols of high orbital angular momentum, e.g. $^2F^o$, are present. The ionic term symbols populated in the shake-up and final-ionic state CI models, $^2P^o$ and $^2S$, are in the minority. Several quartet states are observed contrary to the spin selection rule $\Delta S = 0$. The satellite spectrum, at least at threshold, is seen to be very complex. The additional final states may or may not contribute to the satellite spectrum at higher hν. Comparison with photoelectron spectra[12] is inconclusive because of their lower resolution of 0.4 eV and higher background.

An analogy with double ionization suggests that the satellite spectrum at threshold might be different from that observed at higher energies. Fano[33] has predicted the excitation of high orbital angular momentum states near the double photoionization threshold (below and above). With two electrons moving slowly from the ion core, the angular correlation predicted by the Wannier theory[34] restricts the electrons to two narrow cones in opposite directions. The narrow spatial angles imply that the electrons may attain high values of l. For satellites at threshold, the situation is similar, the photoelectron and excited electrons are travelling away from the nucleus with small kinetic energy. The satellite may be thought of as a failed double ionization where one electron falls behind the other and is captured. In an analogous way, the spectator decay of an inner-shell resonance has been considered as an extreme case of post-collision interaction.[35] The observed quartet and high L satellite states in Ne may result from the strong coupling between the excited electron and photoelectron. The orientation of the core's spin and orbital angular momentum exerts a weakened influence on the excited electron. However, certain term symbols for the complete ion are still favored such as $^2P^o$ and $^2D$.

Autoionization from doubly-excited states could explain an additional satellite being present at threshold. As seen by Woodruff and Samson[5,6] in He and Becker et al.[13] in Ne, this mechanism is especially important at low kinetic energies because there exists a series of doubly-excited levels below each satellite threshold. The measurements in Ne showed in particular that satellite 12 ($^3$P)3s $^2$P has vanishing intensity except on doubly-excited resonances. The influential doubly-excited states have either the same core term symbol ($^3$P) or the same excited orbital (3s) as satellite 12. The absorption experiment of Codling et al.[36] places resonances: ($^3$P)3p($^2$P)4d at 52.112 eV, ($^3$P)3p($^2$P)5d (52.478 eV), ($^1$S)3s($^2$S)3p (52.614 eV) and ($^1$S)3d($^2$D)3p (57.574 eV). These resonances coincide with the thresholds of satellites 11, 11a and 5, suggesting that satellites 11a and 5 may exist only on these resonances because of the autoionization decay. Satellite 11 is clearly observed at higher photon energies.[12,13,31] The complexity of the threshold spectrum may result from the correlation between the excited electron and photoelectron in two ways: nonresonantly because both electrons are slow and resonantly from the decay of doubly-excited states.

The last column of Table II presents the satellite cross sections inferred from the (satellite) / (2s) branching ratio values derived from the threshold scan. Figure 8 shows the satellite $\sigma$ from a series of constant kinetic energy scans from 0 to 1 eV taken at 48°, near the pseudo-magic angle. For the Ne scans, the counts were first normalized to the electron current in the storage ring and then divided by a separate scan of I(h$\nu$) / (ring current). This procedure was necessary because of instabilities in the photomultiplier tube used to monitor the photon flux. The uncertainty of this normalization is estimated to be $\lesssim$ 5%. The light intensity is corrected for higher order components, whose contribution varied between 8 and 23 %. Figure 8 also contains the $\sigma$ values at higher kinetic energies from Heimann et al.[12] and Becker et al.[13] In Fig. 8 and table II the error bars include the uncertainty from both the normalization and the higher order correction.

The Ne satellite intensities will be discussed in two parts. First, the cross sections at threshold will be considered, then the variation of $\sigma$ with kinetic energy. The general discussion of Fano[33] and the He calculation of Greene[30] (shown in Fig. 6a) predict how the excited electron goes into the different l orbitals at threshold. The distribution over l should change as n increases, shifting to higher l.

Figure 6b shows the observed distribution for the neon valence satellites. The np states, which are heavily favored in the shake-up picture, are strong but not dominant. For satellite final states with n = 3, the s and p orbitals receive nearly equal fractions while d orbitals are more infrequent. When the excited electron goes to the n = 4 or n = 5 shell, the fraction of s orbitals is small while larger, similar portions are observed in p and d (or f) orbitals. Qualitatively, the Ne satellites at threshold show the expected behavior of favoring higher l as n increases.

It is interesting to consider the distribution among the core term symbols at threshold: the $^3P$ : $^1D$ : $^1S$ intensities vary as $^3P : {}^1D : {}^1S = 9 : 8 : 0.3$. The difference between the measured values and the statistical ratios results in part from the enhancement of the $^1D$ satellite 11 on a resonance and from the location of the $^1S$ states at high binding energies, where some satellite peaks could not be assigned. The result at threshold contrasts with the observation at 130 - 150 eV photon energy of Wuilleumier and Krause, $^3P : {}^1D : {}^1S = 9 : (17\text{-}22) : \leq 6$.[31] Their measured values may be affected by unresolved contributions in their spectra.

In the kinetic energy range from 0 to 1 eV, the intensities of satellite 11 and 12 undergo large changes. As discussed above, doubly-excited states may autoionize into satellite channels enhancing the satellite intensity. In a constant kinetic energy scan, a resonantly enhanced peak shows a number of characteristic features, seen for example in satellite 11 at threshold. The width of this peak in the 0 eV scan is 0.12 eV, less than the experimental resolution. Similarly, the hν position of satellite 11 is not quite right for its binding energy. If the monochromator width is decreased to 0.09, then the branching ratio of satellite 11 relative to the 2s intensity is increased by 17(6)%.

For satellite 11 the enhancement at threshold by a factor of 3 is caused by the resonance $(^3P)3p(^2P)4d$, which shares neither core term symbol nor excited orbital with the satellite. In contrast, a doubly-excited state with a 3s orbital, $(^1S)3s(^2S)3p$, gives little intensity to this satellite channel. This resonance instead strongly enhances satellite 12,[13] whose final state also has a 3s orbital. At 0.7 eV kinetic energy, Becker et al.[13] measured a satellite 11 intensity of 0.026(2) Mb, which is somewhat larger than the present σ result.

Satellite 12 decreases by a factor of 3 from 0 to 0.5 eV kinetic energy. No doubly-excited state has been observed[36] near the satellite 12 threshold, which suggests a continuum-state CI effect. As discussed above, the intensity of the He (2p) satellite decreases with increasing kinetic energy because of continuum state CI. However, the energy range over which satellite 12 diminishes is very much smaller than the range for He (2p). At 1.0 eV satellite 12 is seen to be increasing again because it approaches the $(^1D)3s(^2D)4p$ resonance at 50.565 eV. The mean of this line is shifted by 0.24 eV because the autoionizing electrons are at the uppermost edge of the analyzer kinetic energy window. On the high hν side of this resonance, Becker et al.[13] observed the satellite 12 intensity to be enhanced.

The satellites other than 11 and 12 are little affected by the presence of resonances. One would expect, for example, that satellite

10 would be enhanced dramatically at 0.6 eV on the $(^1D)3p(^2P)4s$ resonance. Curiously, this resonance appears to have little effect on the other satellite channels, either.[13] There seems to be something special about satellites 11 and 12, which make them more likely to be resonantly enhanced. Codling et al.[36] observe the doubly-excited resonances becoming weaker with increasing photon energy. Hence, most of the strong resonances are located below the thresholds of the higher satellites, and as a result coupling to satellites 11 and 12 is favored. To understand in general which doubly-excited states decay into which satellite channels requires further work. At present, a weak rule might state that when a doubly-excited state shares the excited orbital or core term symbol with one or more open satellite channels, the resonance will usually couple to one of the satellite channels.

The satellites as a whole appear to become somewhat less intense at 0.5 - 0.7 eV. This variation could result from the multiplication by $\sigma_{2s}$ if the 2s intensity does not change linearly as assumed. Comparing the 2s intensity from 1.5 to 0.1 eV with the calculated analyzer transmission confirms that $\sigma_{2s}$ is slowly varying and that it is enhanced by 10 - 20 % between 0.4 and 0.7 eV. The origin of the increase is probably autoionization from doubly-excited states such as $(^1D)3s(^2D)3p$ at 48.91 eV and $(^3P)3s(^2P_{3/2})7p$ at 48.98 eV. The apparent overall drop in the satellite intensities at 0.5 - 0.7 eV is most likely an artifact resulting from this uncertainty in $\sigma_{2s}$.

In comparison with higher kinetic energies, the intensities at threshold are either similar (satellites 7, 10) or higher (3, 4, 11, 12). This result suggests that the adiabatic limit does not exist. A recent calculation for Ne 2p → 3p shake-up[37] predicts that the satellite intensity at threshold is closer to the sudden limit than to the adiabatic limit. Classically, the velocity of the photoelectron as it passes through the valence orbitals is not low even at threshold. From an alternative point of view, the oscillator strength will be a continuous function from the doubly-excited Rydberg series across the corresponding satellite threshold.[14] Over the total, measured kinetic energy range, the He and Ne satellite intensities (except for the Ne satellite 7) are not observed to decrease as threshold is approached, contrary to the expectations of the shake-up model.[2]

## 2. NEON ASYMMETRY PARAMETERS (β)

Table III shows the Ne β values measured at 0.5 and 1.0 eV kinetic energies. The asymmetry parameters were calculated from intensities at 0° and 48° with the analyzer efficiency calibrated with the Ne 2s main line. The error bars include systematic errors from the calibration. While the uncertainties are large, some qualitative observations can be made. Satellite 12 is seen to have $\beta = -1$ within error. For satellite 12 there is only one possible photoelectron wave with $l=1$. According to angular momentum transfer theory,[39] this transition is parity unfavored and must have a constant $\beta = -1$. The only dramatic β variation occurs for satellite 11. While the low β value at 0.5 eV might result from the $(^1S)3s(^2S)3p$ resonance at 52.614 eV,[36] no corresponding effect is observed in the σ of figure 8. Near threshold, satellites 7 and 10 have β like the 2p main line, which has been observed at higher kinetic energies[12] and is expected because of their $^2P^o$ final state. Lastly, for satellite 3 the nearly constant $\beta$ at higher kinetic energies[12] continues close to threshold.

The satellites of both He and Ne have small or negative $\beta$ values near threshold. In the case of Ne, one must hesitate to infer an angular correlation between the excited and ejected electrons because the main line $\beta_{2p}$ is also negative. The Ne $\beta$ results show one satellite to originate from a parity unfavored transition. For two $^2P^o$ satellites (7, 10) $\beta$ is similar to $\beta_{2p}$ near threshold as well as at higher kinetic energies.

## E. CONCLUSION

We have directly measured for the first time threshold intensities of photoelectron satellite lines. In He correlation satellites up to n=8 were observed. The angular distribution asymmetry parameter $\beta$ of these satellites becomes increasingly negative with higher principal quantum number n of the excited electron. This result agrees with the predictions of a theoretical treatment of the long-range dipole interaction. In Ne the threshold spectrum contains lines with high spin and orbital momentum and is more complex than the spectra obtained at higher photon energies. The qualitative prediction of an approach toward the adiabatic limit with satellite intensities decreasing toward threshold is not seen (except for the Ne satellite 7). Near threshold the He 1s and Ne 2p satellite intensities vary slowly except at resonances, where some satellites show rapid enhancement. Further theoretical and experimental work toward understanding the selective decay of doubly-excited states into satellite channels will be valuable.

## REFERENCES

*Work done in collaboration with U. Becker, H.G. Kerkhoff, B. Langer, D. Szostak, R. Wehlitz, D.W. Lindle, T.A. Ferrett, and D.A. Shirley (Phys. Rev. A 34, 3782 (1986) to be published).

1. T. Åberg, Phys. Rev. 156, 35 (1967).
2. T.D. Thomas, Phys. Rev. Lett. 52, 417 (1984).
3. K.G. Dyall and F.P. Larkins, J. Phys. B 15, 219 (1982).
4. H. Smid and J.E. Hansen, Phys. Rev. Lett. 52, 2138 (1984).
5. P.R. Woodruff and J.A.R. Samson, Phys. Rev. Lett. 45, 110 (1980).
6. P.R. Woodruff and J.A.R. Samson, Phys. Rev. A 25, 848 (1982).
7. P. Morin, M.Y. Adam, I. Nenner, J. Delwiche, M.J. Hubin-Franskin, and P. Lablanquie, Nucl. Instr. and Meth. 208, 761 (1983).
8. D.W. Lindle, T.A. Ferrett, U. Becker, P.H. Kobrin, C.M. Truesdale, H.G. Kerkhoff, and D.A. Shirley, Phys. Rev. A 31, 714 (1985), and references therein.
9. V. Schmidt, H. Derenbach, and R. Malutzki, J. Phys. B 15, L523 (1982).
10. V.L. Jacobs and P.G. Burke, J. Phys. B 5, L67 (1972); K.A. Berrington, P.G. Burke, W.C. Fon, and K.T. Taylor, J. Phys. B 15, L603 (1982); P. Scott and P.G. Burke, J. Phys. B 17, 1321 (1984).
11. G.B. Armen, T. Åberg, K.R. Karim, J.C. Levin, B. Crasemann, G.S. Brown, M.H. Chen, and G.E. Ice, Phys. Rev. Lett. 54, 182 (1985).
12. P.A. Heimann, C.M. Truesdale, H.G. Kerkhoff, D.W. Lindle, T.A. Ferrett, C.C. Bahr, W.D. Brewer, U. Becker, and D.A. Shirley, Phys. Rev. A 31, 2250 (1985).

13. U. Becker, R. Hölzel, H.G. Kerkhoff, B. Langer, D. Szostak, and R. Wehlitz, Phys. Rev. Lett. 56, 1120 (1986).

14. M.Y. Adam, P. Morin, and G. Wendin, Phys. Rev. A 31, 1426 (1985).

15. A. Fahlman, M.O. Krause, and T.A. Carlson, J. Phys. B 17, L217 (1984); A. Fahlman, M.O. Krause, T.A. Carlson and A. Svensson, Phys. Rev. A 30, 812 (1984).

16. T. Baer, P.M. Guyon, I. Nenner, A. Tabche-Fouhaille, R. Botter, L.F.A. Ferreira, and T.R. Govers, J. Chem. Phys. 70, 1585 (1979).

17. R. Stockbauer, Int. J. Mass Spectrom. Ion Phys. 25, 89 (1977).

18. S. Cvejanovic and F.H. Read, J. Phys. B 7, 1841 (1974).

19. M.G. White, R.A. Rosenberg, G. Gabor, E.D. Poliakoff, G. Thorton, S.H. Southworth, and D.A. Shirley, Rev. Sci. Instrum. 50, 1268 (1979).

20. W.C. Wiley and I.H. McLaren, Rev. Sci. Instrum. 26, 1150 (1955).

21. F. Wuilleumier and M.O. Krause, J. Electron Spectrosc. Relat. Phenom. 15, 15 (1979); J.A.R. Samson and J.L. Gardner Phys. Rev. Lett. 33, 671 (1974).

22. U. Becker, R. Hölzel, H.G. Kerkhoff, B. Langer, D. Szostak, and R. Wehlitz, to be published.

23. C.N. Yang, Phys. Rev. 74, 764 (1948).

24. G.V. Marr and J.B. West, At. Data Nucl. Data Tables 18, 497 (1976).

25. U. Fano and J.W. Cooper, Phys. Rev. 137, A1364 (1965).

26. D.W. Lindle, P.A. Heimann, T.A. Ferrett, and D.A. Shirley, to be published.

27. C. Greene, Phys. Rev. Lett. 44, 869 (1980).

28. D.R. Herrick, Phys. Rev. A 12, 413 (1975); O. Sinanoglu and D.R. Herrick, J. Chem. Phys. 62, 886 (1975).

29. J.M. Bizau, F. Wuilleumier, P. Dhez, D.L. Ederer, T.N. Chang, S. Krummacher, and V. Schmidt, Phys. Rev. Lett. 48, 588 (1982).

30. C. Greene (private communication)

31. F. Wuilleumier and M.O. Krause, Phys. Rev. A 10, 242 (1974).

32. W. Persson, Phys. Scr. 3, 133 (1971).

33. U. Fano, J. Phys. B 7, L401 (1974).

34. G.H. Wannier, Phys. Rev. 90, 817 (1953).

35. G.B. Armen, T. Åberg, J.C. Levin, B. Crasemann, M.H. Chen, G.E. Ice, and G.S. Brown, Phys. Rev. Lett. 54, 1142 (1985).

36. K. Codling, R.P. Madden, and D.L. Ederer, Phys. Rev. 155, 26 (1967).

37. T.D. Thomas, J. Electron Spectrosc. Relat. Phenom. 40, 259 (1986).

38. S.H. Southworth, A.C. Parr, J.E. Hardis, J.L. Dehmer, and D.M.P. Holland, Nucl. Instrum. and Meth. A246, 782 (1986).

39. D. Dill and U. Fano, Phys. Rev. Lett. 29, 1203 (1972).

Table I. The He satellite binding energies and threshold cross sections.

| Peak | Binding Energy (eV) | Calculated Energy (eV)[a] | $\sigma$ (Mb) |
|---|---|---|---|
| 1s | | 24.567 | 7.6(2)[b] |
| n=2 | 65.44 | 65.377 | 0.10(1)[c] |
| n=3 | 72.95 | 72.934 | 0.0159(5) |
| n=4 | 75.57 | 75.579 | 0.0080(2) |
| n=5 | 76.80 | 76.803 | 0.0022(1) |
| n=6 | 77.46 | 77.469 | 0.0015(1) |
| n=7 | 77.86 | 77.870 | 0.00091(7) |
| n=8 | 78.12 | 78.130 | 0.00077(7) |
| n=9 | 78.30 | 78.308 | 0.00043(7) |
| n=10 | 78.46 | 78.436 | 0.00037(6) |
| Sat. total | | | 0.13 |

[a] from $E_n = E_\infty - I_H (Z^2/n^2)$, where $I_H$ is the ionization energy for H.

[b] Ref. 24

[c] Ref. 5

Table II. Neon valence satellite binding energies from the present work together with the energies of Persson[32] from emission spectroscopy. All the assigned satellite final states include a $1s^2 2s^2 2p^4$ core. The last column contains the satellite cross sections at threshold measured by us.

| | Binding | | Optical | |
|---|---|---|---|---|
| Peak | Energy (eV) | Assignment | Energy (eV) | $\sigma$ (Mb) |
| 2p | | | 21.57 | 6.2(2)[a] |
| 2s | | | 48.48 | 0.16[b] |
| 13 | 48.77 | $(^3P)3s\ ^4P$ | 48.77 | 0.013(3) |
| 12 | 49.36 | $(^3P)3s\ ^2P$ | 49.37 | 0.019(3) |
| 11 | 52.07 | $(^1D)3s\ ^2D$ | 52.11 | 0.063(7) |
| 11a | 52.43 | $(^3P)3p\ ^4D^o$ | 52.49 | 0.007(2) |
| 10a | 52.72 | $(^3P)3p\ ^2D^o$ | 52.71 | 0.007(2) |
| | | $(^3P)3p\ ^2S^o$ | 52.91 | |
| 10 | 53.07 | $(^3P)3p\ ^2P^o$ | 53.08 | 0.027(3) |
| 7a | 55.58 | $(^1D)3p\ ^2F^o$ | 55.59 | 0.009(2) |
| 7 | 55.81 | $(^1D)3p\ ^2P^o$ | 55.83 | 0.024(3) |
| | | $^2D^o$ | 55.95 | |
| 6 | 56.33 | $(^3P)3d\ ^4D$ | 56.19 | 0.020(3) |
| | | $^2D$ | 56.32 | |
| | | $^2F$ or $^4P$ | 56.39 or 56.41 | |
| | | $^2P$ | 56.48 | |
| 6a | 56.66 | $(^3P)4s\ ^2P$ | 56.72 | 0.005(2) |
| 5 | 57.68 | $(^3P)4p\ ^4D^o$ | 57.71 | 0.004(1) |

| | | | | | |
|---|---|---|---|---|---|
| | | + other terms | | | |
| 4 | 57.99 | $(^3P)4p$ | $^2P^o$ | 58.04 | 0.013(2) |
| 3b | 59.04 | $(^3P)4d$ | $^4D$ | 59.00 | 0.016(2) |
| | | | $^2D$ | 59.05 | |
| | | | $^2P$ | 59.15 | |
| 3 | 59.40 | $(^3P)5s$ | $^2P$ | 59.27 | 0.029(3) |
| | | $(^1S)3p$ | $^2P^o$ | 59.43 | |
| | | $(^1D)3d$ | $^2D$ | 59.54 | |
| 3a | 59.67 | $(^3P)5p$ | $^4D^o$ | 59.69 | 0.009(2) |
| | | | $^2P^o$ | 59.85 | |
| 2a | 60.31 | $(^3P)5d$ | | 60.3 | 0.008(2) |
| 2 | 60.96 | $(^1D)4p$ | $^2P^o$ | 60.96 | 0.009(2) |
| 1b | 61.34 | | | | 0.003(1) |
| 1a | 61.64 | | | | 0.003(1) |
| 1 | 62.22 | $(^1D)4d$ | | 62.2 | 0.018(3) |
| 0b | 62.7 | $(^1D)5p$ | | | 0.001(1) |
| 0a | 63.1 | $(^1S)3d$ | $^2D$ | | 0.003(1) |
| 0 | 63.4 | $(^1D)5d$ | | | 0.008(1) |
| -1 | 64.0 | | | | 0.003(2) |
| -2 | 64.4 | $(^1S)4p$ | $^2P^o$ | | 0.003(2) |
| Sat. total | | | | | 0.32 |

---

[a] Ref. 24

[b] Ref. 21

Table III. Asymmetry parameters of Ne valence satellites at three kinetic energies: 0.5 and 1.0 from the present work and 5 eV from Ref. 12; $\beta_{2p}$ from Ref. 38.

| Peak | $\beta$ (0.5 eV) | $\beta$ (1.0 eV) | $\beta$ (5 eV) |
|---|---|---|---|
| 2p | -0.55(7) | -0.63(7) | -0.18(7) |
| 2s | 2 | 2 | 2 |
| 12 | -0.9(3) | | |
| 11 | 0.2(3) | 1.0(6) | 1.7(3) |
| 10 | -0.2(5) | 0.0(3) | -0.2(1) |
| 7 | -0.2(2) | -0.2(3) | 0.0(1) |
| 6 | -0.5(2) | -0.2(4) | |
| 4 | 0.4(3) | | 0.0(1) |
| 3 | 0.5(2) | 0.3(4) | 0.4(2) |

FIGURE CAPTIONS

Fig. 1 a) A schematic diagram of the threshold electron analyzer drawn to scale. Two electron trajectories are represented by long dashed lines. b) The varying potential (V) seen by the photoelectron as it leaves the ionization region and moves toward the microchannel plate detector (scale same as in a)). The arrows point to initial positions for an electron on either side of the ionization region.

Fig. 2 A time spectrum of He taken near the n=2 satellite threshold in 500s (left axis). Also shown is the calculated transmission function expressed as the acceptance half angle $\delta$ (right axis).

Fig. 3 Threshold photoelectron scan of the He satellites. n is the principal quantum number of the remaining electron in $He^+$. The count rate at the maximum of the n=2 satellite peak is 9700 c/s. The line simply connects the data points.

Fig. 4 He satellite cross sections at low kinetic energies shown in a semi-log plot. The n=2 satellite $\sigma$ values are from Woodruff and Samson.[5]

Fig. 5 Asymmetry parameter ($\beta$) of the He satellites displayed as a function of the principal quantum number n of the $He^+$ excited electron. The circles represent two sets of measurements at 0.6 eV (filled circles) and at 1.1 eV (open circles) kinetic energies. The open squares show the calculation of Greene.[27] They are connected by a line only for clarity.

Fig. 6 The relative nl distribution of the excited electron in the threshold satellite spectrum: a) He calculation,[30] b) Ne experiment (this work). For each n the l segments sum to a unit length. Included in the Ne 4d and 5d fractions are unresolved higher l components.

Fig. 7 Threshold photoelectron scan of the Ne 2s main line and valence satellites. The numbers labelling the satellite peaks follow the notation of Wuilleumier and Krause.[32] For clarity the additional peaks are not labelled, but appear in Table II. As in Fig. 3 the line connects the points.

Fig. 8 Ne valence satellite cross sections at low kinetic energies (0-1 eV) from this work along with σ values at higher kinetic energies from Heimann et al.[12] (satellites 4 - 11) and from Becker et al.[13] (satellite 12). For each satellite typical error bars are displayed. In the notation of Table II, satellite 7 includes 6a, 6, 7 and 7a, satellite 3 contains 3a, 3 and 3b, and satellite 4 includes 4 and 5.

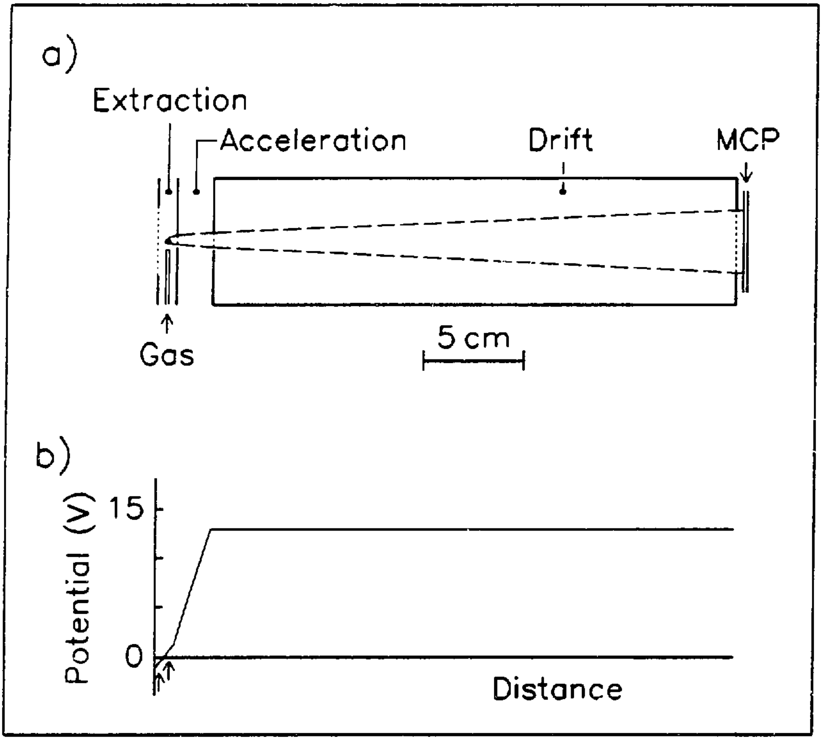

XBL 866-2147

Figure 1

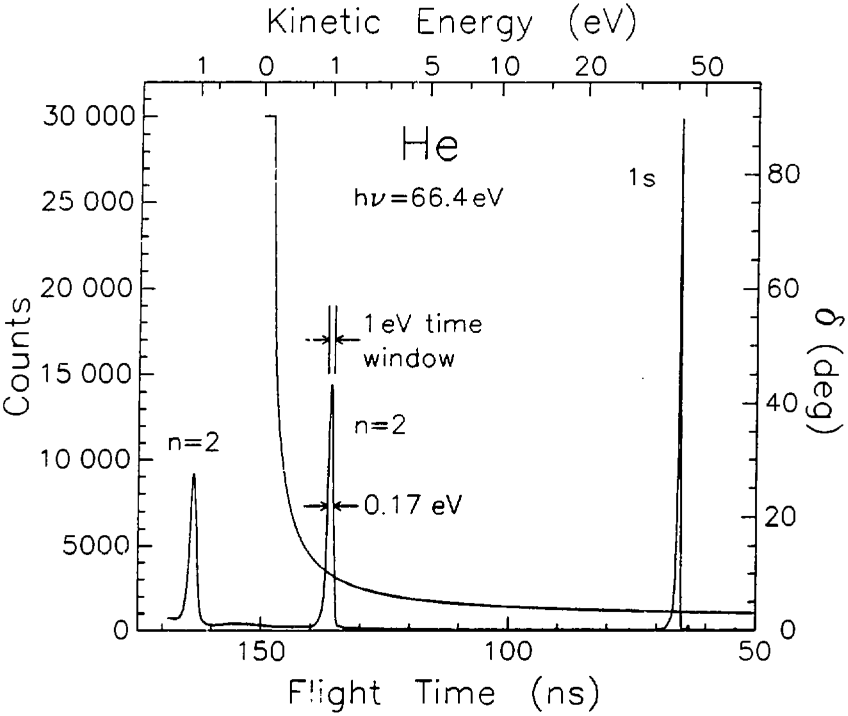

XBL 866-2146

Figure 2

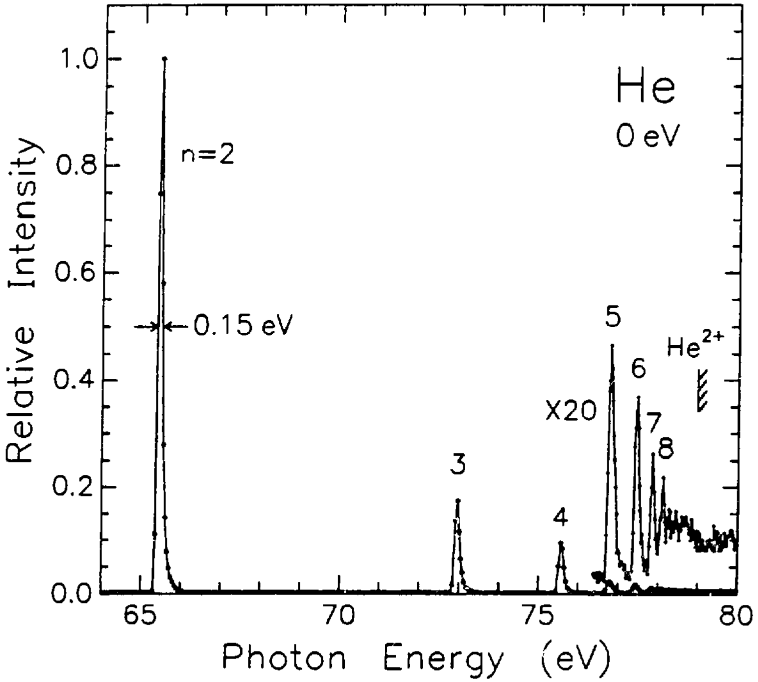

XBL 866-2145

Figure 3

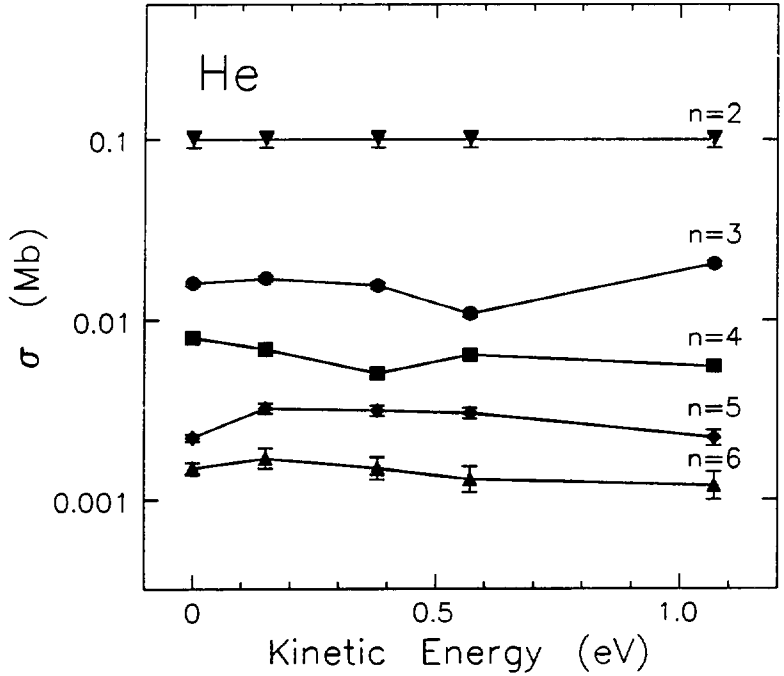

XBL 866-2144

Figure 4

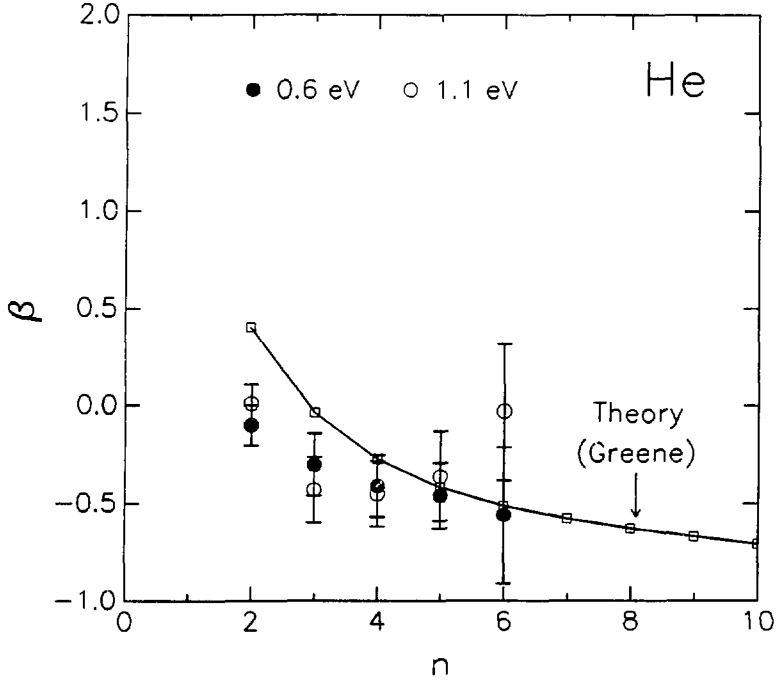

XBL 866-2143

Figure 5

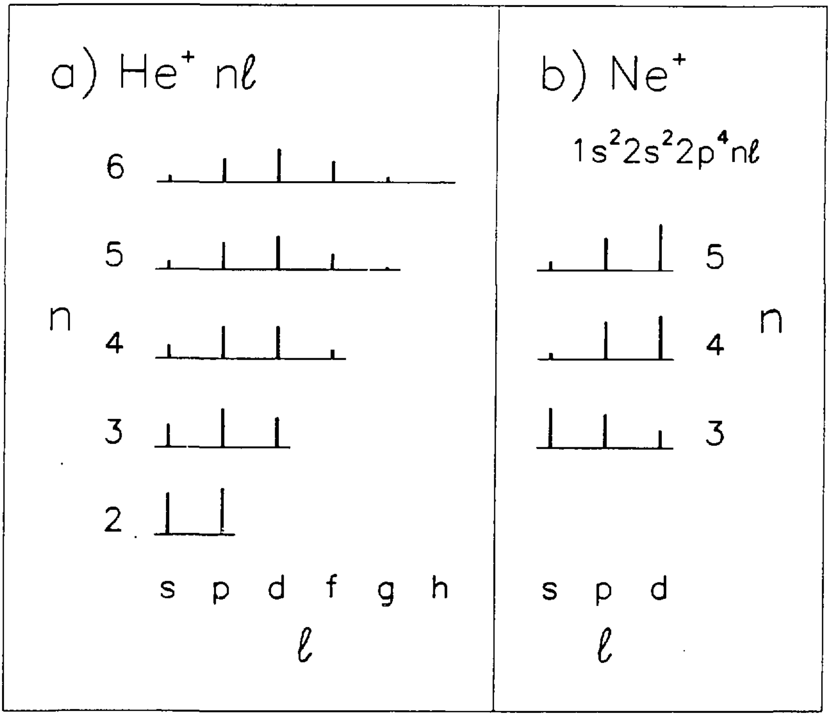

XBL 866-2142

Figure 6

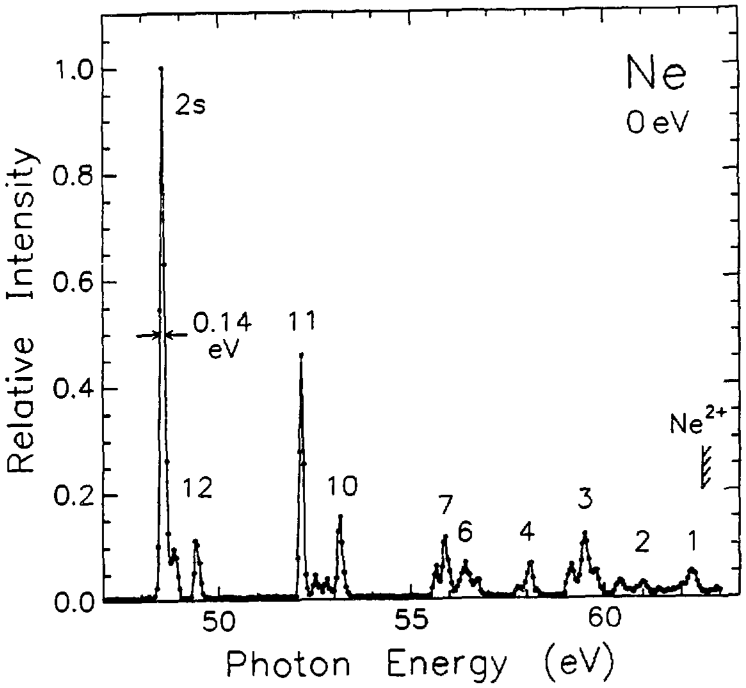

XBL 866-2141

Figure 7

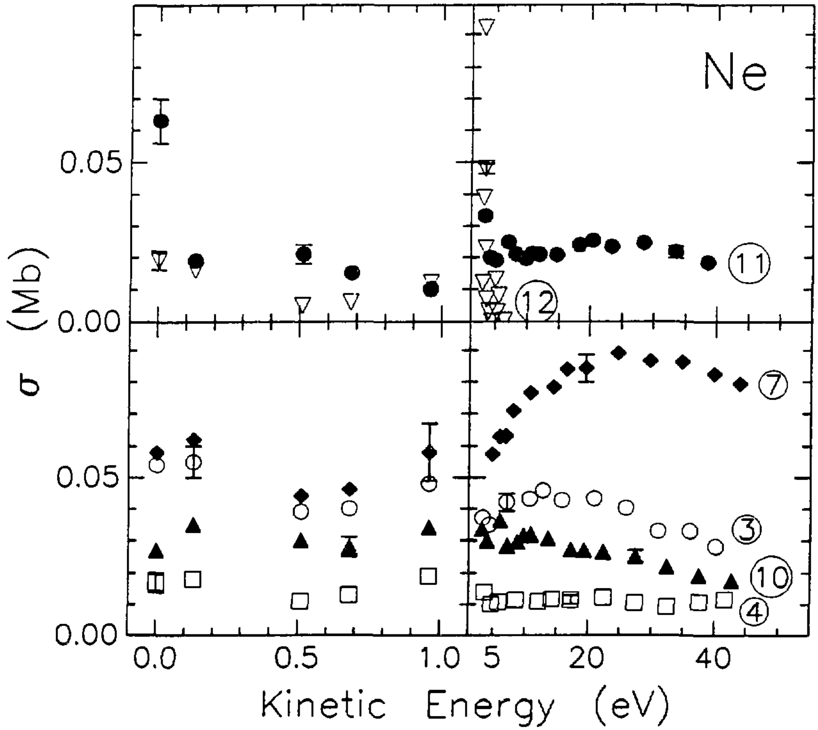

XBL 866-2204

Figure 8

# V. SHAKE-OFF ON INNER-SHELL RESONANCES OF AR, KR, AND XE*

## ABSTRACT

Synchrotron radiation was used to excite an inner-shell electron into a Rydberg orbital: Ar 2p → ns, nd, Kr 3d → np, and Xe 4d → np. The resonant decay into shake-off channels was studied by three different electron measurements. First, threshold electron scans were obtained over the resonances and thresholds. On the first resonance for each atom, photoelectron spectra were collected. The intensity distribution of low kinetic energy electrons was also determined for a few resonances. Finally, a shake calculation was carried out to compare with the experimental shake-off probabilities. Shake-off is observed to be a strong decay channel for these resonances.

## A. INTRODUCTION

A threshold marks the photon energy at which electron ionization in a particular subshell becomes energetically allowed. For inner shells, the step-like onset of photoionization is complicated by two phenomena: discrete resonances and post-collision interaction (PCI). We discuss both briefly as background for the present work on threshold phenomena in rare gases.

At certain energies below threshold, an inner-shell electron may be excited into an unoccupied Rydberg orbital. In krypton, for example, two strong series of resonances have been observed: $3d_{5/2} \rightarrow 5p, 6p, \ldots$ and $3d_{3/2} \rightarrow 5p, 6p, \ldots$.[1] Transitions to nf orbitals are quite weak because of the large barrier in the effective potential for f electrons.[2] Resonances similarly occur in argon below the 2p thresholds and in xenon approaching the 4d thresholds.

A number of recent experiments[3-12] have studied different aspects of the excitation and decay of a particular set of resonances - Ar 2p → ns, nd, Kr 3d → np and Xe 4d → np - which have been studied together[3,4] because of their similarity as inner-shell resonances. Using electron impact, King et al.[3] measured energy-loss spectra, equivalent to photoabsorption scans. Their high-resolution experiment provides precise energies for the resonances and thresholds. Relative values of the oscillator strength f were determined and found to vary approximately with the separation of the resonance energy levels $dE_n/dn$. The decrease in intensity along a Rydberg series results mainly from the overall expansion of the Rydberg orbital.[13] For a given spin-orbit pair of resonances, e.g. Kr $3d_{5/2} \rightarrow np$ and $3d_{3/2} \rightarrow np$, the measured ratios of oscillator strengths were very close to statistical, suggesting that relativistic effects have little influence on the transition strengths of these resonances.

Combining synchrotron radiation and mass spectrometry, Hayaishi et al.[4] examined the cross sections $\sigma$ for the formation of singly, doubly, and triply charged ions. For the argon 2p → ns, nd excitations, $Ar^+$ was found to be the most frequent product of resonant decay. By contrast, in both krypton and xenon the doubly charged ion is the dominant product at the d → np resonances. The Kr and Xe results were unexpected because the spectator model, in which the Rydberg electron remains in an outer orbital while the core undergoes an Auger-like decay, yields a singly-charged ion. Secondly, the linewidths (and consequently the lifetimes) of the Kr and Xe resonances were found to be essentially independent of the principal quantum number n of the Rydberg electron, which suggests that autoionization to $ns^{-1}$ and $np^{-1}$ final states rarely occurs. The Rydberg electron could participate in the resonant decay in some other way, such as being excited (shake-up) or ionized (shake-off). For the most important pathway to doubly-charged ions, Hayaishi et al.[4] proposed a two-step process, such as $\mathrm{Kr}\ 3d_{5/2}^{-1}5p \rightarrow \mathrm{Kr}^+\ 4s^{-1}4p^{-1}5p \rightarrow \mathrm{Kr}^{+2}\ 4p^{-2}$.

Electron spectra at the Kr and Xe resonances have been investigated extensively.[5-11] For both Kr[11] and Xe,[7,10] the observed variations in $\sigma_{ns}$ and $\sigma_{np}$ caused by autoionization were small, < 15 %. The electron spectra agree with the expectations of the spectator model with two important exceptions. First, shake-up of the Rydberg electron during Auger-like decay contributes additional peaks, e.g. $\mathrm{Kr}\ 3d^{-1}5p \rightarrow \mathrm{Kr}^+\ 4p^{-2}6p$.[6,8,9,11] Secondly, on the Xe 4d → np resonances, Becker et al.[10]

qualitatively observed a large continuous background caused by shake-off processes, e.g. Xe $4d^{-1}6p \rightarrow Xe^{2+}\ 5p^{-2}$.

We now address post-collision interaction (PCI) effects. At photon energies just above threshold, photoemission and "subsequent" Auger decay cannot be separated into two independent steps. Niehaus[14] developed a semi-classical model to explain PCI. Initially, the slow photoelectron moves in the Coulomb field of the singly charged ion $A^+$. As Auger emission occurs, the photoelectron finds itself on the more strongly attractive potential curve of the doubly charged ion $A^{+2}$. Recently, the Niehaus theory has been extended by Russek and Mehlhorn[15] to include the time for the Auger electron to "overtake" the photoelectron. Predictions of the new model have been confirmed by a measurement of Xe $N_5O_{23}O_{23}\ {}^1S_0$ Auger electrons by Borst and Schmidt.[16] PCI also causes the $Ar^+$ yield to decrease slowly above the $2p_{1/2}$ threshold as the probability for capture of the photoelectron decreases.[4] At the Kr 3d and Xe 4d thresholds, however, Hayaishi et al.[4] surprisingly found no evidence for PCI in the Kr and Xe ion cross sections.

Wight and Van der Wiel[12] reported a low-resolution (1 eV) threshold scan of Xe over the 4d region. In a threshold spectrum the ejected electrons with very low kinetic energies are collected while varying the photon energy (or equivalently the energy loss of the impact electron). The threshold electron intensity from Xe was enhanced at the below-threshold resonances because of shake-off transitions, e.g. Xe $4d^{-1}nl \rightarrow Xe^{2+}\ 5p^{-2}$. Wight and Van der Wiel also observed that the Xe 4d threshold peaks were distorted by PCI, having a lowered maximum and a tail extending to higher energy.

In this work, we have used high-resolution synchrotron radiation to take threshold electron scans over the Ar 2p, Kr 3d, and Xe 4d threshold regions. Our main purpose was to study quantitatively the shake-off transitions occuring on the below-threshold resonances. We also have determined the threshold lineshapes for comparison with the PCI theory. To measure the total intensity of shake-off electrons on the resonances, photoelectron spectra and intensity distributions of low kinetic energy electrons were obtained. Lastly, a shake calculation of the shake-off probability was carried out using HF wavefunctions.

Some experimental methods are described in Sec. B. Sec. C is devoted to the intensities of threshold electrons on the below-threshold resonances and Sec. D to the threshold lineshape. Sec. E contains the discussion of the photoelectron spectra and the intensity distributions of low kinetic electrons. The results of the shake calculation are described in Sec. F. Finally, the conclusions are presented in Sec. G.

## B. EXPERIMENTAL

This experiment was performed at the Stanford Synchrotron Radiation Laboratory (SSRL) using a grazing incidence "grasshopper" monochromator. Some preliminary work was carried out at the 5.6 m toroidal grating monochromator (TGM) at the Hamburger Synchrotronstrahlungslabor (HASYLAB). In the SSRL studies, two gratings were employed, with 600 and 1200 lines/mm. An Al filter was inserted to reduce the higher-order light of the 600 lines/mm grating. For the threshold electron scans, the monochromator resolution (FWHM) is estimated to be 0.35 eV for Ar and 0.04 eV for Kr and Xe. For the low kinetic energy distributions and photoelectron spectra which require higher flux, the monochromator bandwidth was broader: 1 eV for Ar and 0.2 eV for Kr and Xe.

The threshold scans and low kinetic energy distributions were obtained with a threshold electron analyzer similar to the one described in detail in an earlier paper.[17] Briefly, photoelectrons are extracted by a weak electric field from the interaction region, which results in a very high transmission for zero and low kinetic energies. Following the principle of space focussing,[18] the electrons are energy-analyzed by their flight times between the interaction region and the detector. There are a few differences between the threshold electron analyzer used in the present work and the one described earlier.[17] In this spectrometer the flight path is shorter (215 mm). The angle between the electric vector and the analyzer axis is fixed at 55°, the magic angle, which implies that the measured electron intensities are independent of angular distribution effects. Lastly, during a photon-energy scan, an entire time spectrum is stored for each photon energy. Afterwards, in the data analysis of a single scan, different kinetic energies may be selected by choosing the appropriate energy (time) window. The threshold intensity represents the electron count rate inside a kinetic energy (time) window set to include energies from 0.0 to 0.05 eV. This electron signal is then divided by the photon flux monitored by a sodium salicylate scintillator and photomultiplier tube.

Low kinetic energy distributions of Kr were constructed by varying the kinetic energy window in 0.2 eV steps from 0 to 10 eV. For each of these energies, the intensity of the resonance was divided by that of the 3d photoelectron peaks. These ratios, which are independent of the analyzer transmission, are then multiplied by $\sigma_{3d}$ to obtain the electron intensity distributions. Unfortunately, at these low kinetic energies $\sigma_{3d}$ is not well known. We inferred $\sigma_{3d}$ from the increased threshold electron signal above the 3d thresholds, caused by double-Auger transitions: $Kr^{+}\ 3d^{-1} \rightarrow Kr^{3+}\ 4p^{-3}$. The double-Auger intensity was estimated down to 1.6 eV kinetic energy and then extrapolated to the average 3d threshold. From this analysis, $\sigma_{3d}$ is observed to increase nearly linearly by 70 % from 0 to 10 eV kinetic energy. This result for $\sigma_{3d}$ agrees better with the HF calculation of Manson and Kennedy[19] than with the measurement of Carlson et al.[20] We estimate the combined statistical and calibration uncertainty to be 25 %.

In addition to the threshold scans and low kinetic energy distributions, photoelectron spectra were taken with our other time-of-flight electron spectrometers, where electrons first travel through a field free region before being accelerated, as in this case, or decelerated. These analyzers described by White et al.[21] have a slowly varying transmission function. The photoelectron spectra have been obtained in 2000 s both at 0° and 55° with respect to the light polarization vector. The spectra taken at the two angles gave the same results within error. Off-resonant spectra have been subtracted in order to account for the analyzer dark counts and the photoelectrons resulting from second-order light. Secondly, the spectra have been corrected for the analyzer transmission function as determined by calibration with Ne 2s and 2p photoelectron peaks. The analyzer resolution varies with kinetic energy as 0.05•E.

## C. THRESHOLD ELECTRON INTENSITIES, RESONANT SHAKE-OFF

Figures 1, 2, and 3 display threshold scans over the Ar 2p, Kr 3d, and Xe 4d thresholds. Table I shows the relative oscillator strengths f from King et al.[3] and the relative threshold intensities obtained from fits of the scans shown in Figs. 1, 2, and 3. The values of f on the resonances were inferred from King et al.'s Eq. (5) and the reported df/dE and $n^*$.

The threshold scans contain the following features: a constant level at lower energies from the analyzer background and valence shake-off, e.g. $\mathrm{Kr} + h\nu \rightarrow \mathrm{Kr}^{2+}\ 4p^4 + 2e^-$, and a constant signal above the thresholds, which is higher as a result of double Auger events, e.g., $\mathrm{Kr}^+\ 3d^{-1}4p^6 \rightarrow \mathrm{Kr}^{3+}\ 4p^3 + 2e^-$. Strong, nearly Lorentzian peaks are observed at resonances below threshold from the shake-off decay of the excited state, e.g. $\mathrm{Kr}\ 3d^{-1}5p \rightarrow \mathrm{Kr}^{2+}\ 4p^4 + 2e^-$. These resonant shake-off transitions resemble the double Auger events above threshold. Finally, at the inner-shell thresholds, there are peaks due to near 0 eV kinetic energy photoelectrons, e.g. $\mathrm{Kr} + h\nu \rightarrow \mathrm{Kr}^+\ 3d^{-1} + e^-$, which are broadened and shifted to higher photon energy hν by the post-collision interaction (PCI) between the slow photoelectron and the faster Auger electron.

In considering the threshold intensity on the resonances, it should be kept in mind that many of the possible decay channels produce ejected electrons with high kinetic energy, such as the spectator Auger-like decay Kr $3d^{-1}5p \rightarrow Kr^{+}\ 4p^{-2}5p + e^{-}$. Even shake-off decay rarely produces an electron with low enough kinetic energy to be included in the threshold scan because, in general, tens of electron volts of energy are partitioned between two electrons. In contrast, at threshold, all of the inner-shell photoelectrons will have the correct low energy to contribute to the threshold intensity. The prominent appearance of the resonances is therefore quite remarkable.

To interpret intensities of resonances in the threshold scans, it is necessary to place the threshold intensities on some scale of oscillator strength. On a resonance, the threshold intensity $I_{th}$ will depend first on the shake-off oscillator strength $f_s$. A second factor is the functional form of the continuous distribution of shake-off electrons $df_s/dKE$, since the threshold analyzer detects only a small part of this distribution near 0 eV kinetic energy. Including the analyzer collection efficiency e(KE),

$$I_{th} = \int_{0}^{\Delta E} \frac{df_s}{dKE}\, e(KE)dKE \approx \left.\frac{df_s}{dKE}\right|_0 e_{av}\ \Delta E, \qquad (1)$$

where $e_{av}$ is an average analyzer efficiency for the accepted electrons with energies from 0 to $\Delta E$. At a threshold the total oscillator strength is collected:

$$I_{th} = \int_{0}^{\Delta E} \frac{df}{dh\nu}\, e(KE)dh\nu \approx \left.\frac{df}{dh\nu}\right|_{BE} e_{av}\ \Delta E. \qquad (2)$$

By dividing $I_{th}$ at the threshold by the known $df/dE$, a constant $N = e_{av}\Delta E$ is obtained, which also includes the arbitrary scaling constant of the relative absorption and threshold measurements. Finally at each resonance,

$$\frac{I_{th}}{Nf} \approx \frac{1}{f}\left.\frac{df_s}{dKE}\right|_0, \qquad (3)$$

which is the fraction of the resonance resulting in shake-off with an electron at low kinetic energy. The resulting values are displayed in the last column of Table I.

In the preceding derivation, it was assumed that two electrons from the same ionization event do not fall within the analyzer kinetic-energy window and that the shake-off distribution is slowly varying over this window. The narrow analyzer resolution (0.1 eV) implies that both these approximations are reasonable. In analyzing the threshold electron spectrum of $N_2O$, Baer et al.[22] carried out a similar analysis comparing (threshold electron) / (ion) ratios at autoionizing resonances and at threshold.

For all the Kr and Xe resonances in Table I, we note first that the threshold shake-off fractions are surprisingly large, which implies that shake-off is an important decay path. Secondly, for all three atoms the fractional yield of a resonance leading to low-energy electrons increases with n. This n dependence suggests that in the shake-off decay the Rydberg electron is usually ejected along with a valence electron. For the higher-n resonances the Rydberg electron becomes less strongly bound, and the ejection of this electron should become more facile. In comparison, Kr and Xe ion-yield measurements[4,23] showed the fractions of single and double ions varying slowly over the resonances, while the triple ion increases with n. In the case of Xe, Eland et al.[23] have proposed that $Xe^{2+}$ results mainly from two step processes while $Xe^{3+}$ is produced by direct shake-off. The ion-yield measurements imply that the cross section for shake-off decay increases with n. The variation of the threshold intensities with n can only suggest an n dependence for the total shake-off strength. The kinetic-energy distribution is another factor, which will be seen below to vary from one resonance to another.

Ar shows different behavior, having very low threshold intensities on the first two resonances and intensities similar to Kr and Xe on the unresolved higher resonances. The ion yields on the Ar resonances also differ from Kr and Xe.[4] The Ar $2p^{-1}nl$ configurations decay mainly to singly charged ions. The fraction of double and triple ions that do result increases strongly with n. Apparently, shake-off is unusually weak for the lower resonances of Ar.

For a mechanism to contribute to the threshold electron intensity on resonance, at least two electrons must be ejected at once. The excess energy is shared, with a finite probability of either electron having very little kinetic energy. Consequently, the predominant pathways for creating threshold electrons should be single step decays from the neutral excited state to doubly- and triply-charged ion final states. Figure 4 shows three possible shake-off decay paths from the $3d^{-1}5p$ resonant state of Kr in which: (1) two valence electrons are ejected, (2) the Rydberg electron is ejected along with a valence electron, and (3) the Rydberg electron and two valence electrons are ejected. For path (1), the same orbitals nl are involved as in double Auger above threshold, e.g. $Kr^{+}\ 3d^{-1} \rightarrow Kr^{3+}\ 4p^{-3}$. The double Auger signal intensity, divided by the intensity of the threshold peaks, $Kr \rightarrow Kr^{+}\ 3d^{-1}$, yields an Auger yield ratio R. The values of R determined from the data shown in Figs. 1-3 are 0.010(2) $eV^{-1}$ (Ar), 0.028(9) $eV^{-1}$ (Kr), and 0.15(2) $eV^{-1}$ (Xe). These R values may provide an estimate for the contribution of the ejection of two valence electrons to the resonant threshold intensities, when compared with the values of $\frac{1}{f}\frac{df_s}{dKE}\Big|_0$ given in column 6 of Table I. For Xe, where $\sigma_{4d}$ rises steeply from threshold, this double Auger intensity must be considered as an upper bound. Since the Rydberg electron does not change its orbital, the probability of ejecting two valence electrons should be nearly independent of n. In most of the cases in Table I, this type of resonant shake-off seems to contribute a significant minority share of the threshold electron intensity.

The relative importance of the other kinds of shake-off are more difficult to evaluate. Shake-off to the triply-charged ion is expected to be important at threshold because it ejects three electrons sharing relatively little energy, e.g. Kr $3d_{5/2}^{-1}5p \rightarrow 4p^{-3} + 3e^-$, where the total available kinetic energy is 15.7 eV.[24]

The spin-orbit branching ratios for ionization at zero kinetic energy are determined from the intensities of the two threshold peaks: $2p_{3/2}/2p_{1/2} = 1.63(5)$ (Ar), $3d_{5/2}/3d_{3/2} = 1.6(1)$ (Kr), and $4d_{5/2}/4d_{3/2} = 1.8(1)$ (Xe). In Ar and Xe, deviations are observed in opposite directions from the statistical ratios of 2 and 1.5, respectively. In general, it is expected that the branching ratio near threshold should be greater than statistical because the $j=l+1/2$ orbital will be slightly more diffuse and will have better overlap with the low-energy continuum orbital.[25] Because of the delayed onset in the $d \rightarrow \varepsilon f$ channel, the p wave should dominate at threshold for Kr and Xe.[2] The branching ratios of King et al.[3] agree with our results for Ar and Kr, but disagree for Xe, where their result is 1.3(2). Both Auger electron[7] and photoelectron experiments[26] have shown greater than statistical values for Xe. Unfortunately, quantative comparison cannot be made with those branching ratios, because they were determined with both spin-orbit components at the same photon energy. Another Auger-electron measurement[27] has shown the Kr $3d_{5/2}:3d_{3/2}$ ratio to be very close to the statistical value from 97 to 200 eV photon energy. For Kr at 10 eV kinetic energy, Huang et al.[28] calculated the $3d_{5/2}:3d_{3/2}$ ratio to be 1.51, slowly decreasing from higher energy. For Xe the calculated branching ratio has larger changes with energy. At 9 eV kinetic energy, Huang et al.[28] predict $4d_{5/2}:4d_{3/2}$ to be 1.5, increasing from higher energy. For all three atoms, the threshold shake-off fractions in Ar and Kr are the same for pairs of spin-orbit split resonances, e.g. Kr $3d_{5/2} \rightarrow 5p$ and $3d_{3/2} \rightarrow 5p$.

The resonant threshold intensities increase from Ar to Kr to Xe. In part, this trend results from the narrowing of the shake-off kinetic-energy distribution in going from Ar to Xe. Considering the first resonances of the three atoms, the maximum kinetic energy for two emitted electrons decreases from 201.0 eV (Ar) to 52.6 eV (Kr) and to 32.0 eV (Xe).[24,29] In the case of double Auger above threshold, the increasing trend of threshold intensities may be compared with the results of ion measurements. Above the inner-shell threshold but below the threshold for double ionization of an inner and outer electron, the double Auger probability can be inferred from the triple ion / double ion ratio R: $R[Ar(L_{2,3}\text{-}MMM)] = 0.11$, $R[Kr(M_{4,5}\text{-}NNN)] = 0.17$, and $R[Xe(N_{4,5}\text{-}OOO)] = 0.19$.[4] The increasing double Auger probability with

Z correlates with the decreasing binding energy and increasing <r> of a valence electron.

## D. THRESHOLD ELECTRON LINESHAPES, POST-COLLISION INTERACTION (PCI)

Using a semi-classical model, Niehaus[14] calculated an Auger lineshape which depends on the lifetime of the hole state $\tau$ and the excess photon energy above threshold $\Delta = h\nu - IP$. Since the Auger energy gain equals the photoelecton energy loss, his expression may be converted into a lineshape for the threshold photoelectron. Starting from his Eqs. (6), (7), and (14), and setting the Auger energy shift equal to $\Delta$ because 0 eV kinetic energy electrons are detected, we have:

$$P(\Delta) = \frac{1}{2\tau\ \Delta^{5/2}} \exp(-t_* / \tau) \qquad (4)$$

$$\text{where } t_* = \frac{1}{\sqrt{2}\ \Delta} \{\frac{\sqrt{2}}{\sqrt{\Delta}} - \sqrt{1+\Delta} - \frac{1}{2\sqrt{\Delta}} (1.763 + \ln[\frac{\sqrt{1+\Delta} - \sqrt{\Delta}}{\sqrt{1+\Delta} + \sqrt{\Delta}}])\}. \qquad (5)$$

The peaks at the inner-shell thresholds were fit to the Niehaus function convoluted with a gaussian representing the monochromator bandwidth. These fits are depicted in Fig. 1 (Ar $2p_{3/2}$, $2p_{1/2}$), Fig. 2 (Kr $3d_{5/2}$, $3d_{3/2}$), and Fig. 3 (Xe $4d_{5/2}$, $4d_{3/2}$). For all three threshold scans the agreement between the fit and the data is excellent, confirming the validity of the Niehaus model, even when the Auger decay occurs while the photoelectron is still near the nucleus. In principle, interference could be present in the second threshold peak since paths through the two $j=l\pm1/2$ hole states can reach the same multiple-ion final states. This interference is not observed, perhaps because the threshold intensity sums over a number of Auger transitions, or perhaps because of insufficient resolution.

Table II displays the natural linewidths of the resonances Ar $2p_{3/2} \rightarrow 4s$ from King et al.[3] and Kr $3d_{5/2} \rightarrow 5p$ and Xe $4d_{5/2} \rightarrow 6p$ from fits of our resonant threshold intensities using a Voigt function. These values for the Kr and Xe resonant linewidth agree reasonably well with those of King et al.[3] and Hayaishi et al.[4] The observation of Hayaishi et al.[4] that the linewidths for Kr and Xe are the same for all np resonances is consistent with the present results. Along with the resonance linewidths, Table II also shows the widths $1/\tau$ of the Neihaus function[14] which best fit the threshold photoelectron peak shapes, from the PCI theory fits. For Ar and Kr, the linewidths (and lifetimes) of the resonance and threshold peaks agree within error, which is expected since the primary Auger process will be little perturbed by the presence of a bound Rydberg electron or slow photoelectron. For Xe, however, the threshold linewidth is significantly smaller than the resonant linewidth. The apparent longer lifetime of the Xe 4d hole at threshold may result from Neihaus's neglect[14] of the time interval taken for the Auger electron to overtake the photoelectron. In Xe this transit time will be longer than in Ar and Kr, since the average Auger energy is smaller. No comparison has been made to the calculated PCI lineshape of Russek and Mehlhorn,[15] whose expression contains terms which diverge for 0 eV photoelectron energy. From the comparison of the kinetic energy of the Xe $N_5O_{23}O_{23}\ {}^1S_0$ with the predictions of Russek and Mehlhorn, Borst and Schmidt[16] inferred a natural linewidth of 0.11 eV. An alternative explanation of the Xe threshold width is that the interaction between a slow photoelectron and a slow Auger electron cannot be approximated simply by a change in the photoelectron potential from $1/r$ to $2/r$.

## E. RESONANT KINETIC ENERGY SPECTRA

To view the total picture of a resonance decaying into shake-off, Auger-like and main-line channels, electron spectra containing electrons of all kinetic energies must be measured. Figures 5-7 show spectra taken at the $2p_{3/2} \rightarrow 4s$ resonance of Ar, the $3d_{5/2} \rightarrow 5p$ resonance of Kr and the $4d_{5/2} \rightarrow 6p$ resonance of Xe. The appearance of the Xe spectrum in Fig. 7 is affected by the presence of electrons in an adjacent "bucket" in the storage ring, which resulted in additional counts on the low kinetic energy side of each peak. By the subtraction of a near-lying off-resonance spectrum, the $ns^{-1}$ and $np^{-1}$ main lines have been eliminated in each case. However, as has been discussed above, autoionization into main-line channels is weak.[4,7,10,11]

These spectra have three types of features. Discrete peaks observed at higher kinetic energies result from Auger-like transitions in which the excited electron plays a spectator role or is shaken up into a higher nl orbital. The final states corresponding to some of the peaks at higher energy can decay further. At lower kinetic energies, discrete peaks are caused by second step Auger transitions from these excited states of the singly charged ion. Table III shows the energies and assignments of some of the second-step decays. This list of second-step Auger peaks is incomplete, and does not reflect completely the large possible number of these transitions. Lastly, a continuous background is observed resulting from shake-off transitions. In agreement with the results of the threshold scans, the continuous electron signal is strong in the photoelectron spectra. It should also be noted for Kr and Xe that the continuous background at high kinetic energy is low, even though the shake-off distribution resulting in $np^{-2}$ final states should extend to 52.5 eV for Kr and 32.0 eV for Xe.[24,29] This observation suggests that $np^{-2}$ is not an important final configuration for shake-off.

The resonant shake-off intensities given in Table III were evaluated by drawing a linear background function underneath the peaks in Figs. 5-7. A number of unresolved peaks, taken together, could resemble background. This is a concern which is reflected in the large error bars. In the analysis of the Kr and Xe spectra, we used the higher-resolution spectra of Aksela et al.[8,9] as a guide for the number and location of the peaks. To obtain the shake-off probability, the total number of background electrons must then be divided by the average number of electrons ejected in a single shake-off transition, approximately $(2\sigma_{2+}+3\sigma_{3+}) / (\sigma_{2+}+\sigma_{3+})$. The ion ratios[4] measured on these resonances give 2.1 shake-off electrons per event for Ar, 2.1 for Kr, and 2.0 for Xe. The fractions of these resonances resulting in shake-off and second-step Auger transitions are displayed in Table III. The reported second-step fractions must be viewed as lower bounds, partly because they only include peaks at energies above 5 eV and partly because of the uncertainty in the shake-off background subtraction. In Kr, for example, by assuming that $4s^{-1}4p^{-1}nl$ and $4s^{-2}nl$ states lead to further Auger electrons, while $4p^{-2}nl$ states do not, an alternative estimate of the second-step Auger contribution can be obtained. In the case of Kr, this method gave a much higher value for the 2nd step Auger, 45 % of the resonant strength. The resulting shake-off fraction is still within the error limits of 37(8) %.

The shake-off contributions increase from Ar to Kr to Xe. For all three atoms, the resonant shake-off intensity is of comparable or greater strength than the two-step Auger-like transitions. This result conflicts with the discussions of Hayaishi et al.[4] and Eland et al.,[23] who tentatively concluded that $Ar^{2+}$, $Kr^{2+}$, and $Xe^{2+}$ dominantly result from sequential decays. With regard to the formation of triply charged ions, three discrete steps are excluded by energy considerations. Therefore, triply charged ions should always result from shake-off either directly from the neutral excited state or possibly in two steps, such as $Kr\ 3d^{-1}np \rightarrow Kr^{+}\ 4s^{-2}np \rightarrow Kr^{3+}4p^{-2}$. In Xe, the $4d_{5/2} \rightarrow 6p$ resonance is only 0.7 eV above the $Xe^{3+}$ threshold,[29] and can only access $Xe^{3+}$ when three electrons leave simultaneously with very low kinetic energy. Qualitative ion ratios can be derived from the analysis of these photoelectron spectra. The derived ion ratios agree with the mass spectrometry results for Ar and Xe,[4,23] but not for Kr, for which a very small cross section to $Kr^{+}$ was reported.[4] Compared with a total $\sigma$ of 7.5 Mb at the Kr $3d_{5/2} \rightarrow 5p$ resonance,[4] $Kr^{+}$ will be formed from the $4s^{-1}$ and $4p^{-1}$ main lines, 0.50 Mb,[11] and from nearly all the $4p^{-2}nl$ spectator lines, 1.5 Mb. (The $Kr^{+}$ $(^{1}S)4p^{-2}6p$ state can further Auger decay). It is interesting that Hayaishi et al.[4] observed no PCI effect in the Kr and Xe ion yields. Related to the high shake-off probability, the slow photoelectron cannot be captured in a high Rydberg state.

Figure 8 shows the low-kinetic-energy distribution of emitted electrons on two resonances of Kr. The intensity decreases steeply from 0 eV kinetic energy for both resonances. For the $3d_{5/2} \rightarrow 5p$ resonance, as seen in Fig. 6, a number of discrete transitions fall between 5 and

10 eV. The kinetic-energy distribution of resonant shake-off electrons should resemble that of the nonresonant double photoionization of valence shells, e.g. $Ne + h\nu \rightarrow Ne^{2+}\ 2p^4 + 2e^-$, which has been studied experimentally by Carlson[30] and theoretically by Chang and Poe.[31] For Ne with the ejected electrons sharing a total kinetic energy (TKE) of ~200 eV, Carlson observed an order-of-magnitude decrease from TKE to TKE/2. An identical decrease must occur between 0 and TKE/2. Using many-body perturbation theory, Chang and Poe calculated kinetic-energy distributions, also for Ne, which become less peaked as the photon energy decreases toward the double-ionization threshold. Resonant shake-off transitions to double ions reach the same final states as valence double photoionization, and the two processes may be considered to be the same.

For the Kr $3d_{5/2} \rightarrow 7p$ resonance the intensity decreases from 0 eV more quickly than for the 5p resonance. A similar change in slope was observed for the Xe $4d_{5/2} \rightarrow 6p$ and 7p low-kinetic-energy distributions. In general, the shake-off distributions of higher nl resonances seem to be more sharply peaked at 0 eV. Theoretical effort aimed at explaining this unexpected behavior of the resonant shake-off intensity would be valuable. As a consequence of the changing kinetic-energy distributions, the threshold intensities of the resonances cannot be interpreted as proportional to the total shake-off probability. In part, the higher fractional threshold intensity of the Kr $3d_{5/2} \rightarrow 7p$ resonance must result from the sharper peaking of the shake-off distribution at 0 eV. Although photoelectron spectra were taken on some of the higher nl resonances, their quality was insufficient to confirm that the total shake-off contribution increases with n as implied by the ion yields.

From the photoelectron spectra and low-kinetic-energy distributions, a number of observations can be made about the shake-off decay of these resonantly excited states. First, shake-off is a strong decay channel which is inconsistent with the spectator model. Its importance is less surprising when compared with the intensity of double-Auger transitions above threshold. Shake-off makes a major contribution to the double-ion yield and is solely responsible for the triply-charged ions. For the first resonances the importance of shake-off increases from Ar to Kr and reaches a probability of about 50 % for Xe. The main final states of shake-off are configurations other than $np^{-2}$, suggesting the influence of configuration interaction in the decay final states. The resonant shake-off distribution has a maximum at zero kinetic energy. From 0 eV, the slope of the decreasing intensity becomes steeper for the higher n resonances.

## F. SHAKE CALCULATION

Carlson and coworkers[32,33] used shake theory and single-configuration wavefunctions to calculate shake-off probabilities accompanying photoionization or Auger decay. The mechanism considered by this model is the sudden change of the potential. The shake probability $P_{nl}$, which includes shake-up to discrete levels as well as shake-off to the continuum, is given by:

$$P_{nl} = 1 - [\int \Psi_{nl}(A_f)\Psi_{nl}(A_i)dr]^{2N} - P_F. \qquad (1)$$

Here, $\Psi_{nl}$ represent the neutral ($A_i$) and ionic ($A_f$) radial wavefunctions (multiplied by r), and N is the number of electrons occupying the nl subshell. $P_F$ corrects for the finite calculated probabilities for transitions to filled subshells. In the cases discussed below, $P_F$ is not important. The agreement with experiment is qualitatively good, within a factor of two, except when photoionization (or Auger decay) and shake-off involve two electrons from the same shell. In this case, many-body effects cannot be neglected. As a result, the shake-theory estimates for double Auger, for example Ar $L_{2,3}$-MMM, are much too low.[33]

Table IV shows the results of a calculation using Eq. (1) for the shake probability on the Ar 2p → ns, nd, Kr 3d → np and Xe 4d → np resonances. The calculations were performed with the Robert Cowan RCN program.[34] We consider for each atom the transition in which a valence p electron fills the hole and another valence p electron is ejected. Figure 9 shows the radial wavefunctions of Ar before and after the Auger-like decay: Ar $2p^{-1}3d \rightarrow Ar^{+}\ 3p^{-2}3d$. The electron kinetic energy will be somewhat higher than the Ar LMM Auger energy above threshold, about 200 eV, and as a result the sudden approximation should be valid. For Kr and Xe the Auger kinetic energies are less, from below 10 eV to 60 eV,[8,9] and the sudden approximation may not be valid.

The calculated shake probability of the valence electrons is quite small, i.e. < 1 %. This result does not have predictive value since all the electrons involved are from the M shell and correlation cannot be neglected. It is interesting, however, that for valence orbitals the potential change resulting from the Auger-like transition is small: an extra core electron is gained which screens the outer electrons well, while two valence electrons, which screen imperfectly, are lost. These effects largely cancel. The 3s and 3p radial wavefunctions of $Ar^+$ are in fact nearly indistinguishable from those of Ar shown in Fig. 9.

The calculated shake probability of the Rydberg electron is large, and it increases with n until it reaches nearly unity at the third or fourth resonanace. The behavior of all three atoms is rather similar. Qualitatively these results may be explained by considering the slowly-varying, nearly-Coulombic potential at large r, approximately given by $\frac{1}{r}$ or $\frac{2}{r}$, which when changed from $\frac{1}{r}$ to $\frac{2}{r}$ may cause the Rydberg orbital to move dramatically toward the nucleus, as seen for Ar 3d in Fig. 1. At smaller r there exists a potential barrier from the centrifugal and Coulomb repulsion terms. For higher n the Rydberg orbital, being further from the repulsive barrier, can contract more upon ionization. The potential at large r should be similar for all three atoms, in agreement with the similar shake probabilities. In addition, there is a dependence on l, with the shake probability following the sequence $P_d > P_p > P_s$.

Further caution must be exercised with regard to the results of the shake calculation. If overlap integrals are calculated between the Rydberg orbital before Auger-like decay and higher Rydberg orbitals afterwards, the excitation to discrete levels can be estimated. However, the resulting excitation probability accounts for nearly the total shake probability, which does not agree with the experimental observation of the importance of shake-off. It is therefore concluded that the accuracy of this calculation is not sufficient to partition the total shake contribution into shake-up and shake-off components. The shake calculation does give the correct qualitative results that the Rydberg electron has a high shake-off probability, and that it increases with n.

## G. CONCLUSION

From the measurement of electron spectra at zero and higher kinetic energies, a detailed, though qualitative picture of shake-off has emerged for the resonances below the Ar 2p, Kr 3d, and Xe 4d thresholds. First of all, shake-off together with shake-up is a very important channel in the decay of the hole. This tends to invalidate the spectator model. For the first resonances, Ar $2p_{3/2} \rightarrow 4s$, Kr $3d_{5/2} \rightarrow 5p$, and Xe $4d_{5/2} \rightarrow 6p$,the shake-off probability increases from Ar to Kr and becomes about 50 % for Xe. The shake-off intensity also increases with the quantum number n of the Rydberg electron; i.e., with the Rydberg orbital becoming more diffuse. In resonant shake-off, a valence electron and the Rydberg electron are usually ejected. For the Kr $3d_{5/2} \rightarrow 5p$ and Xe $4d_{5/2} \rightarrow 6p$ resonances, it was found that $np^{-2}$ final states are unimportant. This observation suggests the influence of final-ionic-state configuration interaction. The kinetic energy distribution of shake-off electrons decreases from 0 eV, with a steeper slope for higher-n resonances. The high probability for ejection of the Rydberg electron is explained by the independent-electron shake calculation. When the core rearranges to fill the hole, the potential for the nl Rydberg orbital becomes more attractive, which causes that orbital to contract and makes it likely that the Rydberg electron will go into another orbital. Further study of shake-off on these and other resonances is needed. A more sophisticated calculation of the resonant shake-off probability, including electron correlation effects, would be valuable. Higher resolution photoelectron spectra could more quantitatively determine the relative contributions of shake-off and two step transitions.

## REFERENCES

*Work done in collaboration with D.W. Lindle, T.A. Ferrett, S.H. Liu, L.J. Medhurst, M.N. Piancastelli, D.A. Shirley, U. Becker, H.G. Kerkhoff, B. Langer, D. Szostak, and R. Wehlitz

1. K. Codling and R.P. Madden, Phys. Rev. Lett. 12, 106 (1964).
2. U. Fano and J.W. Cooper, Rev. Mod. Phys. 40, 441 (1968).
3. G.C. King, M. Tronc, F.H. Read, and R.C. Bradford, J. Phys. B 10, 2479 (1977); G.C. King and F.H. Read, in Atomic Inner-shell Physics, ed. B. Crasemann (Plenum Press, N.Y., 1985), p. 317.
4. T. Hayaishi, Y. Morioka, Y. Kageyama, M. Watanabe, I.H. Suzuki, A. Mikuni, G. Isoyama, S. Asaoka, and M. Nakamura, J. Phys. B 17, 3511 (1984).
5. W. Eberhardt, G. Kalkoffen, and C. Kunz, Phys. Rev. Lett. 41, 156 (1978).
6. V. Schmidt, S. Krummacher, F. Wuilleumier, and P. Dhez, Phys. Rev. A 24, 1803 (1981).
7. S.H. Southworth, U. Becker, C.M. Truesdale, P.H. Kobrin, D.W. Lindle, S. Owaki, and D.A. Shirley, Phys. Rev. A 28, 261 (1983).
8. H. Aksela, S. Aksela, G.M. Bancroft, K.H. Tan, and H. Pulkkinen, Phys. Rev. A 33, 3867 (1986).
9. H. Aksela, S. Aksela, H. Pulkkinen, G.M. Bancroft, and K.H. Tan, Phys. Rev. A 33, 3876 (1986).
10. U. Becker, T. Prescher, E. Schmidt, B. Sonntag, and H.E. Wetzel, Phys. Rev. A 33, 3891 (1986).
11. D.W. Lindle, P.A. Heimann, T.A. Ferrett, M.N. Piancastelli, and D.A. Shirley, unpublished.

12. G.R. Wight and M.J. Van der Wiel, J. Phys. B 10, 601 (1977).

13. U. Fano and J.W. Cooper, Phys. Rev. 137, A1364 (1965).

14. A. Niehaus, J. Phys. B 10, 1845 (1977).

15. A. Russek and W. Mehlhorn, J. Phys. B 19, 911 (1986).

16. M. Borst and V. Schmidt, Phys. Rev. A 33, 4456 (1986).

17. P.A. Heimann, U. Becker, H.G. Kerkhoff, B. Langer, D. Szostak, R. Wehlitz, D.W. Lindle, T.A. Ferrett, and D.A. Shirley, Phys. Rev. A 34, 3782 (1986).

18. W.C. Wiley and I.H. McLaren, Rev. Sci. Instrum. 26, 1150 (1955).

19. D.J. Kennedy and S.T. Manson, Phys. Rev. A 5, 227 (1972).

20. T.A. Carlson, M.O. Krause, F.A. Grimm, P.R. Keller, and J.W. Taylor, Chem. Phys. Lett. 87, 552 (1982).

21. M.G. White, R.A. Rosenberg, G. Gabor, E.D. Poliakoff, G. Thorton, S.H. Southworth, and D.A. Shirley, Rev. Sci. Instrum. 50, 1268 (1979).

22. T. Baer, P.M. Guyon, I. Nenner, A. Tabche-Fouhaille, R. Botter, L.F.A. Ferreira, and T.R. Govers, J. Chem. Phys. 70, 1585 (1979).

23. J.H.D. Eland, F.S. Wort, P. Lablanquie, and I. Nenner, Zeitschrift für Physik, to be published.

24. C.E. Moore, Atomic Energy Levels, NBS Circular 467 (U.S. GPO, Washington, D.C., 1949), Vol. 2.

25. T.E.H. Walker and J.T. Waber, J. Phys. B 7, 674 (1974).

26. B.W. Yates, K.H. Tan, L.L. Coatsworth, and G.M. Bancroft, Phys. Rev. A 31, 1529 (1985).

27. S. Aksela, K.H. Tan, G.M. Bancroft, H. Aksela, B.W. Yates, and L.L. Coatsworth, Phys. Rev. A 32, 1219 (1985).

28. K.N. Huang, W.R. Johnson, and K.T. Cheng, At. Data Nucl. Data Tables 26, 33 (1981).

29. R. Dutil and P. Marmet, Int. J. Mass Spect. Ion Phys. 35, 371 (1980).

30. T.A. Carlson, Phys. Rev. 156, 142 (1967).

31. T.N. Chang and R.T. Poe, Phys. Rev. A 12, 1432 (1975).

32. T.A. Carlson and C.W. Nestor, Phys. Rev. A 8, 2887 (1973).

33. T.A. Carlson and M.O. Krause, Phys. Rev. Lett. 17, 1079 (1966).

34. R.D. Cowan, The Theory of Atomic Structure and Spectra (Univ. of California Press, Berkeley, 1981).

Table I. Threshold intensities from this work, and energies and oscillator strengths from King et al.[3]

| Atom | Transition | Energy (eV) | Oscillator Strength f | Threshold Intensity $I_{th}$ | $\frac{1}{f}\frac{df_s}{dKE}\Big\|_0(eV^{-1})$ |
|---|---|---|---|---|---|
| Ar | $2p_{3/2} \rightarrow 4s$ | 244.39(1) | 0.51(5) | 0.22(5) | 0.015(4) |
| | 3d | 246.93(1) | 1 | 1.00(15) | 0.034(6) |
| | 4d | 247.67(1) | 0.63(4) | 6.5(6) | 0.22(3) |
| | 5d | 248.03(2) | 0.39(4) | | |
| | ε s,d | 248.63(1) | 1.38(8) | 40.3(10) | |
| | $2p_{1/2} \rightarrow 4s$ | 246.51(1) | 0.28(5) | 0.19(10) | 0.023(13) |
| | 3d | 249.07(1) | 0.50(3) | | |
| | 4d | 249.82(1) | 0.30(3) | 2.7(7) | 0.20(5) |
| | 5d | 250.17(2) | 0.14(3) | | |
| | ε s,d | 250.78(1) | 0.82(6) | 24.7(4) | |

Table I continued.

| Atom | Transition | Energy (eV) | Oscillator Strength $f$ | Threshold Intensity $I_{th}$ | $\frac{1}{f}\frac{df_s}{dKE}\Big\|_0 (eV^{-1})$ |
|---|---|---|---|---|---|
| Kr | $3d_{5/2} \rightarrow 5p$ | 91.20(1) | 1.0 | 1.00(4) | 0.14(2) |
| | 6p | 92.56(1) | 0.37(1) | 0.57(3) | 0.21(3) |
| | 7p | 93.06(1) | 0.12(1) | 0.29(1) | 0.33(6) |
| | 8p | 93.30(3) | 0.08(4) | 0.24(1) | 0.41(22) |
| | $\epsilon p$ | 93.79(2) | 0.36(8) | 2.57(12) | |
| | $3d_{3/2} \rightarrow 5p$ | 92.43(1) | 0.63(1) | 0.66(3) | 0.15(2) |
| | 6p | 93.81(1) | 0.23(1) | 0.41(3) | 0.25(4) |
| | 7p | 94.32(2) | 0.087(10) | 0.18(2) | 0.29(7) |
| | 8p | 94.57(3) | 0.034(14) | 0.14(2) | 0.57(30) |
| | $\epsilon p$ | 95.04(3) | 0.22(4) | 1.62(8) | |
| Xe | $4d_{5/2} \rightarrow 6p$ | 65.11(1) | 1.0 | 1.00(4) | 0.29(5) |
| | 7p | 66.38(1) | 0.334(6) | 0.55(3) | 0.47(9) |
| | 8p | 66.85(1) | 0.112(7) | 0.21(1) | 0.53(10) |
| | $\epsilon p$ | 67.55(1) | 0.37(6) | 1.60(8) | |
| | $4d_{3/2} \rightarrow 6p$ | 67.04(1) | 0.74(2) | 0.69(5) | 0.27(4) |
| | 7p | 68.35(1) | 0.226(7) | 0.34(2) | 0.43(6) |
| | 8p | 68.84(2) | 0.092(12) | 0.14(1) | 0.42(9) |
| | $\epsilon p$ | 69.54(1) | 0.29(2) | 0.87(4) | |

Table II Natural linewidth of the inner-shell resonance of lowest photon energy for Ar, Kr, and Xe, and the width ($1/\tau$) of the Niehaus function (Eqns (4) and (5)) which best fits the threshold peaks.

| Atom | Threshold Width Niehaus Function (eV) | Resonance Natural Linewidth (eV) this work | Ref. 3 | Ref. 4 |
|---|---|---|---|---|
| Ar | 0.12(1) | | 0.116(3) | |
| Kr | 0.08(1) | 0.088(6) | 0.083(4) | 0.108 |
| Xe | 0.07(1) | 0.102(5) | 0.111(4) | 0.105 |

Table III. The contribution of shake-off and second-step Auger transitions in the total decay of the first resonances in Ar, Kr, and Xe.[a]

| Resonance | Shake-off Fraction | 2nd Step Auger |  | Identification |
|---|---|---|---|---|
|  |  | Fraction | Energy (eV) |  |
| Ar $2p_{3/2} \rightarrow 4s$ | 16(8) % | 18 % | 7.0(7) |  |
|  |  |  | 15.1(4) |  |
| Kr $3d_{5/2} \rightarrow 5p$ | 37(8) % | 16 % | 3.3(3) |  |
|  |  |  | 6.1(3) | $4s^{-1}4p^{-1}(^1P)5p \rightarrow 4p^{-2}\ {}^1S$, |
|  |  |  |  | $4s^{-2}5p \rightarrow 4s^{-1}4p^{-1}(^1P)$ |
|  |  |  | 7.9(3) | $4s^{-1}4p^{-1}(^1P)5p \rightarrow 4p^{-2}\ {}^1D$ |
|  |  |  | 9.6(3) | $4s^{-1}4p^{-1}(^1P)5p \rightarrow 4p^{-2}\ {}^3P$, |
|  |  |  |  | $4s^{-2}5p \rightarrow 4s^{-1}4p^{-1}(^3P)$ |
|  |  |  | 13.8(3) | $4p^3 4d5p \rightarrow 4p^{-2}\ {}^1D$ |
| Xe $4d_{5/2} \rightarrow 6p$ | 51(10) % | 18 % | 6.1(3) | $5s^{-1}5p^{-1}6p \rightarrow 5p^{-2}\ {}^3P, {}^1D$, |
|  |  |  |  | $5s^{-2}6p \rightarrow 5s^{-1}5p^{-1}\ {}^3P$ |
|  |  |  | 10.0(3) | $5p^{-3}5d6p \rightarrow 5p^{-2}\ {}^1D$ |

[a] All fractions represent a percentage of the total $\sigma$ on the resonance excluding the nonresonant valence $\sigma_{ns}$ and $\sigma_{np}$.

Table IV The calculated shake probabilities $P_{nl}$ accompanying Auger-like decay,[a] for example Ar $2p^{-1}4s \rightarrow Ar^{+}\ 3p^{-2}\varepsilon s$.

| Atom | orbital | $P_{nl}$ | Atom | orbital | $P_{nl}$ | Atom | orbital | $P_{nl}$ |
|---|---|---|---|---|---|---|---|---|
| Ar | 4s | 0.13 | Kr | 5p | 0.22 | Xe | 6p | 0.21 |
| | 5s | 0.49 | | 6p | 0.65 | | 7p | 0.63 |
| | 3d | 0.78 | | 7p | 0.96 | | 8p | 0.95 |
| | 4d | 0.99 | | 8p | 0.98 | | 9p | 0.98 |
| | 5d | 0.89 | | | | | | |

[a] For each resonance the probability of ejection (or excitation) of the Rydberg electron is shown.

FIGURE CAPTIONS

Fig. 1 A threshold scan over the Ar $2p^{-1}ns$, nd resonances and 2p thresholds. The curve reproduces a fit.

Fig. 2 A threshold scan over the Kr $3d^{-1}np$ resonances and 3d thresholds. The curve reproduces a fit.

Fig. 3 A threshold scan over the Xe $4d^{-1}np$ resonances and 4d thresholds. The curve reproduces a fit.

Fig. 4 An energy level diagram for the first Kr resonance. The arrows show the excitation and three types of single step decay which result in the ejection of two or more electrons.

Fig. 5 An electron difference spectrum of Ar taken at 244.4 eV photon energy on the $2p_{3/2}^{-1}4s$ resonance. Nonresonant contributions have been removed by subtracting a spectrum taken at 242.2 eV photon energy. The labels give only the most important final states.

Fig. 6 Electron difference spectrum, like Fig. 5, for Kr at 91.2 eV on the $3d_{5/2}^{-1}5p$ resonance. Non-resonant spectrum at 90.2 eV has been subtracted.

Fig. 7 Electon difference spectrum, like Fig. 5, for Xe at 65.1 eV on the $4d_{5/2}^{-1}6p$ resonance. Non-resonant spectrum at 64.1 eV has been subtracted.

Fig. 8 The low kinetic energy distribution of electrons ejected on two Kr resonances: Kr $3d_{5/2}^{-1}5p$ and $3d_{5/2}^{-1}7p$.

Fig. 9 The outer radial wavefunctions $\psi_{nl}$ of Ar calculated for the configuration $2p^{-1}3d$ and $\psi_{3d}$ of $Ar^{+}$ $3p^{-2}3d$.

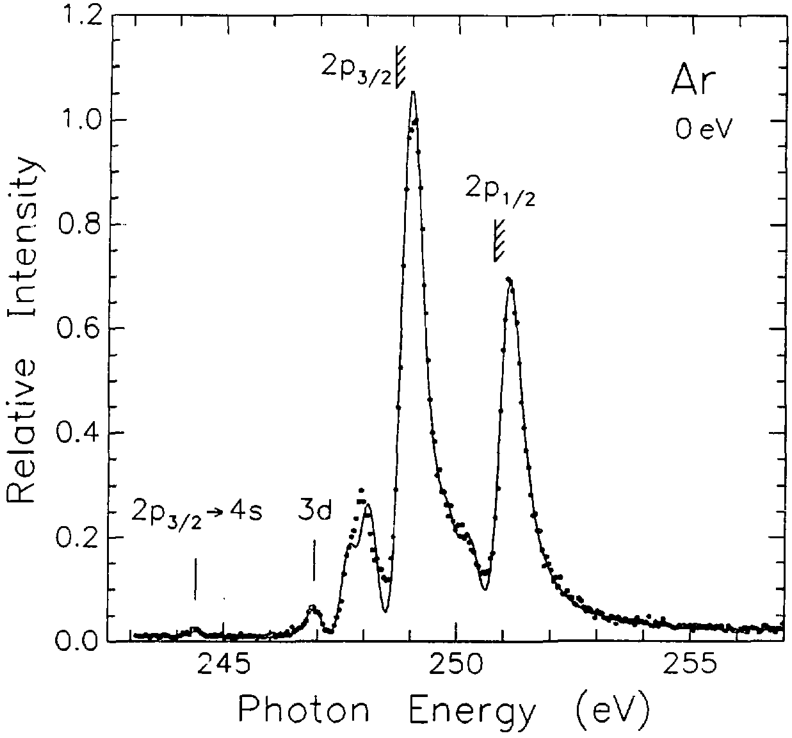

XBL 8611-4319

Figure 1

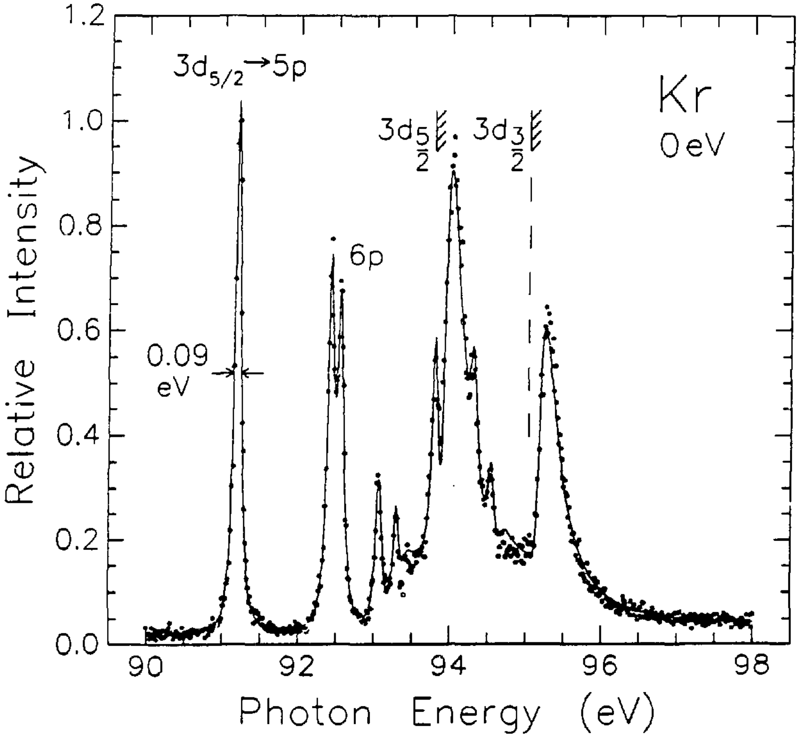

XBL 8611-4320

Figure 2

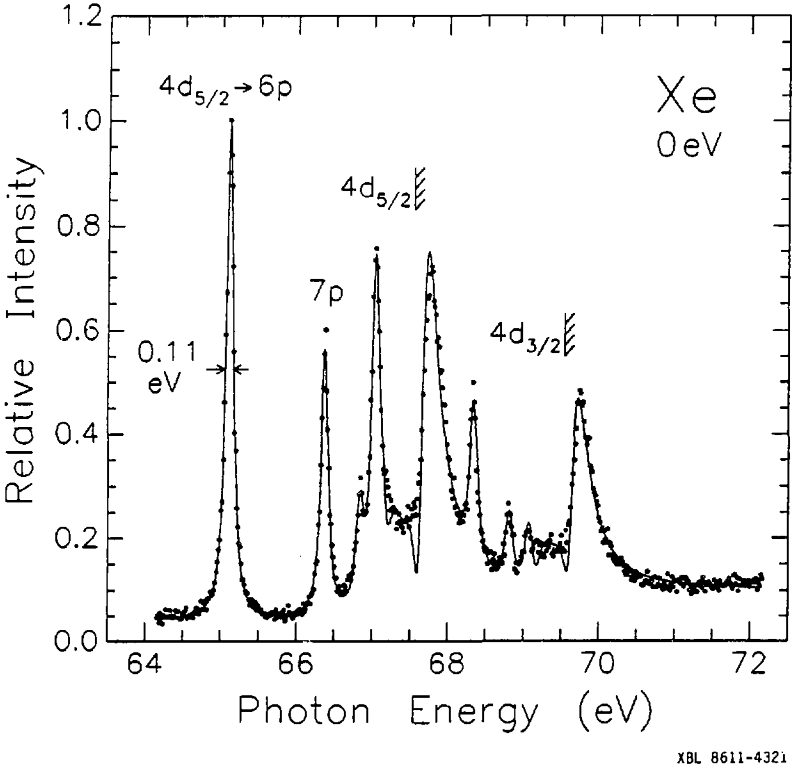
Relative Intensity
Photon Energy (eV)
0.0
0.2
0.4
0.6
0.8
1.0
1.2
64
66
68
70
72
$4d_{5/2} \rightarrow 6p$
Xe
0 eV
$4d_{5/2}$
7p
0.11 eV
$4d_{3/2}$
XBL 8611-4321

Figure 3

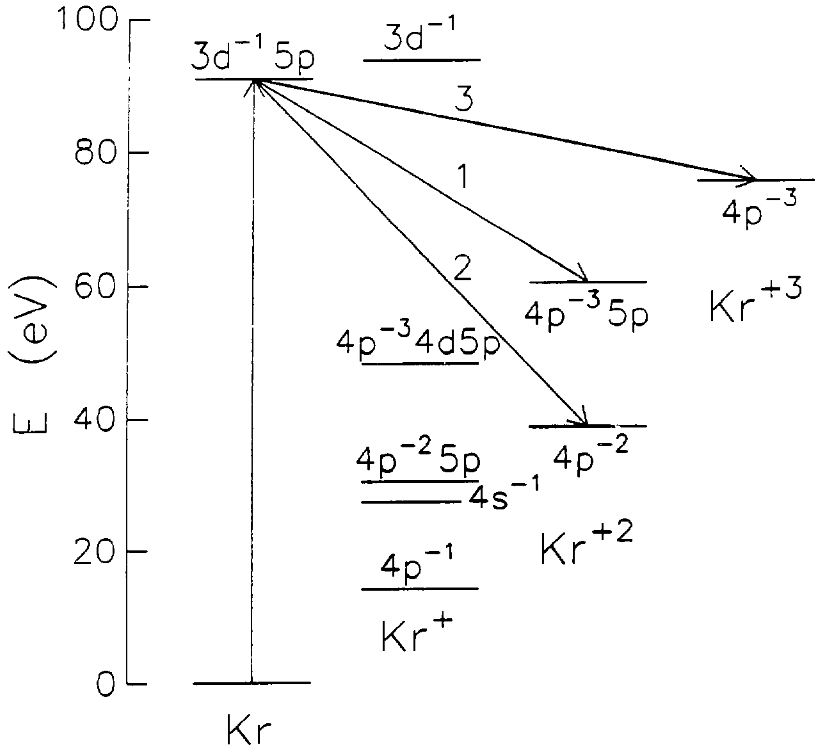

XBL 8611-4318

Figure 4

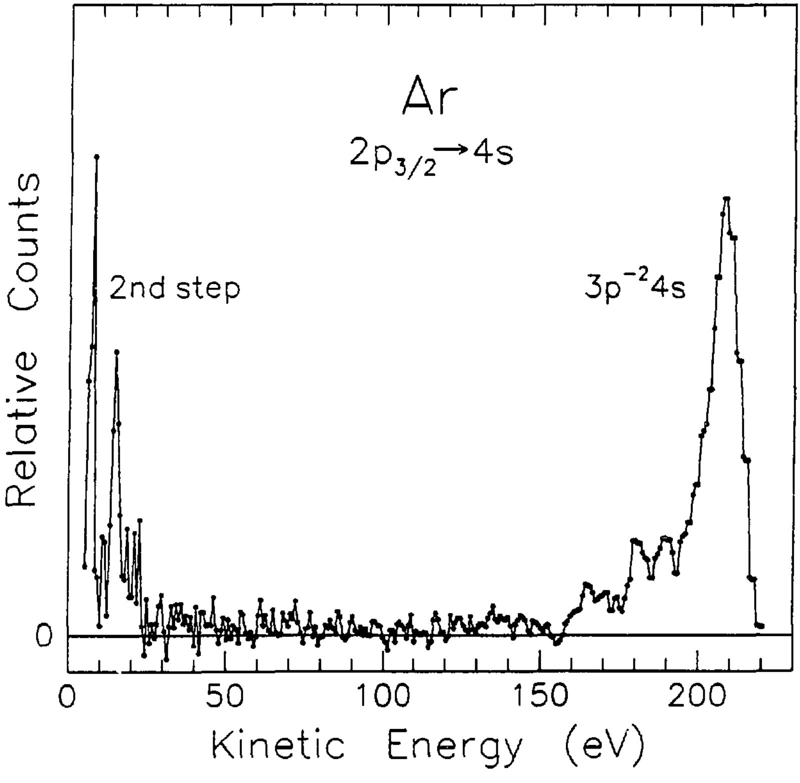

XBL 8611-4322

Figure 5

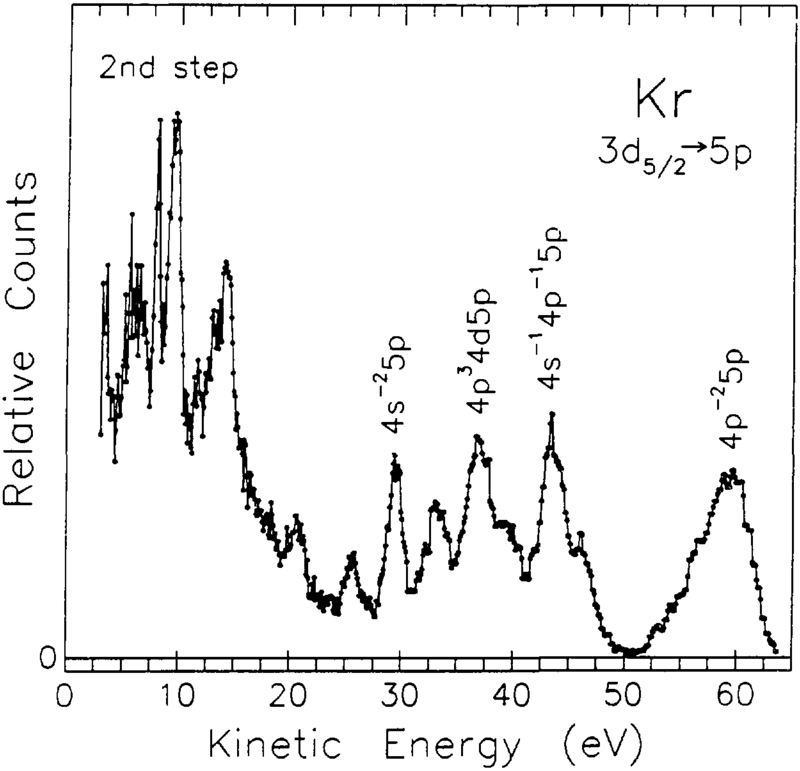

XBL 8611-4323

Figure 6

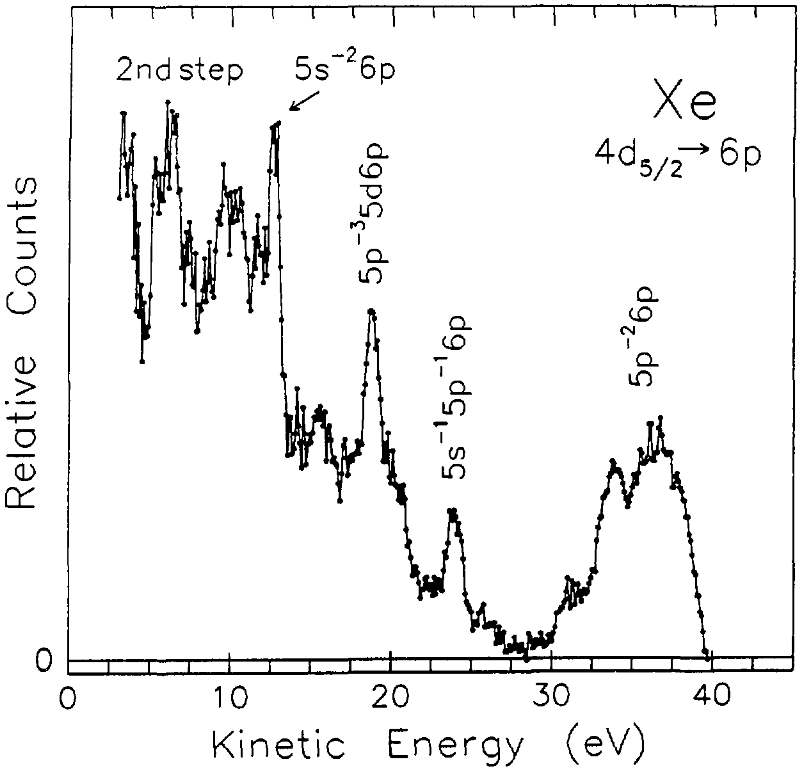

XBL 8611-4324

Figure 7

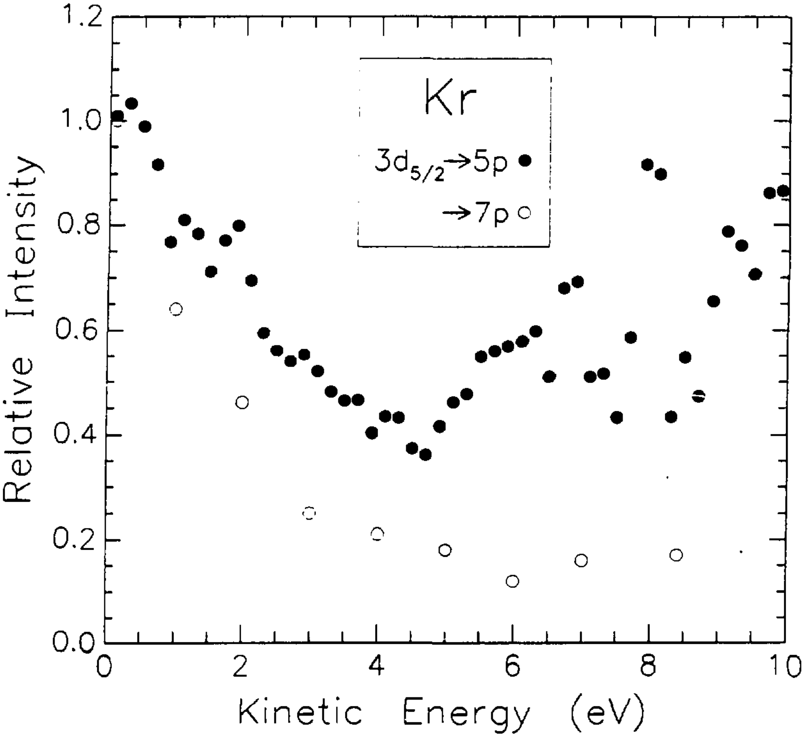

XBL 8611-4325

Figure 8

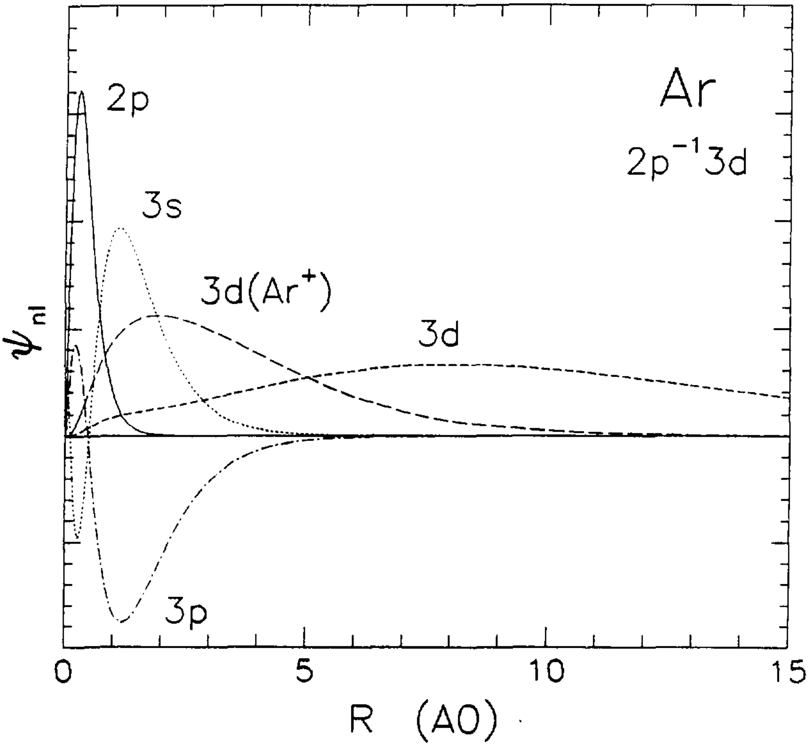

XBL 8611-4326

Figure 9

# VI. ARGON PHOTOELECTRON SATELLITES AT THRESHOLD*

## ABSTRACT

Photoionization of argon to excited satellite states, $Ar^+$ $1s^2 2s^2 2p^6 3s^2 3p^4 nl$, was studied with synchrotron radiation in the energy range $h\nu = 30 - 44$ eV and threshold electron analysis. At threshold, essentially all satellite final states, $^{2S+1}L$, are observed.

## A. INTRODUCTION

In photoelectron spectra there are both main-line peaks, e.g. $Ar^+$ $3s3p^6$, as well as satellite peaks, e.g. $Ar^+$ $3s^2 3p^4 nl$, which exist only because of electron correlation. The argon valence satellites have been much studied experimentally[1-4] and theoretically[5,6] because of the strong configuration interaction in the ion which mixes $3s3p^6$ $^2S$ and $3s^2 3p^4 nl$ $^2S$ states. In addition, satellite energies and intensities may be calculated for Ar without including relativistic effects. The theoretical predictions are appropriate for the sudden limit, at high photon energy hν, because they neglect both the energy variation of the dipole matrix element and interchannel coupling.[6] In high hν limit, the dominant contribution to the satellite spectrum is from $^2S$ states created by Final-Ionic-State Configuration Interaction (FISCI). The single largest satellite is $(^1D)3d$ $^2S$.

The argon satellite spectrum changes dramatically between hν = 1487 eV and hν = 40 eV. The lower hν range has been investigated by Adam et al.,[3] who measured both satellite cross sections and angular distributions. These authors divide the satellite spectrum in two parts based on the behavior through the 3s Cooper minimum. The first group of satellites, assigned to $3p^4 nd$ $^2S$ final states, show a constant intensity ratio to that of the 3s line, as well as a β value of 2. The other satellites, associated with the 3p main line, have intensity ratios to the 3p line that decrease slowly with increasing hν. The β values for these satellites differ from both $\beta_{3s}$ and $\beta_{3p}$. The most intense of these satellites has been assigned to the state $3s^2 3p^4 (^1D)3d$ $^2D$. FISCI can only open channels to $^2S$ and $^2P^o$ final states. Other terms may be accessible from initial state CI, which mixes $3s^2 3p^6\ ^1S$ with $3s^2 3p^4 nln'l'\ ^1S$ configurations, or from inelastic scattering of the photoelectron.[3]

A separate issue is the disagreement between the high hν photoelectron spectrum of these Ar satellites with the results of electron momentum spectroscopy (EMS). Smid and Hansen,[5] whose calculation supports the photoelectron intensities, have suggested that the binding energy spectra from EMS cannot be simply interpreted in terms of pole strengths. This question, however, is outside the scope of the present discussion.

In this chapter is presented a threshold electron scan of the Ar satellites based on the use of synchrotron radiation. Threshold electron analysis with its high resolution is ideally suited to the study of a complex spectrum such as the Ar valence satellites. Furthermore, the behavior of satellites at zero kinetic energy is of special interest. It is here that the sudden limit breaks down most completely and that mechanisms other than FISCI will be most important. The experimental methods are described in Sec. B. In Sec. C we report and discuss the satellite cross sections at threshold. Finally, Sec. D contains the conclusions.

## B. EXPERIMENTAL

This experiment was performed using a grazing incidence "Grasshopper" monochromator at the Stanford Synchrotron Radiation Laboratory (SSRL). The monochromator resolution with the 600 lines/mm grating is estimated to vary from 0.05 to 0.09 eV in going from 30 to 40 eV photon energy hν. In this low photon energy range, the photon intensity from the monochromator is quite low, and the fractional contribution of higher orders is high. The scans were carried out with and without an Al filter, which improved the first order purity especially above 36 eV, but also lowered the intensity. With the Al filter inserted, the fraction of first-order light increased from 39 % at 29 eV to 93 % at 44 eV. With the Al filter withdrawn, the contribution of first-order light went from 19 to 43 % over the same range. The higher orders were estimated from photoelectron spectra of Ne.

A similar threshold electron analyzer was described in some detail in a earlier paper,[7] while an account of the chamber and timing electronics can be found in White et. al.[8] Briefly, photoelectrons are extracted by a weak electric field from the interaction region, which results in a very high transmission for 0 and low kinetic energies. The electrons are energy analyzed by their flight times between the interaction region and the detector. The analyzer is fixed at 55° relative to the photon polarization vector. During a photon energy scan, a whole time spectrum is stored on disk for each energy. The intensity plotted in Fig. 1 represents the electron count rate inside a kinetic energy (time) window, $\Delta E = 0 - 0.05$ eV, divided by the photon flux, which has been corrected for higher-order contributions.

## C. RESULTS AND DISCUSSION

Figure 1 shows the threshold scan of the $Ar^+$ (3s) and $Ar^+$ $1s^2 2s^2 2p^4 nl$ satellites. Table I contains assignments of the observed peaks using energy level tables of Moore.[9] The identification of the $(^1D)3d\ ^2F$ final state, not found in Ref. 9, is based on the extrapolation of the series of doubly-excited states, $(^1D)3d(^2F_{7/2})nf$.[12] While two satellite peaks at 37.42 and 38.03 eV are assigned to a final state $(^1D)3d\ ^2P$ following Moore's tables, this identification should be correct for only one of these peaks.

The number of satellite lines in this Ar threshold scan is striking. Below 35.7 eV binding energy, all the LS terms listed in Moore's tables[9] are present in Table I. At higher binding energy, there are indications in the threshold scan of additional peaks not in Table I. At threshold it seems that all possible LS satellite states have significant cross sections. Similarly, the Ne satellite spectrum at threshold has a complex appearance with, however, fewer peaks.[7] The differences between the Ne and Ar spectra at threshold result in part from the greater density of low lying excited states in $Ar^+$. The larger size of the Ar 3p orbital relative to Ne 2p results in a reduction of the $^3P$-$^1D$-$^1S$ splittings. Among the Ar satellite final states at threshold, the excited electron most often goes into the 3d subshell, for which there is no Ne counterpart. The next most probable configurations at threshold are $Ar^+\ 3p^4 4s$ and $3p^4 4p$ with nearly equal likelihood. Finally, for both Ar and Ne, the distribution of satellite intensities among the core term symbols at threshold is close to statistical. For the case of Ar, $^3P:{}^1D:{}^1S = 9:6.7:0.7$.

The labels 1 to 5 in Fig. 1 are the notation used by Adam et al.[3] to identify the satellite peaks in their Ar photoelectron spectra at intermediate kinetic energies, 3 to 35 eV. The number of observed satellite lines is quite different for the threshold and higher kinetic energy spectra. One contributing factor is our higher resolution of 0.1 eV compared with 0.8 eV used by Adam et al.[3] From a lineshape analysis, Adam et al. infer additional, unresolved peaks on the low binding-energy side of satellites 1, 2 and 3. However, the improved resolution is not a sufficient explanation because Adam et al.'s spectrum at $h\nu = 43$ eV has a flat background from the 3s line until 33.5 eV binding energy. Therefore, the cross section $\sigma$ for these three satellite transitions must have decreased to essentially zero in going from threshold to $h\nu = 43$ eV. Because whole time spectra were stored during the scan, plots can be made like Fig. 1 but at higher kinetic energies and with much worse signal-to-noise. The $(^3P)4s\ ^2P$ satellite, for example, is clearly observable for kinetic energies ranging from 0 to 0.9 eV. Another recent photoelectron experiment has studied the satellite intensity variations from about 1 - 10 eV kinetic energy.[13]

At and near threshold, the mechanism for producing satellites is altered. Earlier,[7] an analogy has been discussed between double ionization and satellites at threshold. In both cases two electrons move slowly from the ion core; here it is the photoelectron and excited electron. At low photoelectron kinetic energies, the interaction between these two electrons is more important, which results in a changed intensity distribution over the possible satellite final states.

At threshold as at any kinetic energy, the satellite cross sections are influenced by the changing main-line cross sections, which reflect the variation of the dipole matrix elements, e.g. $\langle 3s|r|\varepsilon p\rangle$. The $3p^4(^1D)$ 3d and 4d $^2S$ satellites, caused by FISCI with the $3s3p^6$

configuration, contribute only a small fraction of the threshold satellite intensity. However, compared with its intensity in the range of the 3s Cooper minimum,[3] the threshold intensity of the $3p^4(^1D)3d\ ^2S$ satellite is an order of magnitude higher. In the case of this FISCI satellite, the satellite and its main line go through a Cooper minimum in a similar way. The satellites besides those assigned to $^2S$ final states should be associated with correlation processes occuring in the 3p subshell. This tentative conclusion is supported by the intensity variations observed at intermediate photon energy[3] and by the simple fact that $\sigma_{3p}$ is many times larger than $\sigma_{3s}$ in this photon energy range. The overall intensity of the non-$^2S$ satellites increases from intermediate kinetic energy[3] to threshold, as does the 3p main line. The variation of the dipole matrix element, as measured by σ(main line), is only one contributing factor to the satellite cross section at low kinetic energy. As an example, the branching ratio of the $(^1D)3d\ ^2S$ satellite to the 3s line, at both $\varepsilon = 0$ eV and $h\nu = 38.6$ eV, differs from the high photon-energy value.[1]

Autoionization from doubly-excited states can cause dramatic variation in satellite cross sections. Since these resonances are located below successive satellite thresholds, their autoionization is most important for low satellite kinetic energies and for satellites of lower binding energy. Autoionization into satellite channels has been previously studied by Woodruff and Samson[14] in He and by Becker et al.[15] in Ne. For five Ar satellites, the cross sections decrease strongly from threshold to $\varepsilon = 0.2$ or 0.3 eV. In each case a doubly-excited state may be found near the satellite threshold, which may resonantly enhance the satellite cross section. Table II contains a list of the satellites and the resonances which affect them at threshold.

The oscillator strength is a continuous function from a doubly-excited Rydberg series across a satellite threshold. Therefore, the threshold satellite scan should resemble the absorption spectrum of doubly-excited states. There is a correspondence between most of the satellite final states which are strong at threshold and the prominent Rydberg series where Madden et al.[12] were able to identify more than two members. In addition, the qualitative observations of Madden et al.[12] about the doubly-excited states could also apply to the satellites at threshold. $3p^4 3dnl$ ($3p^4 3d$) states are most important followed by $3p^4 4snl$ ($3p^4 4s$). $3p^4 4pnl$ ($3p^4 4p$) configurations and quartet states appear to be more prominent in the threshold satellite spectrum than in the doubly-excited resonances. However, these states may occur among the unassigned resonances.

## D. CONCLUSIONS

A discussion has been given above which should apply in its general outline to the valence satellites of any atom or molecule at threshold. All possible LS final states are reached. The threshold satellite spectrum differs from that at intermediate kinetic energies by the presence of additional peaks, some of which persist at least until $\varepsilon = 1$ eV. Very roughly, the broader final-state distribution is caused by the increased interaction of the slowly leaving photoelectron with the ion. Most of the satellites should be associated with correlation processes in the outer p subshell. The FISCI mechanism can only account for a fraction of the satellite peaks, with $^2S$ and $^2P^o$ term symbols. Autoionization from doubly-excited states is influential, strongly enhancing certain satellites. Finally, there exists a correspondence between the prominent series of doubly-excited states and the more intense satellites at threshold. A theoretical calculation of the Ar satellite spectrum at zero kinetic energy would be very valuable.

## REFERENCES

*Work done in collaboration with S.H. Liu, and D.A. Shirley.

1. D. Spears, E.J. Fishbeck, and T.A. Carlson, Phys. Rev. A 9, 1603 (1974).
2. M.Y. Adam, F. Wuilleumier, S. Krummacher, V. Schmidt, and W. Mehlhorn, J. Phys. B 11, L413 (1978).
3. M.Y. Adam, P. Morin, and G. Wendin, Phys. Rev. A 31, 1426 (1985).
4. C.E. Brion, K.H. Tan, and G.M. Bancroft, Phys. Rev. Lett. 56, 584 (1986).
5. H. Smid and J.E. Hansen, J. Phys. B 14, L811 (1981); H. Smid and J.E. Hansen, J. Phys. B 16, 3339 (1983).
6. K.G. Dyall and F.P. Larkins, J. Phys. B 15, 219 (1982).
7. P.A. Heimann, U. Becker, H.G. Kerkhoff, B. Langer, D.Szostak, R. Wehlitz, D.W. Lindle, T.A. Ferrett, and D.A. Shirley, Phys. Rev. A 34, 3782 (1986).
8. M.G. White, R.A. Rosenberg, G. Gabor, E.D. Poliakoff, G. Thornton, S.H. Southworth, and D.A. Shirley, Rev. Sci. Instrum. 50, 1268 (1979).
9. C.E. Moore, Atomic Energy Levels, Natl. Bur. Stand. (U.S.) Circ. No. 467 (U.S. GPO, Washington , D.C., 1949), Vol. 1.
10. G.V. Marr and J.B. West, At. Data Nucl. Data Tables 18, 497 (1976).
11. C.D. Lin, Phys. Rev. A 9, 171 (1974).
12. R.P. Madden, D.L. Ederer, and K. Codling, Phys. Rev. 177, 136 (1969).
13. U. Becker, private communication.

14. P.R. Woodruff and J.A.R. Samson, Phys. Rev. Lett. 45, 110 (1980); P.R. Woodruff and J.A.R. Samson, Phys. Rev. A 25, 848 (1982).

15. U. Becker, R. Hölzel, H.G. Kerkhoff, B. Langer, D. Szostak, and R. Wehlitz, Phys. Rev. Lett. 56, 1120 (1986).

Table I. Argon valence satellite binding energies, whose uncertainty is 0.02 eV, together with the optical energies of Moore.[9] All the assigned satellite final states include a $1s^2 2s^2 2p^6 3s^2 3p^4$ core. The last column contains the satellite cross sections at threshold.

| Peak Assignment | Binding Energy (eV) | Optical Energy (eV) | σ (Mb) |
|---|---|---|---|
| 3p | | 15.8 | 29.2(9)[a] |
| 3s | | 29.24 | 0.8[b] |
| $(^3P)3d\ ^4D$ | 32.17 | 32.18 | 0.033(4) |
| $(^3P)4s\ ^4P$ | 32.47 | 32.46 | 0.027(4) |
| $^2P$ | 32.88 | 32.94 | 0.076(7) |
| $(^3P)3d\ ^4F$ | 33.54 | 33.45 | 0.071(6) |
| $^2P$ | 33.78 | 33.78 | 0.300(12) |
| $^4P$ | 34.04 | 34.06 | 0.044(7) |
| $(^1D)4s\ ^2D$ | 34.20 | 34.20 | 0.196(11) |
| $(^3P)3d\ ^2F$ | 34.39 | 34.30 | 0.088(5) |
| $^2D$ | | 34.49 | |
| $(^1D)3d\ ^2G$ | 34.91 | 34.88 | 0.039(4) |
| $(^3P)4p\ ^4P^o$ | | 35.01 | 0.160(13) |
| $^4D^o$ | 35.28 | 35.30 | |
| $^2D^o$ | 35.51 | 35.44 | |
| $^2P^o$ | | 35.60 | |
| $(^1D)3d\ ^2F$ | 36.00 | 36.03 | 0.094(7) |
| $(^1S)4s\ ^2S$ | 36.51 | 36.50 | 0.040(6) |
| $(^1D)4p\ ^2F^o$ | 36.90 | 36.89 | 0.051(7) |
| $(^1D)4p\ ^2P^o$ | 37.11 | 37.11 | 0.061(4) |

| | | | |
|---|---|---|---|
| $(^1D)3d\ ^2D$ | 37.23 | 37.18 | 0.066(7) |
| $(^1D)4p\ ^2D^o$ | | 37.25 | |
| $(^1D)3d\ ^2P$ | 37.42 | 37.40 | 0.045(3) |
| $(^1D)3d\ ^2P$ | 38.03 | 38.04 | 0.044(2) |
| $(^3P)5s\ ^4P$ | 38.33 | 38.32 | 0.007(1) |
| $(^1D)3d\ ^2S$ | 38.59 | 38.58 | 0.029(2) |
| $(^1S)3d\ ^2D$ | 38.90 | 38.91 | 0.011(1) |
| $(^3P)5p\ ^2P^o$ | 39.35 | 39.33 | 0.038(2) |
| $^2D^o$ | | 39.38 | |
| $(^3P)4d\ ^2P$ | | 39.39 | |
| $(^1S)4p\ ^2P^o$ | 39.61 | 39.57 | 0.028(2) |
| $(^3P)4d\ ^2D$ | | 39.64 | |
| $(^1D)5s\ ^2D$ | 40.03 | 40.04 | 0.025(3) |
| $(^3P)4f$ | | 40.07 | |
| $(^1D)4d\ ^2S$ | 41.16 | 41.20 | 0.023(4) |
| Sat. total | | | 1.68 |

[a] Ref. 10

[b] Ref. 11

Table II. The doubly-excited states (Ref. 12) which autoionize into satellite channels at threshold.

| Resonance | hν (eV) | Satellite |
|---|---|---|
| $(^1D)3d(^2F_{5/2})4p$ | 32.853 | $(^3P)4s\ ^2P$ |
| $(^3P)4p(^2D_{3/2})5s$ | 33.582 | $(^3P)3d\ ^4F$ |
| $(^1D)3d(^2G_{7/2})6f$ | 34.494 | $(^3P)3d\ ^2F,\ ^2D$ |
| $(^1S)4s(^2S_{1/2})7p$ | 36.020 | $(^1D)3d\ ^2F$ |
| $(^1D)3d(^2P_{3/2})9p$ | 37.127 | $(^1D)4p\ ^2P^o$ |

## FIGURE CAPTION

Fig. 1 Threshold photoelectron scan of the Ar valence satellites. The count rate at the 3s peak is 53 c/s.

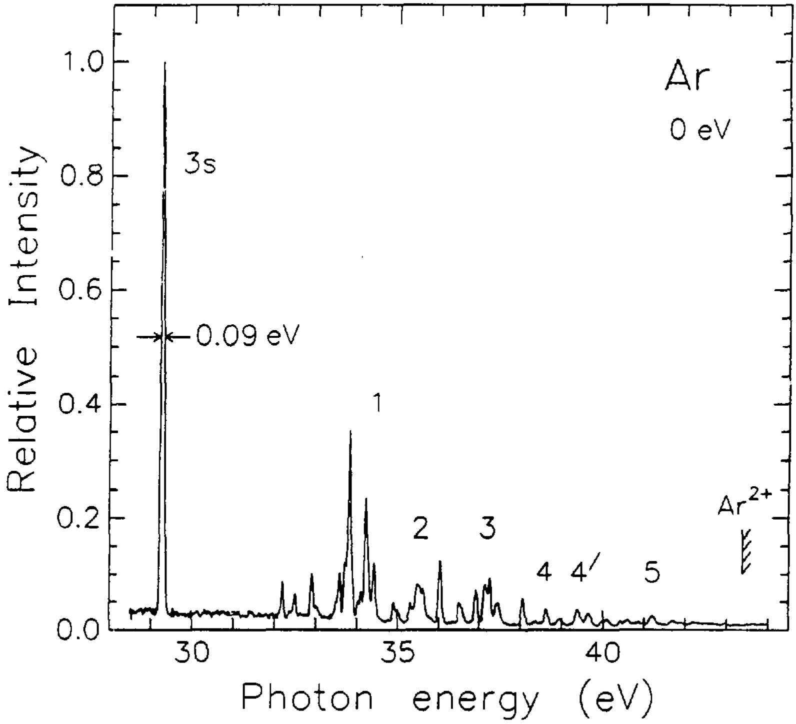

XBL 8611-4327

Figure 1

## ACKNOWLEDGEMENTS

I would like to thank my research advisor Professor Dave Shirley for his support and Professor Uwe Becker for his enthusiasm.

The experiments were performed as a group effort with a number of different people at different times: Dennis Lindle and Trish Ferrett with whom I worked during my whole stay at Berkeley; Paul Kobrin and Carleton Truesdale who helped me get started; Ralf Wehlitz, Burkhard Langer and Daniel Szostak with whom I worked during the HASYLAB run; and also Professor Maria Novella Piancastelli, Professor William Brewer, Shihong Liu and Jane Medhurst. In addition I would like to thank the rest of the Shirley group for sharing many lunchtimes.

I received valuable assistance from the LBL support staff, especially from Warren Harnden (who taught me to draw dark lines), Tony Moscarelli and Joe Katz.

I would also like to thank my friends Hans Kerkhoff for his technical help and for his translation of German menus and Miriam Baskin for being a good roommate. Lastly, I would like to thank my parents, who I can take for granted.